Thesis

Experimental Verification of Beam Wander, Beam Spread and Scintillation in an Optical Laser Link through a Turbulent Atmosphere

by

Jesper Johannes Maria Frijns

May 17, 2023

for the degree of

Ir. & Master of Science
in Aerospace Engineering
(Space Engineering)

at Delft University of Technology

Responsible Thesis Supervisor:	Ir. K.A. Broekens,	TNO
Responsible Thesis Supervisor:	Dr.ir. R. Saathof,	Delft University of Technology
Examiner:	Dr. R.M. Groves,	Delft University of Technology
Chair:	Dr. A. Menicucci,	Delft University of Technology

TU Delft Delft University of Technology

TNO

NOTES TO THE READER

This is a thesis report describing the research performed for the degree of Master of Science. As the student and daily supervisors have the aspiration to publish the results of this study, the contents are structured in paper format. The results which will be available to the public are gathered in the paper, while additional results and background information are gathered in the appendices. If additional information is available for a part in the paper, then the appendix, wherein this can be found, is referred to.

This research is part of the Scylight programme of the European Space Agency, which ”supports the research, development and evolution of optical communications – laser – technologies, and provides flight opportunities for their in-orbit verification” [1]. Furthermore, the research is part of the Terabit Optical Communication Adaptive Terminal (TOmCAT) project within TNO [2], which aimes to prove the concept of optical feeder links. These links require high data throughput. In the TOmCAT project, the goal is to achieve uplink communications. The research topic has been requested by TNO as an addition to their development of the Ground Terminal Breadboard (GTB) and Satellite Terminal Breadboard (STB). The STB has only limited partial information of the received spot sent by the GTB. By researching the (almost) completely received spot, the individual components contributing to the final received power and scintillation can be related to the results of the STB by TNO. Furthermore, the empirical results can be compared to the used simulation software, which predicts the influence of atmospheric turbulence on optical propagation.

The research performed is concerned with empirical verification. For completeness the test setup and instruments are described. However, the design and setup of these instruments is not deemed part of the research performed. The research questions and objective can be found in subsection A-D.

PREFACE

Dear reader,

I am writing this report as part of my research thesis for Delft University of Technology. The purpose of the report is to show the capabilities of the student to perform research at a Master degree level and to be defended in front of an exam committee. This done by empirically validating the theoretical models used in laser satellite communications system design. The European Space Agency and Government of the Netherlands look for new and better ways to communicate with satellites; faster, safer and with less interference than current radio frequency communications. The research performed helps improving the models used to predict the influence of atmospheric turbulence on a laser link.

I would like to thank Rudolf Saathof for the guidance and support throughout this project. His practical approach to research and documentation made it a real pleasure to conduct my thesis research. Furthermore, I would like to thank Kristiaan Broekens for the internal guidance and help at TNO. Thank you very much for facilitating the required information and tools at TNO, along with the useful feedback. Another thanks goes out to Wimar Klop, who joined the update meetings and feedback group at a later stage. I would also like to thank the other employees and co-interns at TNO for their help, feedback and interesting conversations on laser satellite communications and optomechatronics.

Next to this, I would also like to thank the people close to my heart. Thank you very much, Lisanne, for the support and interest in my reseach. Thanks to my parents who housed me while writing this report, such that I could fully focus on it and thank you for listening to me babble about it. Thanks to my brother, Ruben, for the practical tips of conducting a thesis research and help in proofreading the report. Last but not least, I would like to thank my friends, with whom I have spent countless days studying in the Fellowship and quite some time drinking ”bakkie op ’t bankie”. It has been a blast studying and hanging out together in Delft. These are friendships, which will last a lifetime.

Lastly, I would like to ask that you use this report carefully and responsibly. It is intended for academic purposes only.

Sincerely,

Jesper Frijns

CONTENTS

NOMENCLATURE

List of Abbreviations

2D	**Two-D**imensional
AO	**A**daptive **O**ptics
BPF	**B**and**P**ass **F**ilter
BP	**B**eam **P**rofiler
C	**C**amera
ESA	**E**uropean **S**pace **A**gency
FM2	Secondary **M**irror
FS	**F**ocal **S**top
GEO	**G**eosynchronous **E**quatorial **O**rbit
GTB	**G**round **T**erminal **B**readboard
L1	**L**ens
LUT	**L**ook**U**p **T**able
M1	Primary **M**irror
M2	Secondary **M**irror
NDF	**N**eutral **D**ensity **F**ilter
OGS	**O**ptical **G**round **S**tation
PAT	**P**ointing, **A**cquisition and **T**racking
TL	**T**e**L**escope
TM	**T**urbulence **M**onitor

List of Symbols

$<>$	Variance
α_r	Angular distance from the boresight $[rad]$
$\bar{x}$	Horizontal spot center location $[m]$
$\bar{y}$	Vertical spot center location $[m]$
η_Q	Quantum efficiency $[-]$
κ_0	Outer scale parameter $[m^{-1}]$
Λ	Fresnel ratio at receiver $[-]$
λ	Wavelength $[m]$
Λ_0	Fresnel ratio at receiver $[-]$
Λ_{ST}	Instantaneous Fresnel ratio $[-]$
σ	Standard deviation
σ_I^2	Scintillation index $[-]$
σ_R^2	Rytov variance $[-]$
$\sigma_{I,l}^2$	Longitudinal scintillation index $[-]$
$\sigma_{I,on-axis}^2$	On-axis scintillation index $[-]$
$\sigma_{I,r}^2$	Radial scintillation index $[-]$
$\sigma_{pe,TC}$	Tip/tilt pre-corrected pointing error variance $[-]$
Θ	Beam curvature parameter at receiver $[-]$
θ	Angle along ellipse $[rad]$
Θ_0	Beam curvature parameter at transmitter $[-]$
ζ	Zenith angle $[rad]$
A	Nominal value of C_n^2 at ground level $[m^{-2/3}]$
b_c	Hot spot movement $[m]$
c	speed of light $[m/s]$
C_n^2	Refractive index structure parameter $[m^{-2/3}]$
C_r	Scaling factor $[-]$
d	Distance $[m]$
d	Width of central band in diffraction pattern $[m]$
$D4\sigma$	Second-moment width $[m]$
E	Photon energy $[J]$
f	Lens focal distance $[m]$
F_0	Radius of the phase front at transmitter $[m]$
FW	Detector Full Well Capacity $[-]$
G_D	Detector gain $[-]$
G_I	Imager gain $[m^2 \cdot pixelcount]$
H	Receiver altitude $[m]$
h	Altitude above sea level $[m]$
h	Planck constant $[m^2 kg/s]$
h_0	Transmitter altitude $[m]$
h_{OGS}	OGS height above sea level $[m]$
I	Intensity $[W/m^2]$
k	Scalar spatial wave number $[rad/m]$
L	Link path length $[m]$
n	Measurement number $[-]$
n	Number of bits $[-]$
R	Mirror radius of curvature $[m]$
r	Radial distance $[m]$
r_0	Atmospheric coherence width (Fried parameter) $[m]$
r_c	Beam wander $[m]$
r_w	Instantaneous spot radius $[m]$
T	Optical transmission $[-]$
t_S	Shutter time $[s]$
T_z	two-axis Zernike tilt variance $[-]$
U	Step function $[-]$
v	Pseudowind $[m/s]$
W	Actual width of imaged object $[m]$
W	Free-space spot radius $[m]$
w	$1/e^2$ radius $[m]$
W_0	Beam radius at transmitter $[m]$
W_{LT}	Long-term spot radius $[m]$
W_{ST}	Short-term spot radius $[m]$
z	Focal distance $[m]$

Experimental Verification of Beam Wander, Beam Spread and Scintillation in an Optical Laser Link through a Turbulent Atmosphere

J.J.M. Frijns, K.A. Broekens, W.A. Klop, R. Saathof

Abstract

Laser satellite communications for ground-to-ground and ground-to-space links is influenced by atmospheric turbulence. Typically, theoretical models are used to predict link performance and the influence of the atmosphere on variables such as beam wander, spot size and scintillation at the receiver. These variables are used as input for system design. However, the models, which predict the individual variables have not yet been empirically verified for their individual contributions. Therefore, this paper focuses on retrieving the individual variables estimated by theoretical models from measurements representing these variables. These measurements have been retrieved in a 10 km uplink path, ground-to-ground field test. In this test, the receiver plane is imaged. The spot location and size and the longitudinal, radial and on-axis scintillation indices are estimated from the measurements. Also, turbulence strength is measured along the path and are used as inputs for the theoretical models. For weak turbulence conditions the theory and test results fall within the same order of magnitude. For all effects, except on-axis scintillation, the values predicted by theory lie at a slightly higher value than retrieved with the field test for the weak turbulence regime. For strong turbulence conditions the difference in results between theory and data grows, up to order one. To the authors' knowledge, this is the first time the turbulence variables have been experimentally investigated in so much detail. It is clear from the differences, that both the experimental setup and theory for horizontal ground-to-ground links need attention to close the gap between them, especially for turbulence conditions outside the Rytov approximation range.

Keywords

Laser satellite communication, pre-correction, optical propagation, ground-to-ground, uplink, atmospheric turbulence, experimental verification, beam wander, beam spread, spot size, scintillation.

I. Introduction

SATELLITE COMMUNICATIONS using radio frequency is reaching its limitations in terms of data rate and frequency congestion [3]. A feasible option to provide higher data rates is by the use of laser communications [4]. Several parties have set up programs to develop such new satellite communications systems, for example the European Space Agency [5] and National Aeronautics and Space Administration [6].

The main challenges for space-to-ground, or ground-to-space laser communications are cloud coverage, atmospheric turbulence and atmospheric absorption. Fortunately, optical communications systems can be designed to mitigate these challenges, such as by implementing Adaptive Optics (AO). Furthermore, Poulenard 2014 [7] estimates availability using geographic diversity to mitigate cloud cover.

Atmospheric turbulence causes beam wander, beam spread and scintillation, which disturb the optical communications link [8], [9]. Furthermore, vibrations in the communications systems can induce additional beam jitter [10]–[12]. These effects of atmospheric turbulence on laser links have been analytically described [9], [13]–[17]. These studies are used to develop relations, which aid in the development of physical laser communications systems for either ground-to-ground or space-to-ground/ground-to-space systems [18]–[20]. For ground-to-ground systems also building sway and thermal cycling of buildings have been verified [21]. To mitigate the effect of turbulence in communications links Pointing, Acquisition and Tracking (PAT) and Adaptive Optics systems have been developed [8], [22], [23].

To verify the theory as summarized in analytic equations [9], numerical propagation techniques [14], [16], [24]–[28] have been used and experiments [29]–[40] have been performed. However, there used to be a mismatch between numerical and analytical results, as the effect of beam wander on scintillation was underestimated [41], [42]. The question arises if the assumptions on which updated models [14]–[16] are based represent reality accurately.

To the authors' knowledge, in the existing body of literature the individual effect of turbulence towards beam wander and beam spread have not been experimentally investigated. Concluding, there is a need for empirical research on relations, which describe the influence of atmospheric turbulence on optical propagation to understand their accuracy and to aid in the development of future optical communications systems. The contributions will be analyzed separately in order to incorporate their individual effects in link budget calculations.

To experimentally verify the separate effects of turbulence, first, the theoretical models under consideration are presented in section II. Secondly, in section III the experimental setup and data analysis are described. Next, the results are shown in section IV, which are then discussed in section V. The paper is concluded in section VI.

II. Analytic Equations about Atmospheric Influence on Optical Propagation

A propagating beam through turbulence is distorted due to refractive index fluctuations, which cause phase changes in the electromagnetic field. Moreover, irradiance fluctuations occur. Differences in refraction indices throughout the atmosphere due to turbulence cause light passing through it to not follow a straight path. Over long distances these effects can enlarge, leading to spatial incoherence of the wavefront, i.e. a perfect spot is distorted.

Several models have been collected, which will be used to compare to the empirical results to. The first is from Andrews 2005 [9], as it forms the basis of the models used in the industry. The second, third and fourth model are on horizontal links [14]–[16], as a nearly-horizontal path is under consideration in this paper. The differences are small between the previously mentioned models, but they are all included for completeness. The last model is from [17], which uses and adds small variations to [9]. As the fitted results in [17] to a ground-to-GEO link match very closely, it is worth investigating how the theory matches for a ground-to-ground link. Note that if models make use of the same equation, that equation is only presented once.

First, the turbulence model under consideration is discussed in subsection II-A. The effects described in this study are beam wander (subsection II-B), beam spread (subsection II-C) and scintillation (subsection II-D).

A. Turbulence Model

To describe optical propagation through a turbulent atmosphere, the atmospheric turbulence can be modelled with the refractive index structure parameter (C_n^2). As this paper focuses on the comparison of theory and empirical results with a ground-to-ground link test, the refractive index structure parameter profiles retrieved from the test are used, see subsection III-B.

Next to this, the turbulence strengths are split up in a weak turbulence and a moderate/strong turbulence regime, as most models are only valid for weak turbulence conditions.

The border between these regimes is determined by the Rytov variance for a divergent Gaussian beam, see Equation 1 [9]:

$$\sigma_B^2 \cong 3.86\sigma_R^2 \left\{ 0.40 \left[(1+2\Theta)^2 + 4\Lambda^2 \right]^{5/12} \times \cos\left[\frac{5}{6} \tan^{-1}\left(\frac{1+2\Theta}{2\Lambda} \right) \right] - \frac{11}{16}\Lambda^{5/6} \right\}, \tag{1}$$

where σ_b^2 $[-]$ is the Rytov variance for a divergent Gaussian beam, Θ $[-]$ the beam curvature parameter of the beam at the receiver and σ_R^2 $[-]$ the Rytov variance for a plane wave, which is computed as [13]:

$$\sigma_R^2 = 1.23 C_n^2 k^{7/6} L^{11/6}, \tag{2}$$

where σ_R^2 $[-]$ is the Rytov variance, $k = 2\pi/L$ $[rad/m]$ the scalar spatial wave number and L $[m]$ the link length. Next to this C_n^2 $[m^{-2/3}]$ is the refractive index structure parameter, which gives an indication of the turbulence strength. Furthermore, Λ $[-]$ is the Fresnel ratio at the receiver [13]:

$$\Lambda = \frac{2L}{kW^2}. \tag{3}$$

If the Rytov parameter is smaller than unity, the turbulence conditions are of the weak kind.

B. Beam Wander

Beam wander is large movement of the beam caused by turbulence cells which are larger than the beam diameter, see Figure 1. These large cells refract the complete spot. Furthermore, turbulence cells close to the transmitter impact the beam wander more than cells closer to the receiver, as an equal angular refraction at a further distance from the receiver plane leads to more beam wander.

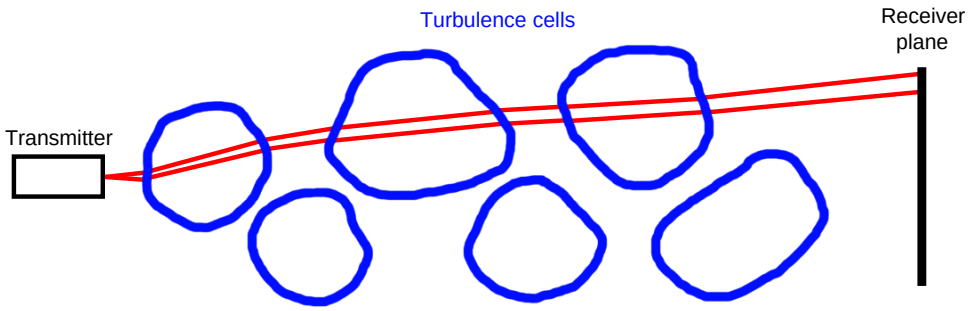

Fig. 1: Schematic representation of beam wander.

To combat this beam wander optical communications systems make use of tip/tilt correction [8], [22], [23]. If this tip/tilt correction is utilized, the beam is said to be ”tracked”. In the theory, it is assumed the tracking is perfect, such that the spot

does not move at the receiver. However, perfect tracking is difficult to achieve [14]. Therefore, as a comparison, the beam wander equations for an untracked beam are used.

Beam wander can be expressed by two variables: "hot spot movement", b_c, which is the movement of the brightest center of the beam within the total spot and "centroid movement", r_c, which is the combined result of generic wander of the whole spot and the hot spot within. The hot spot movement is related to centroid movement by Equation 4 [16]:

$$\left\langle b_c^2 \right\rangle = 0.56 \left\langle r_c^2 \right\rangle. \tag{4}$$

As the methods described in section III compute the total spot movement including hot spot movement, the term "beam wander" is used for centroid movement variance with the symbol $< r_c^2 >$.

The references mentioned above contain three different beam wander models for an untracked Gaussian beam. These models are only valid for weak turbulence conditions. The first is a model for a Gaussian beam in a slant path [9] see Equation 5:

$$\left\langle r_c^2 \right\rangle = 7.25 \left(H - h_0\right)^2 \sec^3(\zeta) W_0^{-1/3} \times \int_{h_0}^{H} C_n^2(h) \xi^2 \times \left[\frac{1}{\left|\Theta_0 + \bar{\Theta}_0 \xi\right|^{1/3}} - \frac{\kappa_0^2(h) W_0^2}{1 + \kappa_0^2(h) W_0^2 \left[\Theta_0 + \bar{\Theta}_0 \xi\right]^2} \right]^{1/6} dh, \tag{5}$$

where $\left\langle r_c^2 \right\rangle$ $[m^2]$ is the beam wander variance, H $[m]$ the receiver altitude, h_0 $[m]$ the transmitter altitude, ζ $[rad]$ the zenith angle, W_0 $[m]$ the beam radius at the transmitter, Θ_0 $[m]$ the beam curvature parameter at the transmitter, κ_0 $[m^{-1}]$ the outer scale parameter, which is set at 0 to give a worst-case value, $\xi = 1 - (h - h_0)/(H - h_0)$ and $\bar{\Theta}_0 = 1 - \Theta_0$.

The second model is from [14] and models a horizontal beam, see Equation 6:

$$\left\langle r_c^2 \right\rangle = \begin{cases} 2.42 C_n^2 L^3 W_0^{-1/3} {}_2F_1\left(\frac{1}{3}, 1; 4; \frac{L}{F_0}\right), \frac{L}{F_0} \leq 1 \\ 0.54 C_n^2 L^3 W_0^{-1/3} \left(\frac{F_0}{L}\right)^3 \left[9 + \frac{4L}{F_0}\left(\frac{5L}{F_0} - 6\right) + 9\left(\frac{L}{F_0} - 1\right)^{8/3}\right], \frac{L}{F_0} > 1, \end{cases} \tag{6}$$

where ${}_pF_q(a; b; z)$ a hypergeometric function and F_0 $[m]$ the radius of the phase front at the transmitter.

The third model is presented in Equation 7 [17] and is the only one to model a collimated beam:

$$\left\langle r_c^2 \right\rangle = 0.54 \left(H - h_0\right)^2 \sec(\zeta)^2 \left(\frac{\lambda}{2W_0}\right)^2 \left(\frac{2W_0}{r_0}\right)^{5/3} \tag{7}$$

where in this case the r_0 $[m]$, which is the atmospheric coherence width (Fried parameter) is computed as [17]:

$$r_0 = \left[0.42 \sec(\zeta) k^2 \int_{h_0}^{H} C_n^2(h) \xi^2 dh \right]^{-3/5}. \tag{8}$$

C. Spot Size

Two variables are important regarding the spot size: the long-term and short-term spot size. The models for the long-term spot size are collected in subsubsection II-C1 and for the short-term spot size in subsubsection II-C2.

1) Long-Term Spot Size: Under long exposure times, the imaged spot is widened and flattened due to beam wander. The long-term spot radius is therefore a combination of the average instantaneous spot radius and beam wander.

There are four different equations used in the comparison. The first model for a Gaussian beam is taken from [9], see Equation 9, which is valid for all turbulence conditions:

$$W_{LT} = \begin{cases} W\sqrt{1 + \left(D_0/r_0\right)^{5/3}}, & 0 \leq D_0/r_0 < 1 \\ W\left[1 + \left(D_0/r_0\right)^{5/3}\right]^{3/5}, & 0 \leq D_0/r_0 < \infty \end{cases}, \tag{9}$$

where W_{LT} $[m]$ is the long-term $1/e^2$ spot radius, W $[m]$ the free-space $1/e^2$ spot radius and

$$D_0^2 = 8 W_0^2. \tag{10}$$

W is computed via Equation 11 [9]:

$$W = W_0 \sqrt{\Theta_0^2 + \Lambda_0^2}, \tag{11}$$

where Λ_0 $[-]$ is the Fresnel ratio at the receiver:

$$\Lambda_0 = \frac{2L}{k W_0^2}. \tag{12}$$

Next to this Equation 9 makes use of the Fried parameter, which in this case is computed with Equation 13.

$$r_0 = \left[0.42 \sec(\zeta) k^2 \int_{h_0}^{H} C_n^2(h) dh \right]^{-3/5}. \tag{13}$$

The second model is from [14] and models a horizontal beam, see Equation 14:

$$W_{\mathrm{LT}} = W\left[1 + 1.33\sigma_R^2\left(\frac{2L}{kW^2}\right)^{5/6}\right]^{1/2}, \tag{14}$$

where W is computed as:

$$W = W_0\left[\left(1 - \frac{L}{F_0}\right)^2 + \left(\frac{2L}{kW_0^2}\right)^2\right]^{1/2}. \tag{15}$$

The third model is from [15], which also models a horizontal beam, see Equation 16:

$$W_{LT} \approx W\left(1 + 1.33\sigma_R^2\Lambda^{5/6}\right)^{3/5}, \quad 0 \leq \sigma_R^2 < \infty \tag{16}$$

where W is computed via Equation 15.

The last model comes from [17] and again is the only one to model a collimated beam, see Equation 17:

$$W_{LT}(L) = W\left[1 + \left(2\sqrt{2}\cdot\frac{W_0}{r_0}\right)^{5/3}\right]^{3/5}, \tag{17}$$

where

$$W(L) = \sqrt{W_0^2\left[1 + \left(\frac{\lambda L}{\pi W_0^2}\right)^2\right]}. \tag{18}$$

2) Short-Term Spot Size: On the short term, the beam "breathes" [9]: there is a short-term cyclical beam spread, which changes around a mean spot size, see Figure 2.

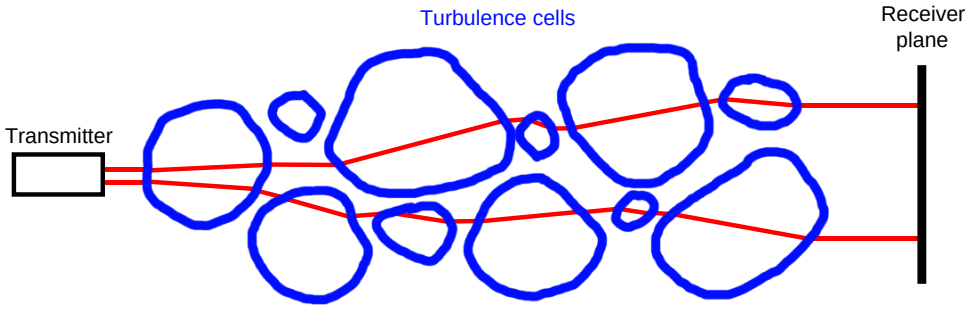

Fig. 2: Schematic representation of beam spread.

In the models presented, the long-term and short-term spot size are related via the mean beam centroid movement, see Figure 3. Thus, for all models the short-term spot size is computed via Equation 19:

$$W_{ST} = \sqrt{W_{LT}^2 - \langle r_c^2\rangle}, \tag{19}$$

where W_{ST} $[m]$ is the short-term $1/e^2$ beam radius.

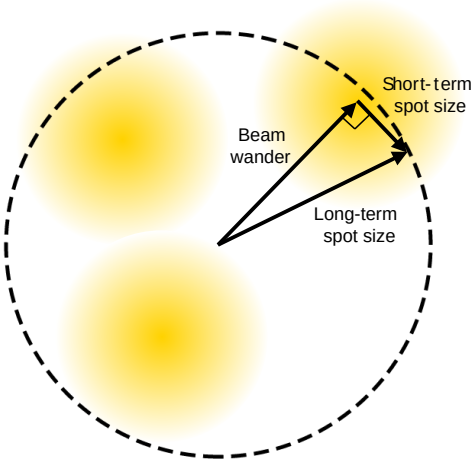

Fig. 3: Schematic representation of long-term spot size.

D. Scintillation

Scintillation is caused by the spatial incoherence of the wavefront, leading to constructive and destructive interference of light at an observer, see Figure 4. This effect is caused by small turbulence cells. Next to this, wandering of the beam leads to additional irradiance fluctuations in the receiver plane [41], [42]. Mathematically, the scintillation index is defined as the normalized variance of the intensity [13], see Equation 20:

$$\sigma_I^2 = \frac{\langle I^2 \rangle}{\langle I \rangle^2} - 1, \tag{20}$$

where σ_I^2 $[-]$ is the scintillation index and I $[W/m^2]$ the received intensity.

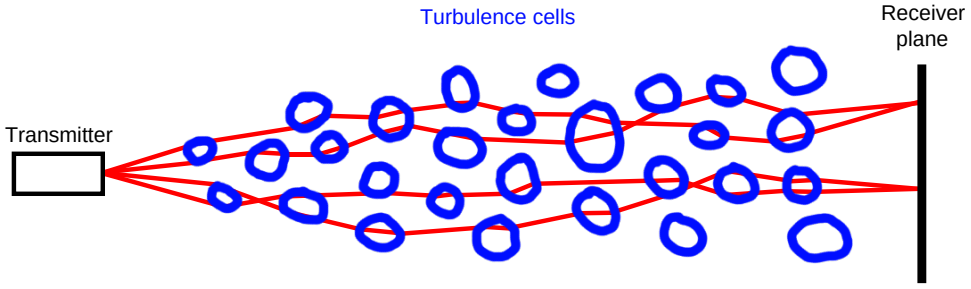

Fig. 4: Schematic representation of scintillation.

In this paper, three different scintillation variables are analyzed: longitudinal, radial and on-axis scintillation. These three variables are chosen, as they contain intensity information of the instantaneous spot (longitudinal and radial) and of the scintillation in the boresight (on-axis).

As, over time the full spot radius is captured in the field test, it is possible to analyze the scintillation across the spot. Furthermore, the scintillation in the boresight is an important performance factor for a communications link using a small receiver aperture. By using these three scintillation indices, the impact of scintillation across the instantaneous spot on the scintillation in the on-axis point can be found. The exact definitions for the three locations used in this paper are as follows, see Figure 5:

- **Longitudinal point:** the instantaneous spot center. The longitudinal point moves along with the spot as it wanders around in the 2D image.
- **Radial direction:** a vector with its origin at the longitudinal point (spot center), which points outwards from the spot center in the 2D plane.
- **On-axis point:** the point where the boresight of the ground station crosses the 2D image plane. This is the straight line a laser would follow under the absence of turbulence. Thus, the on-axis point is fixed in the receiver aperture. Thus, the link performance at the longitudinal point is influenced by beam wander and the quality of the received spot.

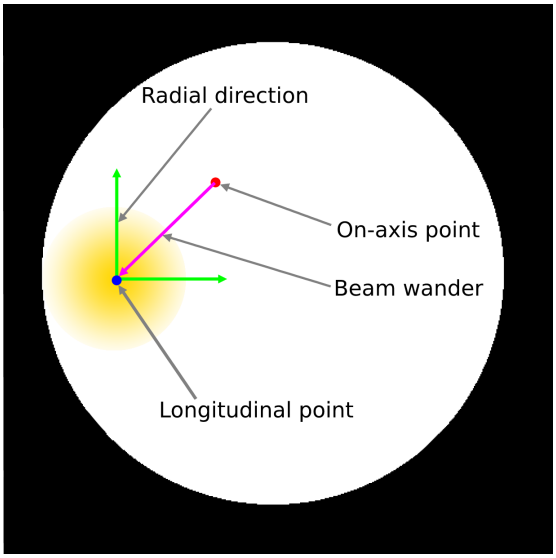

Fig. 5: Schematic representation of longitudinal (blue) and on-axis (red) point, and radial direction (green arrows). Note that the spot with longitudinal point and radial vectors wander in the imaged plane (magenta arrow).

Concluding, the longitudinal and on-axis scintillation index cover the scintillation of a single point, which moves along with the spot (longitudinal) or is fixed in a certain location (on-axis). The radial scintillation index is a vector with its origin at the longitudinal point and is computed as follows:

$$\sigma_I(\mathbf{r})^2 = \frac{\langle I(\mathbf{r},t)^2\rangle}{\langle I(\mathbf{r},t)\rangle^2} - 1, \tag{21}$$

Note that, if the spot is tracked perfectly and thus eliminating all beam wander, the longitudinal and on-axis point overlap. As mentioned before, this is practically unfeasible, which means the two points do not overlap. Moreover, this study focuses on the individual effects contributing to the overall effect of turbulence on optical propagation. Thus, these terms are analyzed separately.

1) Longitudinal Scintillation: The longitudinal scintillation is approximated by three unique equations. The first model for a Gaussian beam comes from [9], see Equation 22:

$$\sigma_{I,l}^2(L)_{\text{tracked}} = \exp\left[\frac{0.49\sigma_{Bu}^2}{\left(1+(1+\Theta)0.56\sigma_{Bu}^{12/5}\right)^{7/6}} + \frac{0.51\sigma_{Bu}^2}{\left(1+0.69\sigma_{Bu}^{12/5}\right)^{5/6}}\right] - 1, 0 \leq \sigma_{Bu}^2 < \infty, \tag{22}$$

where

$$\sigma_{Bu}^2 = 8.70\mu_{3,u}k^{7/6}\left(H-h_0\right)^{5/6}\sec^{11/6}(\zeta). \tag{23}$$

in Equation 23 σ_{Bu}^2 $[-]$ is the Rytov variance for a Gaussian uplink beam wave and

$$\mu_{3u} = \text{Re}\int_{h_0}^{H} C_n^2(h)\left\{\xi^{5/6}[\Lambda\xi + i(1-\bar{\Theta}\xi)]^{5/6} - \Lambda^{5/6}\xi^{5/3}\right\}dh. \tag{24}$$

'Re' denotes in Equation 24 that only the real part of the equation is used. Equation 22-Equation 24 are valid for all turbulence conditions. [17] uses the above model, but uses different equations for beam wander and spot size than [9].

The second model comes from [14] and models a horizontal beam, see Equation 25:

$$\sigma_I^2\left(\sigma_{pe,TC},L\right)_{\text{tracked}} = 3.86\sigma_R^2\,\text{Re}\left[i^{5/6}{}_2F_1\left(-\frac{5}{6},\frac{11}{6};\frac{17}{6};\bar{\Theta}+i\Lambda\right)\right] - 2.64\sigma_R^2\Lambda^{5/6}{}_1F_1\left(-\frac{5}{6};1;\frac{2\sigma_{pe,TC}^2}{W^2}\right), \tag{25}$$

where $\bar{\Theta} = 1-\Theta$, $\sigma_I^2\left(\sigma_{pe,TC},L\right)_{\text{tracked}}$ $[-]$ the longitudinal scintillation for a tip/tilt pre-corrected beam and $\sigma_{pe,TC}$ $[-]$ the tip/tilt pre-corrected pointing error variance, see Equation 26 [14]:

$$\sigma_{pe,TC}^2 = \left[\left(\langle r_c^2\rangle\right)^{1/2} - T_z L\right]^2\left[1-\frac{8}{9}\left(\frac{C_r^2W_0^2/r_0^2}{1+0.5C_r^2W_0^2/r_0^2}\right)^{1/6}\right], \tag{26}$$

where $\langle r_c^2 \rangle$ is computed with Equation 6 and T_z $[-]$ the two-axis Zernike tilt variance [43], [44] with:

$$T_z^2 = 0.32 \left(\frac{\lambda}{2W_0}\right)^2 \left(\frac{2W_0}{r_0}\right)^{5/3}. \tag{27}$$

Furthermore, the Fried parameter is computed with Equation 28 [14]:

$$r_0 = \left(0.16 C_n^2 k^2 L\right)^{-3/5}, \tag{28}$$

which is valid for horizontal links.

Lastly, Equation 26 uses the scaling factor C_r $[-]$. [14] uses a value of $C_r = 1.5\pi$ for horizontal links, which is therefore also used for this study.

The last model comes from [16], which also models a horizontal beam, see Equation 29:

$$\sigma_{I,l}^2(L)_{\text{tracked}} = 3.86\sigma_R^2 \,\text{Re}\left[i^{5/6} {}_2F_1\left(-\frac{5}{6}, \frac{11}{6}; \frac{17}{6}; \bar{\Theta} + i\Lambda\right)\right] - 2.64\sigma_R^2 \Lambda^{5/6}, \tag{29}$$

2) Radial Scintillation: Four equations are used to compare the radial scintillation. The first is again from [9], see Equation 30:

$$\sigma_I^2(\mathbf{r}, L)_{\text{tracked}} = 5.95\,(H - h_0)^2 \sec^2(\zeta) \left(\frac{2W_0}{r_0}\right)^{5/3} \times \left(\frac{\alpha_r - \sqrt{\langle \alpha_c^2 \rangle}}{W}\right)^2 \times U\left(\alpha_r - \sqrt{\langle \alpha_c^2 \rangle}\right) + \sigma_{I,l}^2(L)_{\text{tracked}}, \tag{30}$$

where $\sigma_I^2(\mathbf{r}, L)_{\text{tracked}}$ $[-]$ is scintillation index of a tracked beam, $U(x)$ $[-]$ a step function and α_r $[rad]$ the angular distance from the boresight:

$$\alpha_r = \frac{r}{L}, \tag{31}$$

where r $[m]$ is the radial distance from the boresight. Furthermore, the beam wander (Equation 5) angular distance from the boresight is defined as:

$$\sqrt{\langle \alpha_c^2 \rangle} = \frac{\sqrt{\langle r_c^2 \rangle}}{L}. \tag{32}$$

Lastly, in Equation 30 W is computed with Equation 11, r_0 with Equation 13 and $\sigma_{I,l}^2(L)_{\text{tracked}}$ with Equation 22. [17] uses the above model, but uses Equation 7 for beam wander, Equation 17 for spot size and for the Fried parameter Equation 8.

The second model with a horizontal beam is from [15], see Equation 33:

$$\sigma_I^2(\mathbf{r}, L)_{\text{tracked}} = 4.42\sigma_R^2 \Lambda^{5/6} \frac{r^2}{W_{ST}^2} + \sigma_{I,l}^2(L)_{\text{tracked}}, \tag{33}$$

where Λ_{ST} $[-]$ is the short-term, or instantaneous, Fresnel ratio, see Equation 34:

$$\Lambda = \frac{2L}{kW_{ST}^2} \tag{34}$$

and $\sigma_{I,l}^2(L)_{\text{tracked}}$ follows from Equation 22.

The third model is shown in Equation 35, which models a horizontal beam [16]:

$$\sigma_I^2(r, L)_{\text{tracked}} = \sigma_{I,l}^2(L)_{\text{tracked}} + 4.42\sigma_R^2 \Lambda_{ST}^{5/6} \frac{U\left(r - \sqrt{\langle r_c^2 \rangle}\right)\left(r - \sqrt{\langle r_c^2 \rangle}\right)^2}{W_{ST}^2}, \tag{35}$$

where $\sigma_{I,l}^2(L)_{\text{tracked}}$ is computed with Equation 29.

As the radial scintillation in section III, is only computed within the short-term spot size, also for the models described above, only radial values up to W_{ST} are included.

3) On-Axis Scintillation: For all radial scintillation models equations presented above, the scintillation at the boresight, or on-axis position can be computed as well. Following the theory presented on the on-axis location, it is proposed to compute the on-axis scintillation as follows:

$$\sigma_{I,\text{on-axis}}^2(L)_{\text{tracked}} = \sigma_I^2\left(\sqrt{\langle r_c^2 \rangle}, L\right)_{\text{tracked}}, \tag{36}$$

as the scintillation at the on axis point is equal to the radial scintillation at the radial distance equal to the beam centroid displacement, see Figure 5. Note that Equation 36 assumes zero pointing error.

For more information on the literature study performed and the research questions following from it, see Appendix A. A summary of the equations used in the comparison can be found in Table I.

TABLE I: Summary of equations used in the comparison.

Effect	**Variable**	**Model 1** [9] (divergent beam, slant path)	**Model 2** [14] (horizontal path)	**Model 3** [15] (horizontal path)	**Model 4** [16] (horizontal path)	**Model 5** [17] (collimated beam, slant path)
Beam Wander	$\langle r_c^2 \rangle$	Eq. 5	Eq. 6	Eq. 6	Eq. 6	Eq. 7
Long-term beam spread	W_{LT}	Eq. 9	Eq. 14	Eq. 16	Eq. 16	Eq. 17
Short-term beam spread	W_{ST}	Eq. 19 & Eq. 5 & Eq. 9	Eq. 19 & Eq. 6 & Eq. 14	Eq. 19 & Eq. 6 & Eq. 16	Eq. 19 & Eq. 6 & Eq. 16	Eq. 19 & Eq. 7 & Eq. 17
Longitudinal scintillation	$\sigma_{I,0}^2$	Eq. 22	Eq. 25	Eq. 22	Eq. 29	Eq. 22
Radial scintillation	$\sigma_{I,r}^2$	Eq. 30 & Eq. 5	None	Eq. 33	Eq. 35	Eq. 30 & Eq. 7
On-axis scintillation	$\sigma_{I,on-axis}^2$	Eq. 30 & Eq. 5	None	Eq. 33 & Eq. 6	Eq. 35 & Eq. 6	Eq. 30 & Eq. 7

III. Methodology

In this section the test setup used to experimentally verify the theoretic models is described (subsection III-A) along with the data analysis performed (subsection III-B).

A. Test Setup

A schematic representation of the test setup is shown in Figure 6. The test setup is closely related to [45], see Figure 6. A ∼10 km ground-to-ground link is under consideration. The Ground Terminal Breadboard (GTB) is placed at the test site near Cabauw. In the Gerbrandy Tower, at 226 m altitude the Beam Profiler (BP) is placed. A beacon is sent from the BP to the GTB. The GTB measures the wavefront error and angle of arrival of the received beacon, as it has been disturbed by the turbulent atmosphere. These measurements are used to pre-correct the tip/tilt of the uplink, Gaussian beam. The idea is that the turbulent atmosphere distorts the uplink beam again, such that it arrives at the Beam Profiler, as it is pre-corrected to account for the tip/tilt distortion. The transmit laser beam has a wavelength of 1553 nm and a divergence half-angle of 18 μrad. Furthermore, four Turbulence Monitors (TMs) have been placed along the link, which measure the turbulence structure parameter C_n^2. Two are placed on top of the Gerbrandy tower platform and two are placed near the GTB. These turbulence monitors are sonic anemometers, see Figure 7. Furthermore, all data of the GTB, BP and TMs is synchronized via satellite.

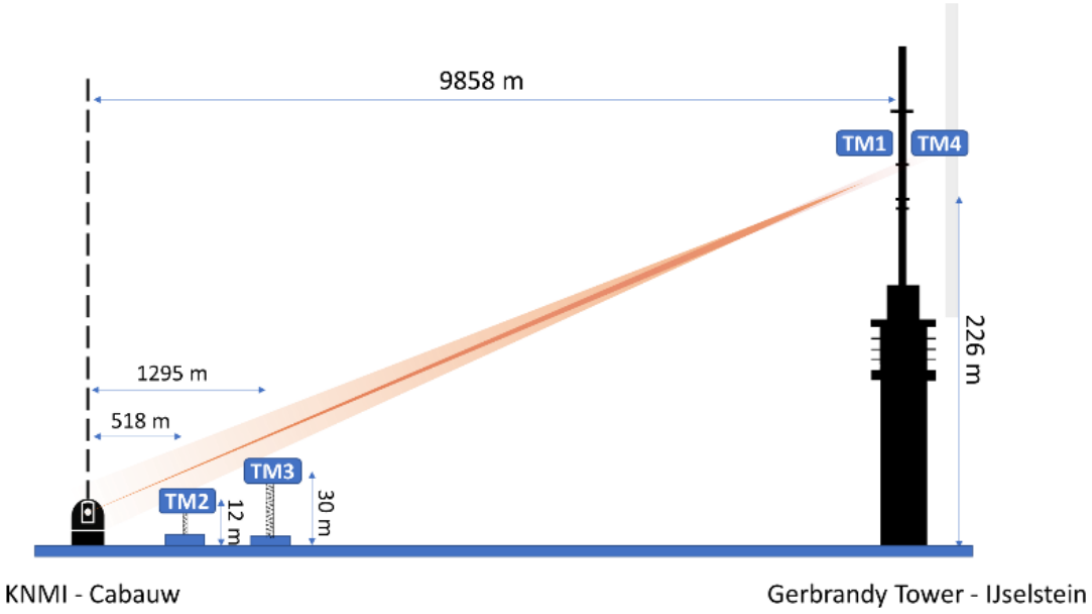

Fig. 6: Schematic representation of the test setup [45].

The GTB, see Figure 8, contains an adaptive optics system. As the goal is to investigate the impact of turbulence on the optical laser link, a continuous power of 0.2 W is used without any communications protocols enabled.

The BP consists of a 50 cm aperture Newtonian telescope, to which an infrared imager camera is attached, see Figure 9c. The pupil plane is imaged, which produces an intensity profile of the beam at 10 km from the transmitter. This information is used to compare the data to the parameters as presented in section II. The image detector (Xenics Cheetah 800 Hz) has a frame rate of 800 Hz and a used image size of 512x512 pixels. Furthermore, a laser beacon is placed on the front, which is aligned with the boresight of the telescope. An image of the setup in the Gerbrandy tower is shown in Figure 9a. An image of the beacon assembly attached to the BP is shown in Figure 9b.

Fig. 7: Turbulence monitor placed on top of crane with sonic anemometer on the left side of the T-post.

Fig. 8: Ground Terminal Breadboard at the test site.

A frame of one of the measurements is shown in Figure 10. The spot is clearly visible in the top left area. In the center the secondary mirror with the beacon on top are visible. The beacon is placed on top, as that position allows for alignment with the line of sight of the telescope. Lastly, the spider strut holding the secondary mirror in place is visible.

Next to this, there are diffraction patterns visible in the image, indicating a slight defocus. The defocus has been found to be to 32 m, and thus the link in the analysis has been adjusted by this distance. m

The BP recorded measurements spanning $\sim$2 s. The test ran from 29/07/2022 until 01/08/2022. In total 1651 measurements are used in the analysis. For more information on the test setup refer to Appendix C.

B. Data Analysis

The goal of the data analysis is to find experimental values for the variables described by the theory in section II. The most important components of the data analysis are presented below.

1) Turbulence Profile: The data of the turbulence monitors is processed to retrieve C_n^2 values, which in term are used to create a turbulence profile for the link. The used data consists of a time stamp, a C_n^2 value and wind direction. The latter two are computed from raw averaged data over a one minute interval [46]. This has been done to eliminate any outliers and to provide a more consistent profile, while at the same time allowing for temporal variations.

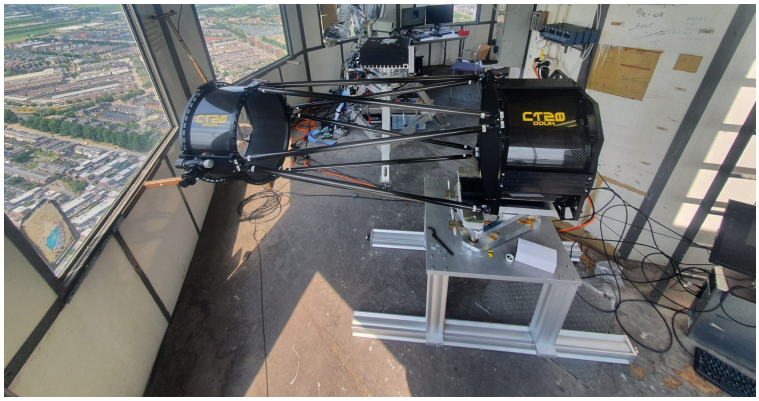

(a) Beam Profiler set up in the Gerbrandy Tower.

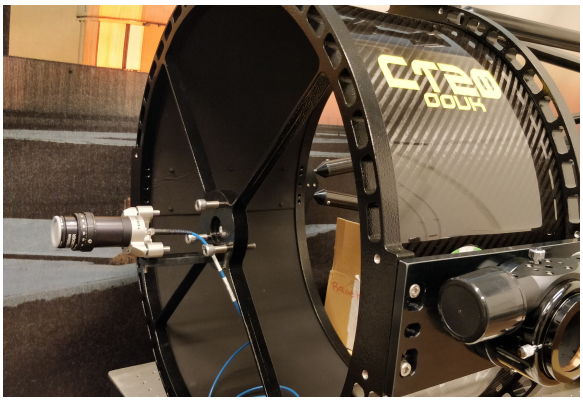

(b) Beacon assembly attached to the telescope in the lab.

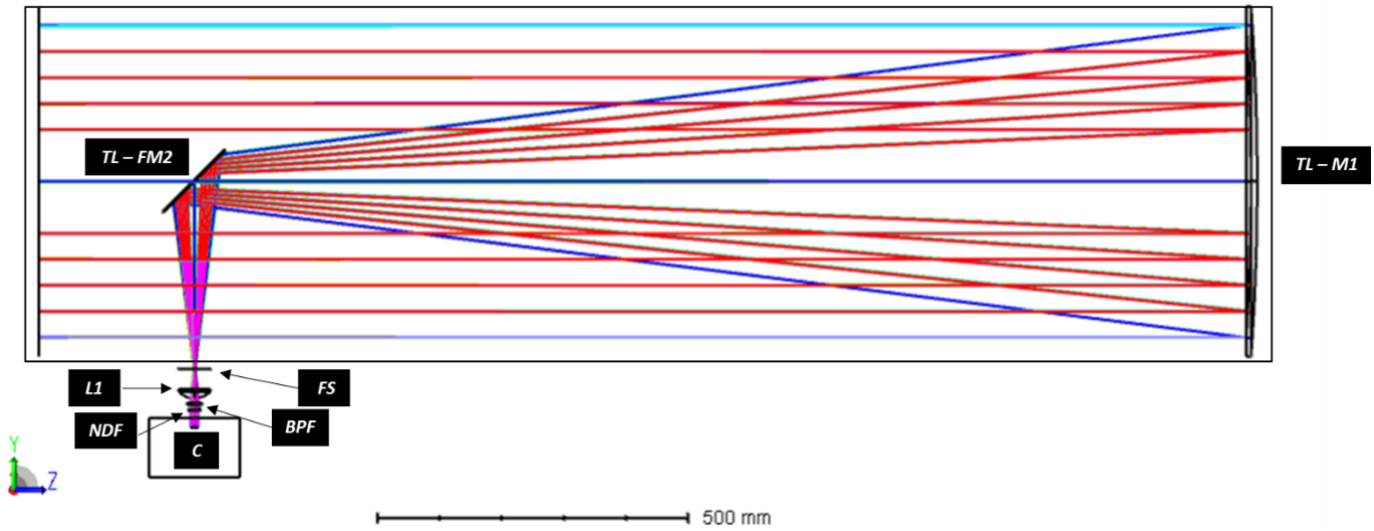

(c) Optical layout of the Telescope and Imager subsystem of the Beam Profiler: TL - telescope, M1 - primary mirror, FM2 - secondary mirror, FS - focal stop, L1 - lens, BPF - bandpass filter, NDF - neutral density filter, C - camera/imager.

Fig. 9: The Beam Profiler.

The link is split up in intervals, for which a C_n^2 value is computed, see Figure 11. Linear interpolation between the retrieved TM C_n^2 values is used for the path TM 2-TM 3 and TM 3-TM 1/TM 4, while a constant value is used for the path TM 2-ground, as there is too little information available to measure the C_n^2 values in between the measurement locations.

To avoid wind shadowing of the tower mast, TM1 and TM4 were mounted with a 90°offset. To select the correct turbulence monitor for turbulence profile creation, the wind direction of TM3 is used to roughly indicate the wind direction at the tower during the measurement period. This way the TM data influenced least by the tower structure can be used for each respective measurement.

To plot the turbulence effects, such as beam wander variance against the turbulence conditions, a single value must be used for a measured turbulence profile. The median of the C_n^2 values in each interpolated profile is used to achieve a more consistent variance in turbulence values, which are influenced less by the individual measurement points along the link.

These turbulence profiles are also used as input for the theory presented in section II.

2) Mask: To analyze the image only those parts are included, which receive light. Due to beam jitter the image moves slightly along the 512x512 image grid. Thus, the mask is slightly larger than the instantaneous obscuration and smaller than the total aperture. This way, the mask excludes any jittering of the image. The resulting mask is shown in Figure 12, where the white part is included and all other pixels are excluded from the analysis.

3) Beam Wander: The longitudinal position of the beam (beam center) is determined via a center of gravity computation of the intensity. The equation used for this is Equation 37:

$$\bar{x} = \frac{\int_{-\infty}^{\infty}\int_{-\infty}^{\infty} I(x,y)x dx dy}{\int_{-\infty}^{\infty}\int_{-\infty}^{\infty} I(x,y) dx dy}, \tag{37}$$

where $\bar{x}$ $[m]$ is the horizontal spot center location. The vertical spot center location ($\bar{y}$) is determined analogously, but for y.

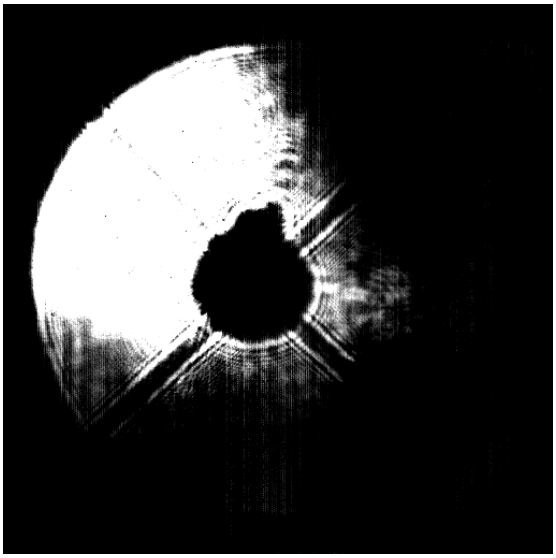

Fig. 10: A snapshot of a measurement with the spot, spider strut, secondary mirror and beacon on top of the secondary mirror visible.

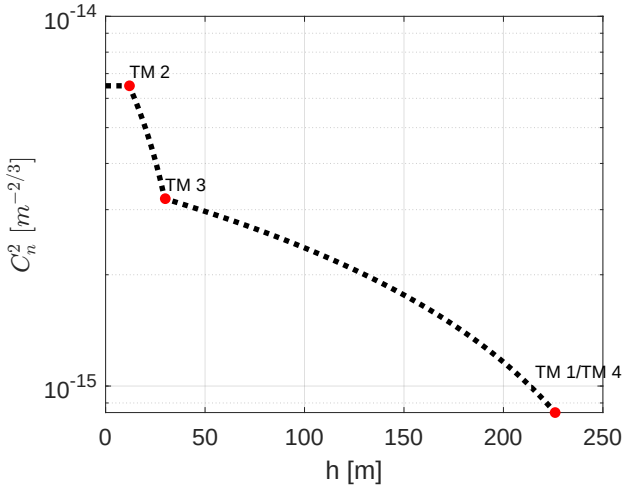

Fig. 11: C_n^2 profile for a measurement, created from Turbulence Monitor data. The C_n^2 values at the red points are measured by the Turbulence Monitors, while the dashed line consists of interpolated values.

The beam wander variance is computed relative to the average hot spot position of a respective measurement to retrieve $\langle r_c^2 \rangle$. Note that the value retrieved for the beam wander also includes a system and beam jitter component.

4) Spot Size: The instantaneous spot size is determined with the second-moment width ($D4\sigma$), as in the past it has been found to be a robust way of retrieving a spot size under influence of scintillation [40]. This spot diameter for the horizontal direction is computed as in Equation 38 [47].

$$D4\sigma_x = 4\sigma = 4\sqrt{\frac{\int_{-\infty}^{\infty}\int_{-\infty}^{\infty} I(x,y)(x-\bar{x})^2 dxdy}{\int_{-\infty}^{\infty}\int_{-\infty}^{\infty} I(x,y)dxdy}} \tag{38}$$

where $D4\sigma_x$ $[m]$ is the second-moment width. The vertical spot size ($D4\sigma_y$) is determined analogously. Therefore, this method allows for analyzing elliptically-shaped beams in horizontal and vertical direction. Though, to compare the results to the theory in section II, which assumes perfectly circular Gaussian beams, the mean of the mean horizontal and vertical spot size is used.

The result is converted into the more commonly used $1/e^2$ spot radius via Equation 39:

$$w = \frac{\sqrt{2}D4\sigma}{4}, \tag{39}$$

where w $[m]$ is the $1/e^2$ radius. For the derivation of this conversion refer to Appendix D-E.

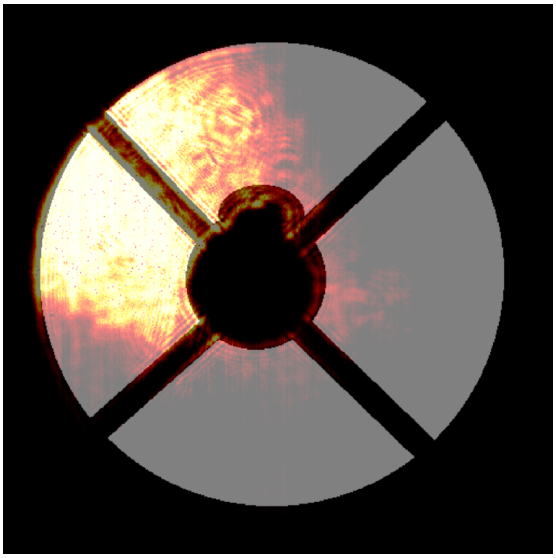

Fig. 12: Mask (white) overlaid on colored data.

The long-term spot size is computed following the definition of Equation 19. Note that in the theoretical models the long-term spot size and beam wander are computed to arrive at the short-term spot size (Equation 19). In the data analysis, the short-term spot size and beam wander are computed to arrive at the long-term spot size.

5) Obscuration & Clipping: As the secondary mirror and laser beacon partially obscure the beam, while the telescope aperture can clip the spot, Equation 37 and Equation 38 lead to inaccuracies. As all other performance parameters retrieved in the data analysis are dependent on the spot location, it is of paramount importance to improve the accuracy of the center of gravity computation.

The proposed solution is to make use of a lookup table (LUT), which relates the clipped and obscured data computed to an unbound, simulated image. The LUT is based on the use of a Gaussian spot, of which the size and location are known.

The conversion works as follows: first an imaged spot is simulated using the Gaussian intensity equation. The mask is used to compute the obscured and clipped result with Equation 37 and Equation 38, which leads to the link between an unbound spot and a masked one. In the data analysis this conversion is reversed to reduce the effect of clipping and obscuration.

The grid on which the spots are simulated is larger than the Beam Profiler image grid (512x512 pixels) to allow for wander of the imaged spot outside of the standard grid. The configuration of the simulated spots are summarized in a three-dimensional array ($n \times n \times m$) of which all combinations are used as LUT entries, see Table II:

TABLE II: Settings used for the creation of the lookup table

	# Entries	**Range**
# Spots x	88	1-768 pix
# Spots y	88	1-768 pix
Spot size x	4	23.75-48.75 cm
Spot size y	4	23.75-48.75 cm

The LUT is interpolated using Delaunay triangulation. The equations used to create (elliptical) Gaussian beams are presented in Appendix D-F1.

This method has been verified for a Gaussian spot. The LUT can predict the size and location of a perfect Gaussian spot for its full working range within 0.004 m and 0.002 m accuracy, respectively. Note that the LUT can only use the intensity values available. Any obscured or clipped hot spot cannot be used in the analysis. If input values lie outside the LUT, it is not included in the analysis. The total amount of excluded frames in the data analysis lies at 4.6%. The verification can be found in Appendix D-F2.

Examples of the retrieved LUT results are shown in Figure 13. Looking at the test data reveals that above a C_n^2 value of 5E-15 $m^{-2/3}$ the beam starts to break up significantly, see Figure 13d. Therefore, the LUT analysis is only performed for $C_n^2 \leq$ 5E-15 $m^{-2/3}$, see Figure 13c.

6) Scintillation: The scintillation analysis is executed after the lookup table has estimated the spot size and location. It uses the spot location and size resulting from the LUT.

For the longitudinal scintillation analysis, the intensity values of the spot center location are collected. Then, for a complete measurement, the longitudinal scintillation index is computed via Equation 20.

For the on-axis scintillation a static point is used. The on-axis location has been found by computing the average hot spot location for the 100 measurements with the lowest median C_n^2 value. A mask with a diameter of 1.1 cm is used to gather the

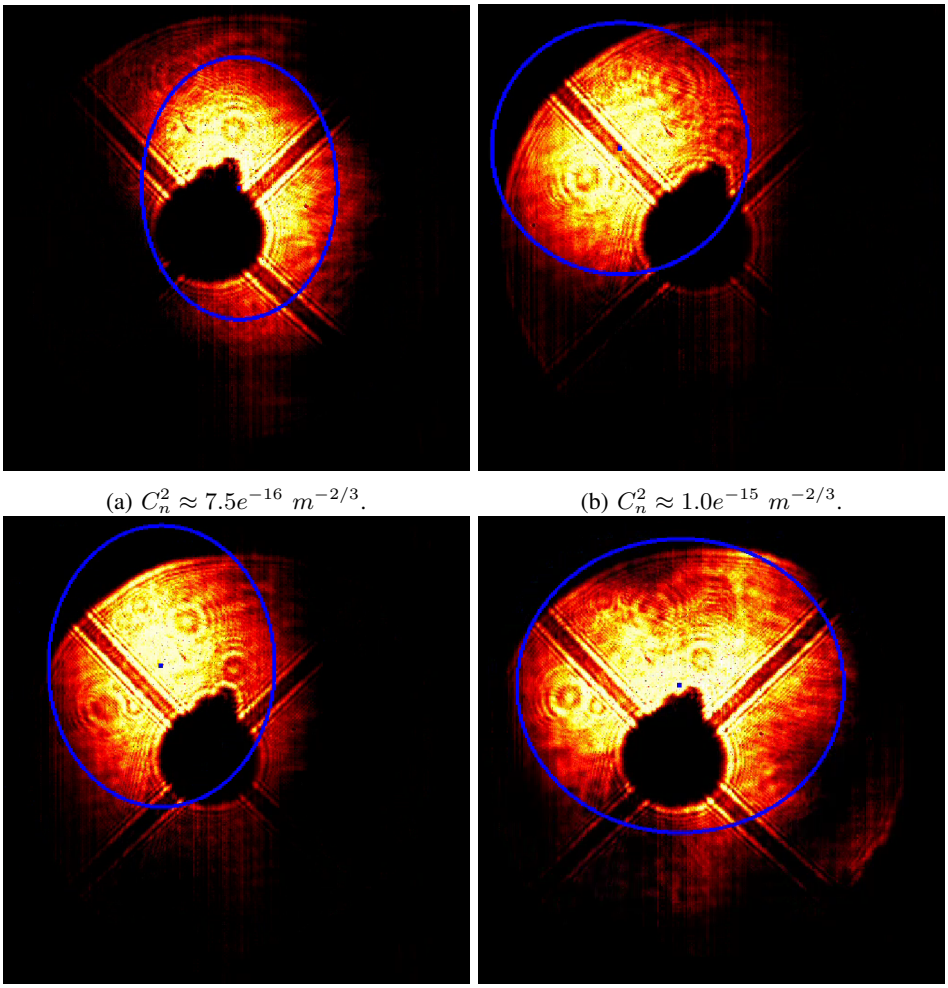

(a) $C_n^2 \approx 7.5e^{-16}\ m^{-2/3}$. (b) $C_n^2 \approx 1.0e^{-15}\ m^{-2/3}$.

(c) $C_n^2 \approx 5.0e^{-15}\ m^{-2/3}$. (d) $C_n^2 \approx 1.0e^{-14}\ m^{-2/3}$ (excluded).

Fig. 13: Still frames of data with estimated spot size (blue ellipse) and spot center (blue dot) by the lookup table.

intensity per frame, which simulates a satellite receiver, see Figure 5. Again the gathered intensity values are used to compute the on-axis scintillation via Equation 20.

As the radial intensity is a vector along radial direction, the scintillation is computed using the intensity values of the instantaneous spots in radial direction. In the theoretical models the radial scintillation vector is equal for all rotational angles in the spot. However, in practice this is not the case and thus multiple vectors are used: a vector in positive and negative horizontal and vertical direction, which match the axes of the spots used in the lookup table. These orientation vectors have the longitudinal point as origin and follow the reference frame of the wandering spot.

Note that the orientation of the vectors is chosen such, because the horizontal wind direction in the field test, cause the spot to change shape in vertical and horizontal direction. By aligning the vectors with the changing shape of the measured spot, the accuracy is improved.

The scintillation index is then computed for each vector. To present the radial scintillation index for varying turbulence strength, the median value of the 4 vectors is used, which filters out any erratic scintillation values at the fringes of the spot.

IV. Results

For the comparison, the GTB beam parameters and the measured turbulence profiles are used as input for the theoretical models. The models are split up in two parts. For one part, the models are completely valid for the turbulence conditions along the path. For the other part, the models are invalid for all turbulence conditions along the path. The latter are presented as lines with a low opacity. Turbulence conditions where the models are only partially valid are not included, as it reduced the clarity of the figures.

As various turbulence profiles can have equal median C_n^2 values, a spread occurs for the theoretical models for slanted paths which are not valid outside the weak turbulence regime. Therefore, the median results for the models is used in the comparison to indicate the general trend of the model outside their validity range.

A. Beam Wander

The analyzed beam displacement for a measurement is shown in Figure 14. As can be seen the beam displacement follows a Gaussian distribution as is expected from theory [9]. Together with the performance shown in Figure 13, this reassures the accuracy of the lookup table when used for a spot under the influence of scintillation.

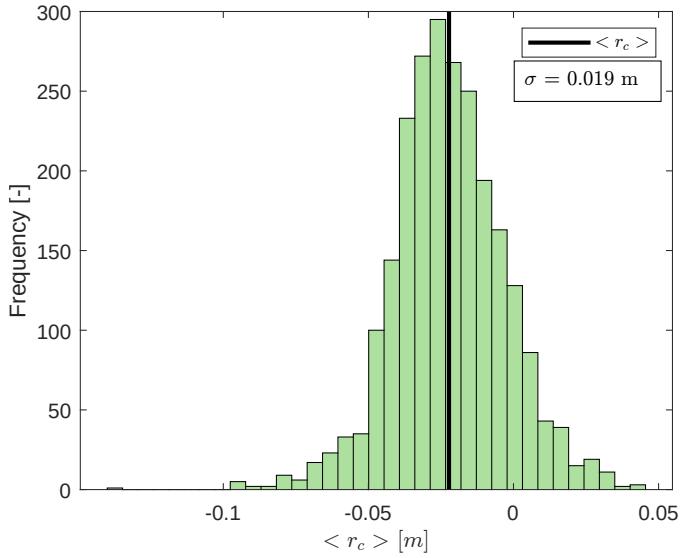

Fig. 14: Beam displacement histogram for a measurement ($C_n^2 \approx 1.2e^{-15}\ m^{-2/3}$).

The results for the beam wander variance are shown in Figure 15. Note that the theoretic models show the results for an untracked beam. The test results are for a tip/tilt pre-corrected beam, but also include a system and beam jitter component. Thus, the actual beam wander encountered in the field test lies lower than presented here.

As can be seen, the beam wander variance in the test is lower than the theoretical models, showing the effectiveness of the tip/tilt pre-correction. The average beam centroid movement over the 10 km test path equals $\sim$ 4 cm. The empirical beam wander variance does also not increase much for increasing turbulence strength. The low slope may indicate that the measured beam movement is mainly a result of jitter and not atmospheric induced turbulence. Next to this, it can be seen that the validity range of the models is limited with respect to the measured turbulence conditions, especially as the empirical results in Figure 15 are only included for $C_n^2 \leq$ 5E-15 m$^{-2/3}$.

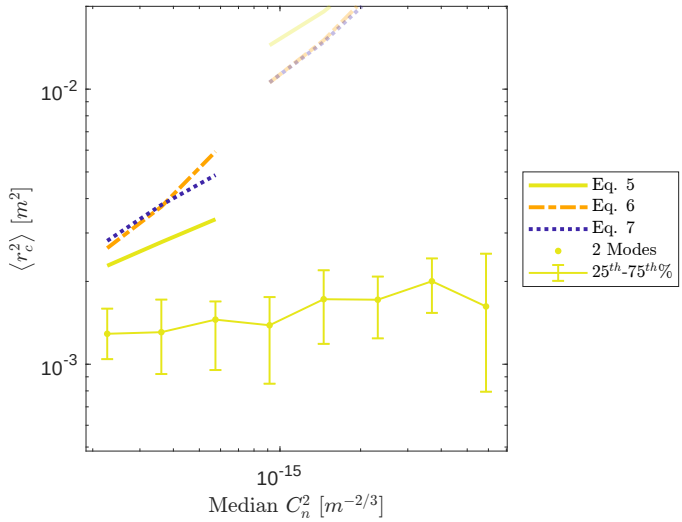

Fig. 15: Empirical beam wander variance results along with theoretical models for an untracked beam. The faded lines are for those parts of models not valid outside the Rytov approximation range.

B. Spot Size

1) Long-Term Spot Size: The long-term spot size results are shown in Figure 16. As can be seen the theoretical results for an untracked beam predict an increase in the long-term spot radius. However, as the beam is tracked, see Figure 15, the empirical

long-term spot size does not increase much with turbulence strength. The difference between the empirical and theoretical results grows to a factor 2.5 for strong turbulence conditions.

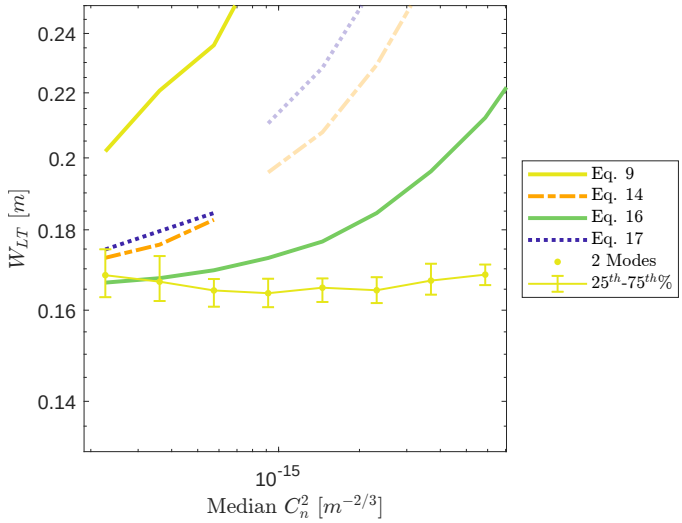

Fig. 16: Empirical long-term spot size results along with theoretical models for an untracked beam. The faded lines are for those parts of models not valid outside the Rytov approximation range.

2) Short-Term Spot Size: The histogram of the measured instantaneous spot size is shown in Figure 17. The beam breathing can be seen in its Gaussian distribution. Furthermore, for this measurement the mean spot size lies slightly below the expected free-space spot size W. However, the difference is not of a significant amount (1.2%).

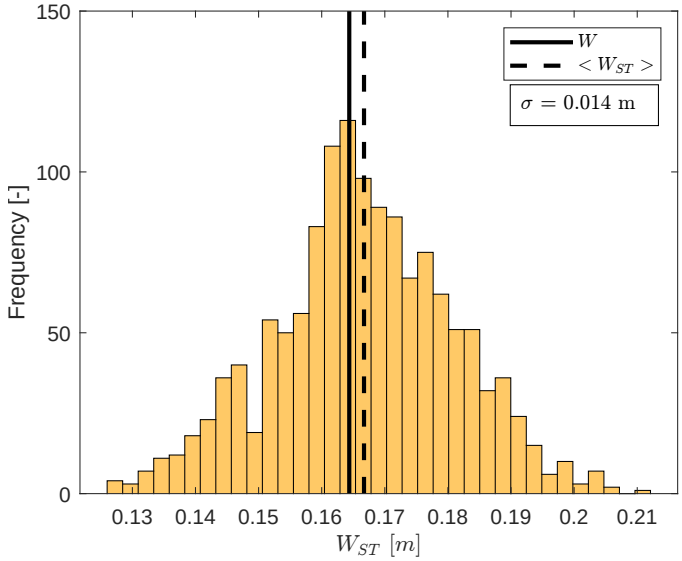

Fig. 17: Spot size histogram for a measurement ($C_n^2 \approx 1.2e^{-15}\ m^{-2/3}$).

The short-term spot size results are compared to the theory for an untracked beam in Figure 18. In this figure also the free-space spot size is plotted. Both empirical and theoretical results lie close in magnitude. As can be seen the spot size in the test does not significantly change for increasing turbulence strengths up to C_n^2 =2E-15 m$^{-2/3}$. It even decreases for part of the turbulence regime, even if it is not of a significant amount (2.5%). This might be the result of minor inaccuracies in the test setup and data analysis. However, it has been verified by inspecting of the individual measurements that the spot size indeed does not grow for stronger turbulence conditions up to C_n^2 =2E-15 m$^{-2/3}$, even though some theory predicts this. This can also be seen in Figure 13. Furthermore, the spot is sufficiently captured in the measurements to be analyzed by the methods in section III. For C_n^2 values above 2E-15 m$^{-2/3}$, the spot size does start to increase. Thus, the mean spot size retrieved in the field test starts to significantly increase in radius at higher C_n^2 values compared to the theoretical results.

For C_n^2 values above 5E-15 m$^{-2/3}$ the spot breaks up. However, this cannot be accurately analyzed with methods used in the analysis, as the LUT method assumes a Gaussian spot without break up. Therefore, those measurements are not included in the analysis.

Next to this, the short-term spot size is on average equal to the free-space spot size for the lowest turbulence conditions. As this outcome matches expectations, it additionally verifies the accuracy of the data analysis for weak turbulence conditions.

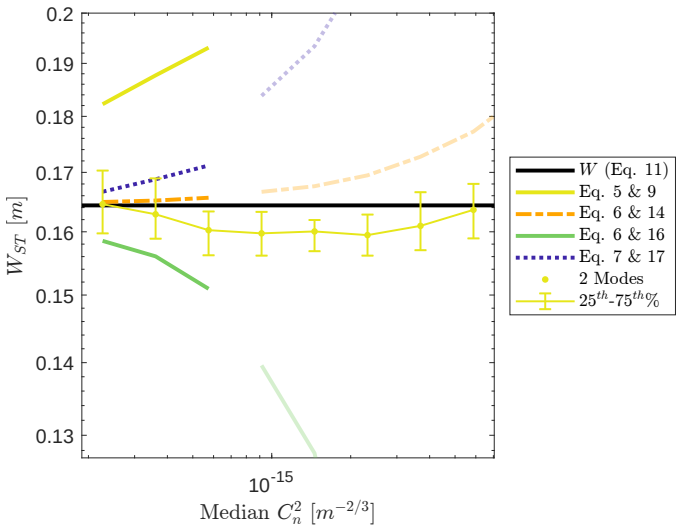

Fig. 18: Empirical short-term spot size results along with theoretical models. The faded lines are for those parts of models not valid outside the Rytov approximation range.

C. Scintillation

1) Longitudinal Scintillation: The longitudinal scintillation index results are shown in Figure 19. As can be seen, all theoretical models predict the same results. The empirical and theoretical results lie close for weak turbulence conditions, within a factor 1.5 difference. For strong turbulence conditions the test results do not increase as much for increasing turbulence strengths as the theory predicts. For strong turbulence conditions the difference between theoretical and empirical results grows up to a factor 4.

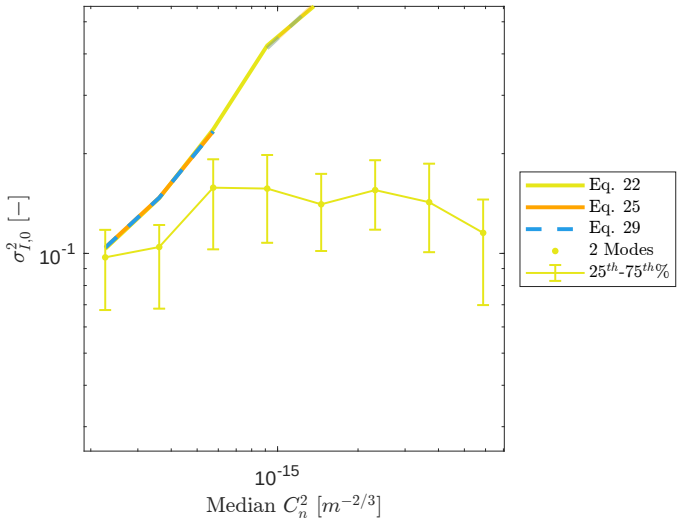

Fig. 19: Empirical longitudinal scintillation results along with theoretical models. The faded lines are for those parts of models not valid outside the Rytov approximation range.

2) Radial Scintillation: The radial scintillation results across the spot for a measurement are shown in Figure 20. Note that, the horizontal axis is not symmetrical as the on-axis location is not centered in the image. As can be seen, the scintillation in the spot center is lower for the empirical results. The theoretical models are for a perfectly tracked beam, while this cannot be achieved in reality. Still, the empirical results are of a smaller magnitude than the theoretical models predict. This is especially true for moderate/strong turbulence conditions.

Furthermore, the bucket shape predicted by Equation 30 and Equation 33 can also be seen in the empirical data. Next to this, the width of the bathtub shape of theoretical and empirical results is comparable. In the empirical results the scintillation index increases at a faster rate with radial distance than the results of theoretical models.

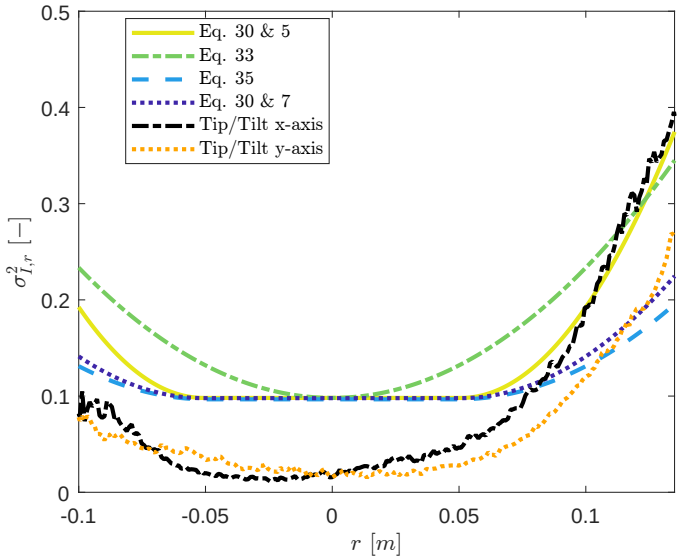

Fig. 20: Radial scintillation results in the imaged pupil plane for a measurement ($C_n^2 \approx 1.2e^{-15}\ m^{-2/3}$).

Figure 21 shows the median radial scintillation results for theoretical models and the field test. As can be seen the theoretical models can differ a factor ∼2.5, with respect to each other. Especially, Equation 35 matches closely with the empirical results, as they lie within a factor 1.5 difference.

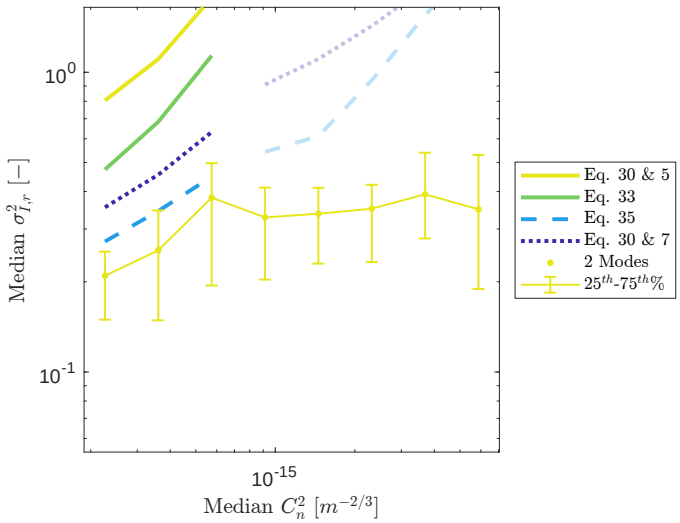

Fig. 21: Empirical radial scintillation results along with theoretical models. The faded lines are for those parts of models not valid outside the Rytov approximation range.

3) On-Axis Scintillation: The received on-axis power histogram for a measurement is shown in Figure 22. The variation in received power is a result of beam wander (Figure 14), changing spot size (Figure 17) and scintillation.

The on-axis scintillation results are shown in Figure 23. The theoretical results of Equation 30 are equal to its longitudinal results of Equation 22 shown in Figure 19, as its step function is not included in the results due to the definition of the on-axis scintillation index, see Equation 36.

As can be seen, for weak turbulence conditions the theory and empirical results are in the same range. For moderate/strong turbulence conditions, the on-axis scintillation index is smaller than predicted by theory, but still lies close to the the theoretical results. The maximum difference lies within a factor 2.5. Therefore, the results between theory and field test lie closest for the on-axis scintillation index over the full analyzed turbulence conditions range.

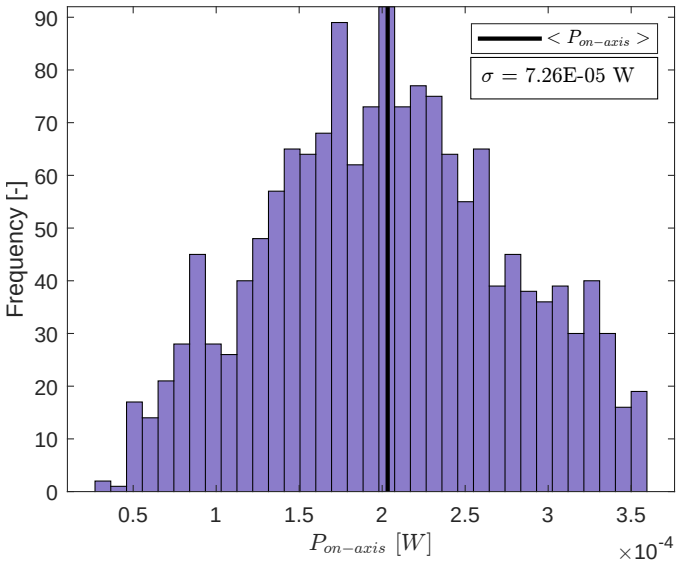

Fig. 22: Received on-axis power histogram for a measurement ($C_n^2 \approx 1.2e^{-15}\ m^{-2/3}$).

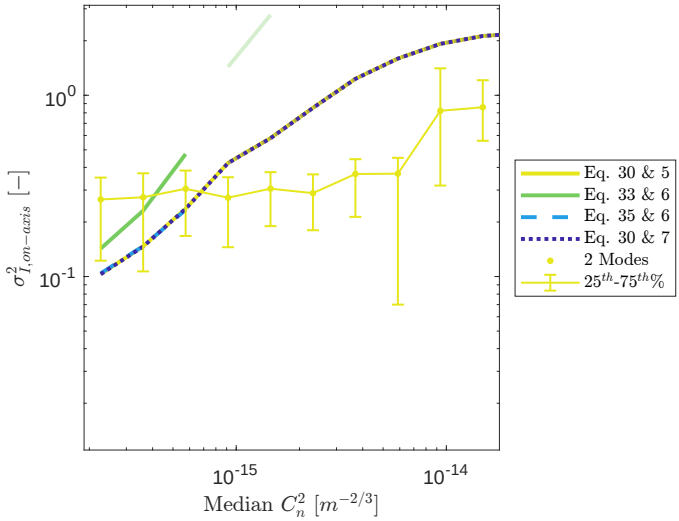

Fig. 23: Empirical on-axis scintillation results along with theoretical models. The faded lines are for those parts of models not valid outside the Rytov approximation range.

V. Discussion

In [9], [14]–[16], simulations are presented to verify the theory presented in section II under weak turbulence conditions. As can be seen in section IV, the theoretical and empirical results match closely for this turbulence regime. The results in section IV show an increasing deviation between the theoretical and empirical results for increasing turbulence strengths, while most measurements fall in this turbulence strength regime.

A note to address is the representation of the results. The results contain measurements which have been recorded for all times of day. As the turbulence profile structure differs significantly between day and night time, this is also found back in the results. The upper limit of the empirical results consists mainly of measurements recorded during the day, while the lower limit consists mostly of night time measurements. As the theory does not differentiate between time of day, this has also not been implemented in the comparison here.

Next to this, two other factors influence the results. Firstly, the wind speed plays a role: Higher wind speeds result in speckles drifting through the laser link quicker, which leads to a higher scintillation index, as the measurement time is only two seconds. Secondly, as the test has a nearly horizontal path, the wind direction is of influence: If the wind is aligned with the link, the speckles seem to be stagnant in the image, as they drift along the path. This leads to a low scintillation index. If the wind blows orthogonal to the link, the speckles drift through the link and thus the scintillation index is higher than for a parallel wind direction. Again, as the theory does not implement these terms, they are also omitted in the comparison.

The difference between results for theory and field test can also be partially the result of the way the C_n^2 profiles have been created. The turbulence strength has been measured on three points along the link. Between these three points the C_n^2 will have deviated from the linearly interpolated values used for the theory. Furthermore, the results of the turbulence monitors placed on the Gerbrandy tower have been influenced by the tower's structure.

Next to this, the limited aperture and the obscuration of the Beam Profiler limit the accuracy of the data analysis. The instantaneous spot intensity profiles are incomplete as a result of these effects. The location and size of the spot are estimated with the LUT, but the loss of information of the intensity values cannot be retrieved. Furthermore, the LUT is based on a perfect Gaussian spot, while in reality scintillation is present. The hot spots caused by scintillation reduce the accuracy of the spot location and size estimation.

To the authors' knowledge, in the existing body of literature the individual effect of turbulence towards beam wander and beam spread have not been experimentally compared to theoretical results. However, there is literature on empirical verification of the on-axis scintillation index available. Firstly, [29] measures a higher on-axis scintillation index for its 600 m link than retrieved on this test. However, the transmitter in [29] does not pre-correct the beam while at the same time utilizing a small beam diameter, which generally leads to higher scintillation index [16]. Secondly, Dunphy 1973 [30] measures a scintillation index in the same order as retrieved in this paper. The results in [30] are for a highly divergent beam over a 6 km path, resulting in a received spot multiple times larger than the expected beam wander. This means, that the measured scintillation index for the untracked beam in [30] is comparable to the longitudinal/on-axis scintillation index for a tracked beam in this paper. As the radial scintillation index close to the spot center is close in value to the longitudinal scintillation index (Figure 20), the similarities between the measurements in [30] and this paper are expected. Lastly, in some papers the theoretical results are fitted to the measured scintillation index and received power in [39] and [17], respectively. Those fitted results show that the theory can be effective for weak turbulence conditions, which is a crucial step. The results in this paper show that there is solid ground to accept the theory to be effective for predicting the effects under consideration for weak turbulence conditions.

VI. Conclusion

An experiment has been carried out to retrieve values of the individual effects atmospheric turbulence has on an optical link. The effects under consideration are: beam wander, beam spread and scintillation. By retrieving these values, the accuracy of the relations, which describe the influence of atmospheric turbulence on optical propagation, can be verified. This way this research also aids in the development of future optical communications systems.

In the field test the spot of a 10 km, tip/tilt pre-corrected, uplink beam is captured by a 0.5 m aperture Newtonian telescope at 800 Hz. Furthermore, the turbulence conditions are logged simultaneously. The spot locations and sizes are retrieved by a center of gravity of the intensity and second-moment width, respectively. Unfortunately, the measurements are influenced by an obscuration and limited aperture size. However, by utilizing a lookup table the influence is reduced.

By using the measured turbulence profiles and settings of the Ground Terminal Breadboard, the theoretical results have been retrieved for similar conditions as encountered during the field test. The empirical results have been compared to the theoretical results.

The beam wander in the field test is shown to be reduced significantly by tip/tilt pre-correction with respect to the theory for an untracked beam. Even though the measured tracked beam wander variance also contains a system and beam jitter component, it still at minimum a factor two smaller than the theoretical results for an untracked beam.

While the theoretical short-spot size increases in radius for increasing turbulence strength already in the low turbulence regime, the short-term spot size retrieved in the test only significantly increases in radius in the moderate-to-strong turbulence regime. Up until that point the empirical short-term spot size is equal to the free-space spot size. The long-term spot size follows the results of the short-term spot size. Thus, the empirical and theoretical results lie close for weak turbulence conditions, but differ significantly for strong turbulence conditions, where they can differ up to a factor 2.5.

The scintillation index is split up in three different variables: longitudinal (instantaneous spot center), radial along the short-term spot and on-axis (boresight). For each location or range, the scintillation index is computed using the intensity values over time.

The theoretical and empirical longitudinal and radial scintillation indices are comparable in magnitude and slope for the weak turbulence regime. The theoretical and empirical longitudinal and radial scintillation indices differ up to a factor 1.5 for weak turbulence conditions. For stronger turbulence conditions the difference between theoretical and empirical results grows up to a factor 4 for the longitudinal scintillation index. Furthermore, the bucket shape for the radial scintillation index along the spot predicted by theory, is also seen in the empirical results. For the on-axis scintillation the empirical and theoretical results lie closest for the full range of analyzed turbulence conditions: the maximum difference lies within a factor 2.5.

For all variables, except on-axis scintillation only measurements with a median C_n^2 value below 5E5 $m^{-2/3}$ are included in the analysis, as for higher turbulence strengths beam break up prevents analysis of the spot with the methods used in the test. For on-axis scintillation a fixed point in the aperture is used, of which the analysis is thus not influenced by beam break up.

There are several factors limiting the accuracy of the data analysis: the obscuration and clipping, limited amount of Turbulence Monitors along the path and the measurement time of two seconds. The obscuration and clipping lead to a loss of information. This loss of information has been bypassed by the lookup table, but it can never reproduce the data nor be fully accurate.

Furthermore, the variance in empirical results for equal turbulence conditions is larger than for the theoretical results. Wind direction, time of day and wind speed are not included in the theoretical equations, while analysis of the empirical results spread shows that these are of influence on the variance of empirical results for equal turbulence conditions.

Concluding, by comparing theory and measurements for equal beam parameters and approximately equal turbulence conditions, an indication is given of the similarities and differences between these for varying turbulence conditions. The similarities for weak turbulence conditions strengthen the confidence in the theory for those conditions, while the dissimilarities for strong turbulence conditions ask for more research to understand the effect of atmospheric turbulence on optical propagation, especially for strong turbulence conditions.

ACKNOWLEDGMENT

This research is part of the the European Space Agency's Scylight programme. The authors would like to thank ESA for the opportunity to perform this research.

Furthermore, there are several individuals to be thanked for their contribution to the research. Firstly, thanks to T. Hooftman for the mechanical design of the Beam Profiler. Secondly, we would like to thank Y. Vos for the setup and alignment of the Beam Profiler during the field test. Thanks to E.P. Veldhuis and A.P.C. Oosterwijk for the processing of the Turbulence Monitor data. Lastly, thank you N.J. Doelman, C.W. Korevaar, M.Pierzyna and J.R. Reynal for the fruitful discussions.

REFERENCES

[1] ESA. ScyLight (https://www.esa.int/Applications/Telecommunications_Integrated_Applications/ScyLight).
[2] ESA. TOmCAT - Terabit Optical Communication Adaptive Terminal (https://artes.esa.int/projects/tomcat). 3 2023.
[3] H. Hemmati, A. Biswas, and D. M. Boroson. 30-dB data rate improvement for interplanetary laser communication. page 687707, 2 2008.
[4] Frank F. Heine, Patricia Martin-Pimentel, Nils Höpcke, David Hasler, Christoph Rochow, and Herwig Zech. Status of Tesat Lasercomms activities. In Hamid Hemmati and Don M. Boroson, editors, *Free-Space Laser Communications XXXIII*, page 8. SPIE, 3 2021.
[5] ESA. ARTES ScyLight - Work plan (https://artes.esa.int/artes-scylight-work-plan), 7 2020.
[6] Kendall Murphy. What's Next: The Future of NASA's Laser Communications (https://www.nasa.gov/feature/goddard/2022/the-future-of-laser-communications), 1 2023.
[7] S. Poulenard, M. Ruellan, B. Roy, J. Riédi, F. Parol, and A. Rissons. High altitude clouds impacts on the design of optical feeder link and optical ground station network for future broadband satellite services. page 897107, 3 2014.
[8] Morio Toyoshima, Hideki Takenaka, Yozo Shoji, and Yoshihisa Takayama. Frequency characteristics of atmospheric turbulence in space-to-ground laser links. In *Atmospheric Propagation VII*, volume 7685, page 76850G. SPIE, 4 2010.
[9] Larry C. Andrews and Ronald L. Phillips. *Laser beam propagation through random media*, volume 2. SPIE, 2005.
[10] M. Toyoshima, T. Jono, K. Nakagawa, and A. Yamamoto. Optimum divergence angle of a Gaussian beam wave in the presence of random jitter in free-space laser communication systems. *J. Opt. Soc. Am. A.*, 19(3):567–571, 2002.
[11] Kamran Kiasaleh. On the probability density function of signal intensity in free-space optical communications systems impaired by pointing jitter and turbulence. *Optical Engineering*, 33(11):3748–3757, 1994.
[12] Fan Yang, Julian Cheng, and Theodoros A. Tsiftsis. Free-space optical communication with nonzero boresight pointing errors. *IEEE Transactions on Communications*, 62(2):713–725, 2014.
[13] L C Andrews, R L Phillips, and P T Yu. Optical scintillations and fade statistics for a satellite-communication system. *Appl. Opt.*, 34:7742–7751, 1995.
[14] Larry C. Andrews. Analysis of beam wander effects for a horizontal-path propagating Gaussian-beam wave: focused beam case. *Optical Engineering*, 46(8):086002, 8 2007.
[15] Larry C. Andrews. *Field Guide to Atmospheric Optics*, volume FG41. SPIE, Bellingham, 2 edition, 2019.
[16] Larry C Andrews. Beam Wander and the Scintillation Index. In *OSA Optical Sensors and Sensing Congress*, 2020.
[17] Nikolaos K. Lyras, Charilaos I. Kourogiorgas, Athanasios D. Panagopoulos, Konstantinos P. Liolis, and Zoran Sodnik. Long Term Irradiance Statistics for Optical GEO Satellite Feeder Links: Validation Against Experimental Data. *Wireless Personal Communications*, 114(1):749–764, 9 2020.
[18] L C Andrews, W B Miller, and J C Ricklin. Geometrical representation of Gaussian beams propagating through complex paraxial optical systems. *Appl. Opt*, 32:5918–5929, 1993.
[19] Dirk Giggenbach, Christian Fuchs, Amita Shrestha, Karen Saucke, and Florian Moll. Reference Power Vectors for the Optical LEO Downlink Channel. In *2019 IEEE International Conference on Space Optical Systems and Applications (ICSOS)*, pages 1–4, 2019.
[20] Dirk Giggenbach. Fading-loss assessment in atmospheric free-space optical communication links with on-off keying. *Optical Engineering*, 47(4):046001, 4 2008.
[21] Isaac I Kim, Ron Stieger, Joseph A Koontz, Carter Moursund, Micah Barclay, Prasanna Adhikari, John Schuster, Eric Korevaar, Richard Ruigrok, and Casimer Decusatis. Wireless optical transmission of fast ethernet, FDDI, ATM, and ESCON protocol data using the TerraLink laser communication system. *Optical Engineering*, 37(12):3143–3155, 1998.
[22] A. Montmerle-Bonnefois, C. Petit, C. B. Lim, J. F. Sauvage, S. Meimon, P. Perrault, F. Mendez, B. Fleury, J. Montri, J. M. Conan, V. Michau, N. Védrenne, Z. Sodnik, and C. Voland. Adaptive optics precompensation of a GEO feeder link: The FEEDELIO experiment. In *Optics InfoBase Conference Papers*, volume Part F149-LSC 2019. OSA - The Optical Society, 2019.
[23] Rudolf Saathof, Remco den Breeje, Wimar Klop, Niek Doelman, Thijs Moens, Michael Gruber, Tjeerd Russchenberg, Federico Pettazzi, Jet Human, Ramon Mata Calvo, Juraj Poliak, Ricardo Barrios, Matthias Richerzhagen, and Ivan Ferrario. Pre-correction adaptive optics performance for a 10 km laser link. In *Proc. SPIE 10910, Free-Space Laser Communications XXXI*, page 53. SPIE-Intl Soc Optical Eng, 3 2019.
[24] J M Martin and Stanley M Flatté. Simulation of point-source scintillation through three-dimensional random media. *J. Opt. Soc. Am. A*, 7(5):838–847, 1990.
[25] Stanley M Flatté, Charles Bracher, and Guang-Yu Wang. Probability-density functions of irradiance for waves in atmospheric turbulence calculated by numerical simulation. *J. Opt. Soc. Am. A*, 11(7):2080–2092, 1994.
[26] Reginald J Hill and Rod G Frehlich. Probability distribution of irradiance for the onset of strong scintillation. *J. Opt. Soc. Am. A.*, 14(7):1530–1540, 1997.
[27] Stanley M Flatté and James S Gerber. Irradiance-variance behavior by numerical simulation for plane-wave and spherical-wave optical propagation through strong turbulence. *J. Opt. Soc. Am. A.*, 17(6):1092–1097, 2000.
[28] M. A. Al-Habash. Mathematical model for the irradiance probability density function of a laser beam propagating through turbulent media. *Optical Engineering*, 40(8):1554–1562, 8 2001.

[29] Gracheva M. E. and Gurvich A. S. Strong fluctuations in the intensity of light propagated through the atmosphere close to the earth. *Izvestiya VUZ. Radiofizika*, 8(4):717–724, 1965.

[30] James R Dunphy and J Richard Kerr. Scintillation measurements for large integrated-path turbulence. *J. Opt. Soc. Am. A.*, 63(8):981–986, 1973.

[31] J Richard Kerr and James R Dunphy. Experimental effects of finite transmitter apertures on scintillations. *J. Opt. Soc. Am. A.*, 63(1):1–8, 1973.

[32] M E Gracheva, A S Gurvich, S S Kashkarov, and V V Pokasov. Similarity relations for strong fluctuations of the intensity of light propagating in a turbulent medium. *Zhurnal Eksperimentalnoi i Teoreticheskoi Fizik*, 40(6):1011–1016, 1974.

[33] G. Parry. Measurement of atmospheric turbulence induced intensity fluctuations in a laser beam. *Optica Acta*, 28(5):715–728, 1981.

[34] W A Coles and R G Frehlich. Simultaneous measurements of angular scattering and intensity scintillation in the atmosphere. *J. Opt. Soc. Am. A.*, 72(8):1042–1048, 1982.

[35] J M Martin and Stanley M Flatté. Intensity images and statistics from numerical simulation of wave propagation in 3-D random media. *Appl. Opt.*, 27:2111–2126, 1988.

[36] Anna Consortini, E Cochetti, James H Churnside, and Reginald J Hill. Inner-scale effect on irradiance variance measured for weak-to-strong atmospheric scintillation. *J. Opt. Soc. Am. A*, 10(11):2354–2362, 1993.

[37] Shivan M. Augustine and Naven Chetty. Experimental verification of the turbulent effects on laser beam propagation in space. *Atmosfera*, 27(4):385–401, 2014.

[38] Janusz Kwiecień. The effects of atmospheric turbulence on laser beam propagation in a closed space—An analytic and experimental approach. *Optics Communications*, 433:200–208, 2 2019.

[39] Alexander Knoedler and Florian Moll. Atmospheric Turbulence Statistics and Profile Modeling. Local to DLR Oberpfaffenhofen. In *COAT-2019 - workshop (Communications and Observations through Atmospheric Turbulence: characterization and mitigation)*, 2019.

[40] Sven A. van Binsbergen, Peter J. van den Berg, Loes C. W. Scheers, Jari Blom, Erik Sucher, Alexander M. J. van Eijk, and Karin Stein. Laser propagation measurements over a multi-km path in a maritime environment. In Karin Stein and Szymon Gladysz, editors, *Environmental Effects on Light Propagation and Adaptive Systems V*, page 2. SPIE, 10 2022.

[41] Gary J. Baker and Robert S. Benson. Gaussian beam scintillation on ground-to-space paths: the importance of beam wander. In *Free-Space Laser Communications IV*, volume 5550, pages 225–236. SPIE, 10 2004.

[42] Federico Dios, Juan Antonio Rubio, Alejandro Rodríguez, and Adolfo Comeró. Scintillation and beam-wander analysis in an optical ground station-satellite uplink. *Appl. Opt.*, 43:3866–3873, 2004.

[43] Ronald L. Phillips. Strehl ratio and scintillation theory for uplink Gaussian-beam waves: beam wander effects. *Optical Engineering*, 45(7):076001, 7 2006.

[44] R.J. Sasiela. *Electromagnetic Wave Propagation in Turbulence*. Springer-Verlag, Berlin, 1st edition, 1994.

[45] Kristiaan Broekens, Wimar Klop, Thijs Moens, Martin Eschen, Gustavo Castro Do Amaral, Fabrizio Silverstri, Aleid Oosterwijk, Martijn Visser, Niek Doelman, Lauren Kaffa, Rudolf Saathof, and Ivan Ferrario. Adaptive Optics pre-correction Demonstrator for Terabit Optical Communication. 2022.

[46] D. Sprung, P. Grossmann, E. Sucher, K. Weiss-Wrana, and K. Stein. Stability and height dependant variations of the structure function parameters in the lower atmospheric boundary layer investigated from measurements of the long-term experiment VERTURM (vertical turbulence measurements). In *Optics in Atmospheric Propagation and Adaptive Systems XIV*, 2011.

[47] A.E. Siegman. How to (Maybe) Measure Laser Beam Quality. *OSA Trends in Optics and Photonics*, 17, 1998.

[48] Larry B. Stotts and Larry C. Andrews. Adaptive optics model characterizing turbulence mitigation for free space optical communications link budgets. *Optics Express*, 29(13), 6 2021.

[49] Florian Moll. Experimental characterization of intensity scintillation in the LEO downlink. In *2015 4th International Workshop on Optical Wireless Communications, IWOW 2015*, pages 31–35. Institute of Electrical and Electronics Engineers Inc., 11 2015.

[50] Frederic M. Davidson. Measurements of intensity scintillations and probability density functions of retroreflected broadband 980-nm laser light in atmospheric turbulence. *Optical Engineering*, 43(11):2689–2695, 11 2004.

[51] A. Kamp. *Space Instrumentation Engineering*. Delft University of Technology, Delft, 1st edition, 11 2007.

APPENDIX A
LITERATURE STUDY

To understand the theory behind the research and to accurately find gaps in the body of research, which contribute to the progress in the field of laser satellite communications at the same time, a literature study has been performed. The results of this literature study, which contribute to the general message of this thesis, are presented in this appendix, together with more background information explaining the material. This is an addition to section II. How the atmosphere is generally modelled is presented in subsection A-A. Secondly, the an overview of the current empirical research performed is presented in subsection A-B, after which the gap in the body of science is marked in subsection A-C. To fill this gap research questions and a research objective to be used are posed in subsection A-D.

A. Atmospheric Turbulence Model

Atmospheric turbulence influences the path light rays take. The differences in refraction indices in the atmosphere as a result of turbulence make it that light rays passing through turbulence do not follow a straight path, see Figure 24. Over long distances these effects can enlarge, leading to spatial incoherence of the wavefront. Researchers try to quantify the effects of atmospheric turbulence on a laser beam by splitting up the effects and quantify each separately, with limited success [41], [42].

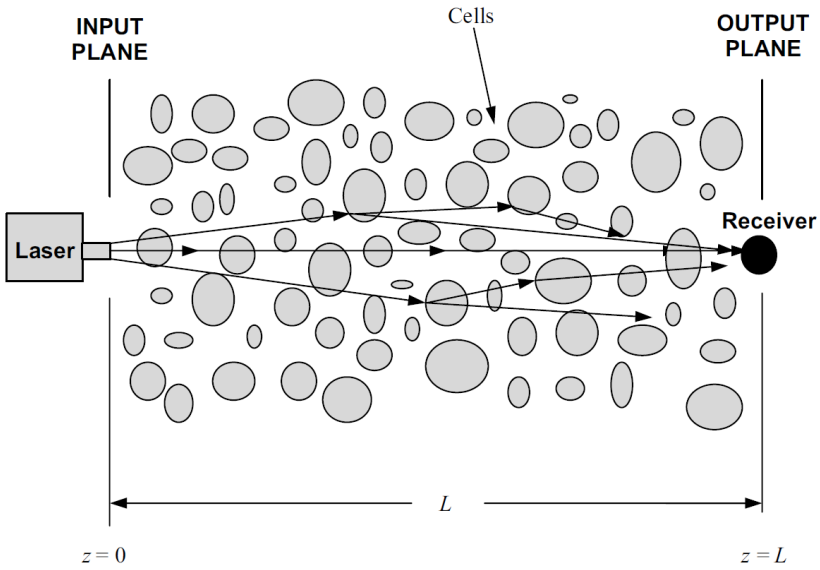

Fig. 24: Propagation geometry for an extended medium [9].

To describe optical propagation through a turbulent atmosphere, the atmospheric turbulence must be modelled. The applicable equation used for this is the Hufnagel-Valley model [13]. This modified Hufnagel-Valley model is defined as follows:

$$C_n^2 = 0.00594 \cdot \left(\frac{v}{27}\right)^2 \cdot \left(10^{-5}h\right)^{10} \cdot e^{-\frac{h}{1000}} + 2.7 \cdot 10^{-16} \cdot e^{-\frac{h}{1500}} + A \cdot e^{-\frac{h}{100}}, \tag{40}$$

where $C_n^2[m^{-2/3}]$ is the refractive index structure parameter, v $[m/s]$ the pseudowind, h $[m]$ the altitude above sea level, A $[m^{-2/3}]$ a nominal value of C_n^2 at the ground (or $C_n^2(0)$) and h_{OGS} $[m]$ the height above sea level of the optical ground station (OGS).

The refractive index structure parameter computed by above stated model, is an important parameter, which important relations use to quantify the effect of turbulence on a laser beam. The Hufnagel-Valley model gives a simple expression for the turbulence intensity, but it is still an approximation, as can be seen in Figure 25. It compares the model to turbulence intensities measured in Korea. The model approximates the refractive index structure parameter, but can differ significantly as well (3E-16 vs. 7E-17 for the HV-model and test data, respectively).

The theoretical models on the optical propagation through this turbulent atmosphere are presented in section II. The implementation of all those equations have been verified by recreating the figures in their respective papers.

B. Verification & Validation of Theory

Past research concerning verification and validation has been gathered, to understand to what extend the theory presented in section II and subsection A-A has been scrutinized. This search shows that the verification is done using Monte Carlo simulations [14], [16], [24]–[28]. All these verification studies focus on weak turbulence conditions, except [26], which focuses on the

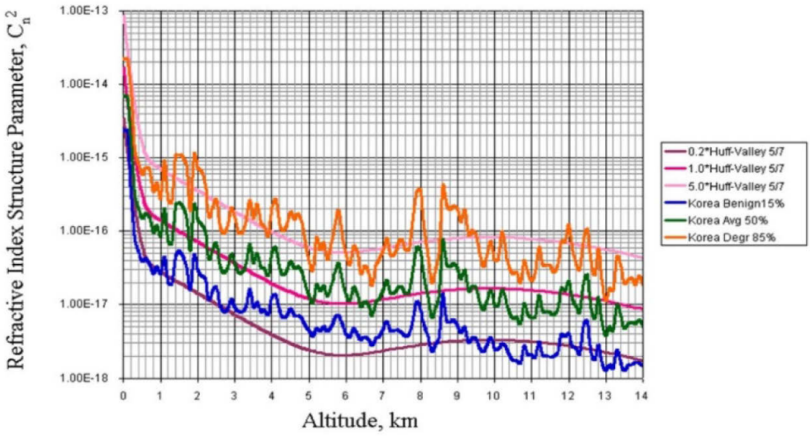

Fig. 25: Hufnagel-Valley 5/7 model compared to turbulence measured in Korea [48].

regime close to strong scintillation. Furthermore, the research focuses on irradiance and scintillation only, except for [16], which also verifies scintillation including the contribution of beam wander.

Next to simulations, several ground-to-ground (G2G) tests have been performed to check the theory [29]–[40]. One of these tries to replicate turbulence in a small-scale lab [37], others use a controlled environment, such as a large closed space [38] and some use a link in free space ranging from 375 m [39] to 8.5 km [32]. However, most tests are in the 1 km range [29], [31], [33]–[36]. The validation focuses on scintillation and irradiance fluctuations. Beam wander is mentioned as a contributor in some of these tests, but omitted in the analysis. In [40] the beam wander and spot size is retrieved for a multi-km path, but this is a feasibility study, which does not focus on verification of turbulence models under varying turbulence conditions.

Next to this, only one test been found that uses a space-to-ground (S2G) link [49]. This paper focuses on the scintillation and mean irradiance versus elevation angle of the satellite. With the problem description introduced in section I, it is therefore of less interest.

C. Gap in Research

The literature presented in section II and subsection A-B show the dependability on the Rytov approximation; that is, most equations are only valid for weak turbulence conditions. Furthermore, theory deviates from simulation results even under weak turbulence conditions for longer propagation distances (>6 km) [14].

Next to this, the validation in papers presented in subsection A-B does not focus on beam wander and scintillation. Only scintillation or mean irradiance is analyzed. Therefore, an important part of the theory presented in section II is not checked by means of validation, especially for longer link paths. A reason for this is that systems, which can deliver a laser spot accurately over long distances were not available. These systems are now available [8], [22], [23].

As discrepancies still have been found for the beam wander and scintillation effects, it is therefore interesting to understand where these lie. Furthermore, it is unknown if splitting up a link in smaller parts aids in the accuracy of the theory. The current theory for scintillation and beam wander are only empirically validated for short distances [37], [50]. Empirical validation of the theory will aid in understanding the accuracy of the models and help improve the models used for future system designs.

D. Research Questions & Objective

To focus the research and aid in setting up a plan of attack, research questions and a research objective have been formulated. Based on the literature study, the research questions are given in subsubsection A-D1. The research objective is stated in subsubsection A-D2.

1) Research Question(s): The literature study of gave rise to an understanding of the gap in the current body of knowledge. Together with the applicable findings by TNO presented in section I and subsection A-C research questions have been identified. Answering the research questions will lead to a better understanding in optical propagation through a turbulence atmosphere and fill the identified research gap. In the light of optical propagation through atmospheric turbulence, the first of the research questions to be answered is:

”How can beam wander and on-axis scintillation effects be separated from empirical data for analysis?”

The follow-up question is related to the analysis of the individual components having influence on optical propagation:

”How do theoretical results regarding, on-axis scintillation, beam wander and beam spread compare to empirical results?”

The final research question focuses on the impact of AO systems, which need is stated in section I. This research questions is as follows:

"How does the predicted impact of Adaptive Optics for beam wander and (on-axis) scintillation compare to empirical results?"

2) Research Objective: Using TNO's need statement from section I and the literature review (subsection A-C), the main research objective of this thesis is stated as:

"To achieve empirical validation of theoretical models used for optical propagation through atmospheric turbulence by comparing the impact of atmospheric turbulence on a ground to ground laser link to the outcomes of those relations".

Notice that by answering the research questions presented in subsubsection A-D1, the research objective will be met.

APPENDIX B
ANSWERS TO RESEARCH QUESTIONS

Below are short answers of the research questions in which the information of the report specific to answering these questions is gathered. Next to this, the parts where additional information on answering the research questions is indicated, as well.

A. First Research Question

The first research question is:

"How can beam wander and on-axis scintillation effects be separated from empirical data for analysis?"

As shown in the methodology (section III, section D), the spot size and location can be retrieved from the data retrieved in the field test using the Ground Terminal Breadbaord and Beam Profiler. Using simple equations - center of gravity of intensity (Equation 37) and second-moment width Equation 38) -, aided by a lookup table. The on-axis scintillation is a fixed point in the imaged plane and thus can be retrieved independently of the spot location. Next to this, by using the spot location, also the longitudinal and radial scintillation indices can be retrieved.

There are several factors limiting the accuracy of the data analysis: the obscuration and clipping, limited amount of Turbulence Monitors along the path and the measurement time. The obscuration and clipping lead to a loss of information. This has been bypassed by the lookup table, but it can never reproduce the data or be fully accurate. Furthermore, not all measurements were included in the test. As generally the beam for tip/tilt pre-corrected measurements starts breaking up at a C_n^2 of 5E-15 $m^{-2/3}$, measurements for stronger turbulence conditions are omitted.

Concluding, by retrieving the spot location for each frame, the beam wander can be analyzed, while the on-axis scintillation can be retrieved by analyzing a fixed point in the imaged plane.

B. Second Research Question

"How do theoretical results regarding, on-axis scintillation, beam wander and beam spread compare to empirical results?"

The empirical results match theoretical results closely for weak turbulence conditions, see section IV. The deviation between empirical and theoretical results grow for increasing turbulence strengths outside the weak turbulence regime. Furthermore, the instantaneous spot size does not change significantly for the changing turbulence conditions: It stays similar to the free-space spot size for the turbulence conditions analyzed in this research. Next to this, the beam wander can be reduced significantly with tip/tilt pre-correction below the theoretical beam wander for an untracked beam, as the pre-correction utilizes refractions of the beam in the atmosphere to deliver the beam to the Beam Profiler.

C. Third Research Question

"How does the predicted impact of Adaptive Optics for beam wander and (on-axis) scintillation compare to empirical results?"

As can be seen in section E, the reduction in beam wander predicted by the simulation results matches the empirical results in that it reduces, even if it is set to zero in the simulation for 28 modes. As perfect tracking is not feasible in reality, the amount of reduction deviates between simulation and field test.

Furthermore, the reduction in scintillation measured during the field test is not represented in the simulation results. The scintillation indices from the simulation tool have a very large spread, even larger than the theory on which it is based. The reason for this is currently still unknown and to be investigated.

The measured spot size does not change significantly for higher AO modes, which it does for the simulated results. The reason for this is that the spot size does not seem to be influenced by turbulence for the turbulence range analyzed in this research. Only for $C_n^2 >$ 5E-15 $m^{-2/3}$ does the spot start to increase significantly. However, due to the beam breaking up for those turbulence conditions this part is not analyzed. Thus, as turbulence does not influence the spot size for the turbulence conditions analyzed, the pre-correction can also not improve the performance. The performance is already optimal, as the spot size equals the free-space spot size.

APPENDIX C
TEST SETUP

Some more information on the test setup can help to understand how the data came to be. The required variables inherent to the ground station are noted in subsection C-A. Afterwards, the camera settings used are presented in subsection C-B. Lastly, further explanation of the test proceedings is given in subsection C-C.

A. Ground Station

The ground station is a mobile trailer containing an optical system. This optical system is described in [45]. Some values are used as an input for the equations presented in section II and are therefore gathered here for completeness, see Table III.

TABLE III: Ground station variables used for the models presented in section II

Variable	**Value**
W_0	0.0308 m
F_0	$3.95 \cdot 10^3$ m

B. Imager

The camera settings of the Beam profiler used are shown in Table IV.

TABLE IV: Camera settings used during the field test.

Variable	**Value**
Shutter time	5E-6 s
Frame rate	800 Hz
Quantum efficiency	0.70
Full Well Capacity	65E3
Number of bits	12
Image size	512x512 pixels

The data has been logged in vectors containing a the time stamp and 12 bit image. This image is reshaped to a vector in order to save it. The time stamp is linked for the Beam Profiler and ground station via satellite.

C. Test Proceedings

During the test the ground station switches between different AO modes (8, 16, 28 and 40). In between every switch, first a dataset is logged with only tip/tilt pre-correction. This is done to see the influence of the higher AO modes, when they are activated. The reason the tip/tilt pre-correction stays on is to keep the laser within the receiver's field of view. For a higher number of AO modes, the order of the functions used for control of the deformable mirror in the AO system increases.

In total 3885 measurements were recorded, but rain resulted in some measurements failing to meet the requirements for analysis, see Figure 26. As can be seen vertical stripes have appeared in the image, which are attributed to rain drops falling through the laser bundle or dripping down the glass window in front of the Beam Profiler. In total 1656 two-second measurements have been used in the analysis.

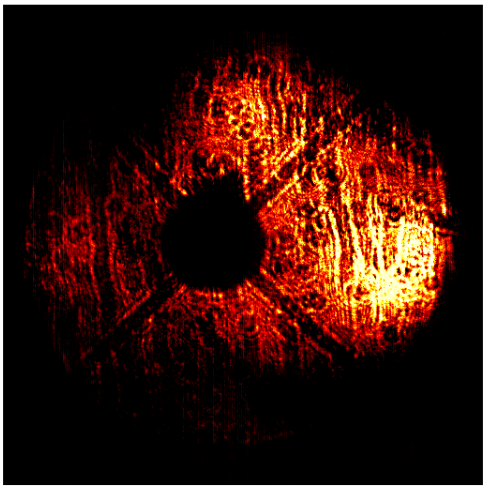

Fig. 26: Light received at the Beam Profiler at the end of a rain shower.

APPENDIX D
DATA ANALYSIS

A. Turbulence Monitor Selection

As shown in Figure 6 four turbulence monitors are positioned along the link path. The mast of the Gerbrandy tower influences the turbulence conditions of the two turbulence monitors on the tower (TM 1 and TM 4). TM 1 was positioned on the Western side of the tower and TM 4 on the Southern side.

To select the correct turbulence monitor, the wind direction of TM 3 is used to roughly indicate the wind direction at the tower. The data is then used from the turbulence monitor which lies on that side of the mast, from which the wind at TM 3 is blowing. For wind direction angles between 45° and 225° the data of TM 4 is used (0° pointing North, clockwise positive). For all other angles TM 1 is used. For angles equal to 45° or 225°, the average results of TM 1 and TM 4 is used. An example of the turbulence monitor selection is shown in Figure 27.

B. Correcting Logged Data

During a measurement, the test data was saved in a buffer on the test computer. This buffer is then emptied after a measurement has finished. However, the buffer was too small to contain a full measurement of 30 seconds. The buffer could only contain data of ∼2 seconds. Furthermore, the buffer spread the results of a measurement over 2 files. This way one file contained half the result of two subsequent measurements. Before the data was analyzed all data sets were put in their own correct file. Which data should be in which AO mode file has been retrieved by looking at patterns in received power and average intensity over a measurement. The AO sequence was 2-8-2-16-2-28-2-40-2. Thus, two consecutive measurements with tip/tilt pre-correction only follow between two of these sweeps. A clear indication of these two equal control settings was found and used to put the correct data with the correct AO setting.

C. Imperfections in Data

Several imperfections can be found in the optical system. An overview of this has been made and is shown in Figure 28. The influence most imperfections cannot be mitigated in the data analysis within a reasonable time scope and are therefore accepted. The defocus can also not be mitigated, but the change in path length can.

The size of the spider struts in the image with respect to their real size is used to compute the focal distance, see Equation 41 [51]:

$$\begin{aligned} z &= \frac{dW}{2\lambda} \\ &= \frac{3.9 \cdot 10^{-2} \cdot 3.0 \cdot 10^{-3}}{2 \cdot 1.550 \cdot 10^{-6}} \\ &= 38\ m, \end{aligned} \tag{41}$$

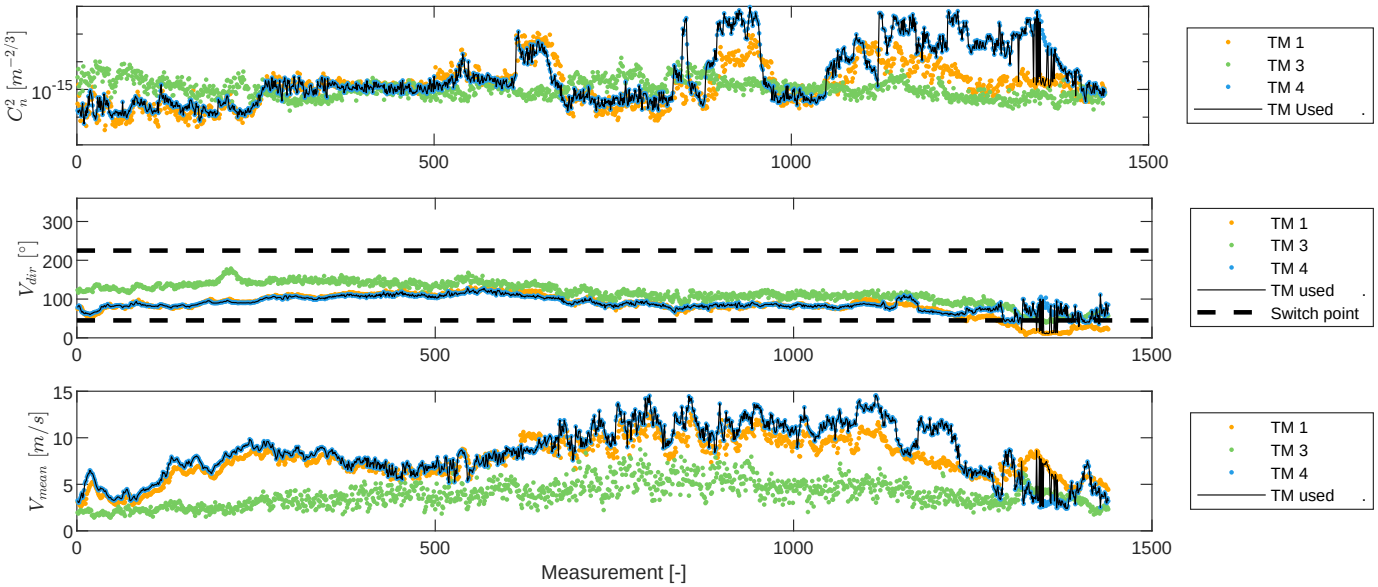

Fig. 27: C_n^2, wind direction and wind speed over time for TM 1, TM 3 and TM 4 to select the TM being used.

where z $[m]$ is the distance of the slit to the receiver, d $[m]$ the width of the central band in the diffraction pattern, W $[m]$ the actual width of the object and λ $[m]$ the wavelength. The total path length of the light from the spider strut to the image is measured to be 2.16 m and thus the defocus equals 36 m. This defocus is subtracted from the path length for the theory to make sure both theory and test results cover the same distance.

Next to the static imperfections a dynamic imperfection was seen on videos of the test results. This is the results of angle of arrival fluctuations induced by the atmospheric turbulence. A ray trace analysis has been performed in which this theory is checked. The setup of the ray trace analysis is shown in Figure 29.

Point 1 is placed at 25 cm from the optical axis at 1 m in front of M2. Point 2 is placed at M1 at 15 cm from the optical axis. Point 3 is placed on M2 at 2 cm from the optical axis of M2 and point 4 is placed 1 cm in front of L1 at 0.2 cm from the optical axis.

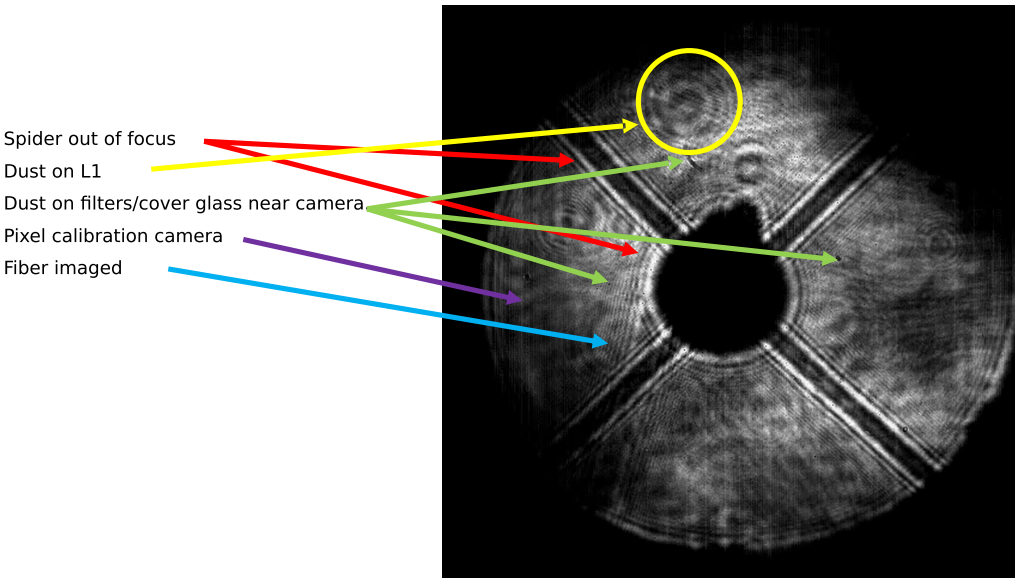

Fig. 28: Imperfections in optical system.

The analysis has been performed via ray transfer matrix analysis (ABCD), using the following components:

$$\begin{pmatrix} 1 & d \\ 0 & 1 \end{pmatrix} \text{(Free-space propagation)}, \tag{42}$$

$$\begin{pmatrix} 1 & 0 \\ \frac{-2}{R} & 1 \end{pmatrix} \text{(M1)}, \tag{43}$$

$$\begin{pmatrix} 1 & 0 \\ 0 & 1 \end{pmatrix} \text{(M2)}, \tag{44}$$

$$\begin{pmatrix} 1 & 0 \\ \frac{-1}{f} & 1 \end{pmatrix} \text{(L1)}, \tag{45}$$

where R $[m]$ is the radius of curvature of the M1 mirror and f $[m]$ the focal distance of the lens.

In the ray trace analysis the location of the Beam Profiler is moved by 3 cm, which equals a rotation of 0.007°at 226 m altitude. The shift in detected location for point 1-4 on the imager plane are 2.6E-4 mm, 5.23E-3 mm, 5.3E-3 mm and 5.3E-3 mm. The shift of point 3 and 4 is less. This is also seen in the videos of the test data. Thus the angle of arrival fluctuations cause the vibrations in the videos. These vibrations are not omitted as it is outside of the scope of this research.

D. Pixel Value Conversion

The pixel values are converted to intensity using a method used by TNO:

$$\begin{aligned} G_I &= \frac{G_D E}{t_S T \eta_Q} \\ &= \frac{16 \cdot 1.3 \cdot 10^{-19}}{5.0 \cdot 10^{-6} \cdot 6.0 \cdot 10^{-4} \cdot 0.70} \\ &= 9.7 \cdot 10^{-10}\ W/(m^2 \cdot pixel\ count), \end{aligned} \tag{46}$$

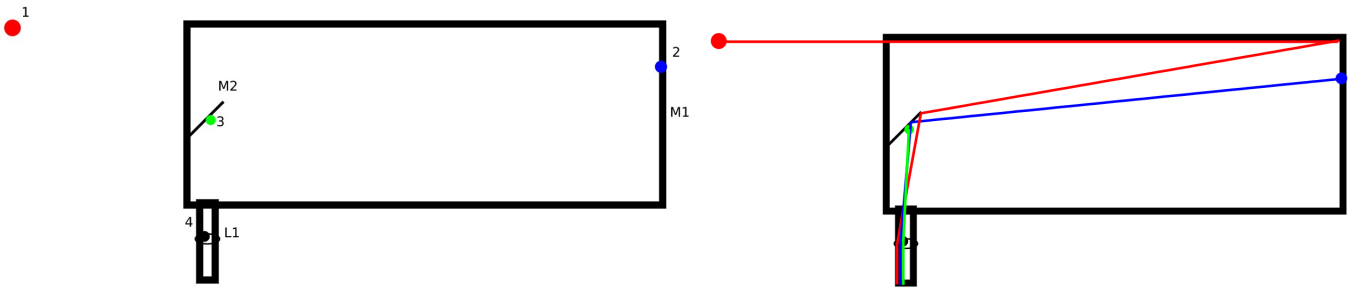

(a) Positions of points and components used.

(b) Rays analyzed in the ray trace analysis.

Fig. 29: Schematic representation of the ray trace analysis performed.

where G_I $[W/(m^2 \cdot pixel\ count)]$ is the imager gain, E $[J]$ the photon energy, t_S $[s]$ the shutter time, T $[-]$ the transmission of the Beam Profiler and η_Q $[-]$ the quantum efficiency and G_D $[-]$ the detector gain, which is computed by Equation 47:

$$\begin{aligned} G_D &= \frac{FW}{2^n} \\ &= \frac{65 \cdot 10^3}{2^1 2} \\ &= 16, \end{aligned} \tag{47}$$

where FW $[-]$ is the Full Well Capacity of the detector and n $[-]$ the number of bits (12). Furthermore, the photon energy is computed with Equation 48:

$$\begin{aligned} E &= \frac{hc}{\lambda} \\ &= \frac{6.6261 \cdot 10^{-34} \cdot 2.99792458 \cdot 10^8}{1.5500 \cdot 10^{-6}} \\ &= 1.3 \cdot 10^{-19}\ J, \end{aligned} \tag{48}$$

where h $[m^2 kg/s]$ is the Planck constant and c $[m/s]$ the speed of light..

E. Spot size Derivation

In the data analysis, the second-moment width is computed, see Equation 38. However, the equations in section II use the $1/e^2$-radius 'w'. A conversion must be made between these values. The derivation is shown below, which starts at the second-moment equation, repeated here below, for ease of reading.

$$D4\sigma_x = 4\sigma = 4\sqrt{\frac{\int_{-\infty}^{\infty}\int_{-\infty}^{\infty} I(x,y)(x-\bar{x})^2 dxdy}{\int_{-\infty}^{\infty}\int_{-\infty}^{\infty} I(x,y)dxdy}}$$

By substituting the intensity equation for a Gaussian beam and integrating, a conversion can be made between $D4\sigma$ and w. Substituting the intensity equation for a Gaussian beam leads to Equation 49:

$$D4\sigma = 4\sigma = 4\sqrt{\frac{\int_0^{2\pi}\int_0^{\infty} I_0 \left(\frac{w_0}{w}\right)^2 e^{-\frac{2r^2}{w^2}} (r)^2 r dr d\theta}{\int_0^{2\pi}\int_0^{\infty} I_0 \left(\frac{w_0}{w}\right)^2 e^{-\frac{2r^2}{w^2}} r dr d\theta}}, \tag{49}$$

where an extra r is added as the Cartesian coordinate system has been changed to a polar coordinate system. Furthermore, $\bar{r}$ is omitted as it is equal to zero, as the centroid lies at the center of the spot. Integrating the inner integral of the numerator is shown below:

$$\int_0^{\infty} I_0 \left(\frac{w_0}{w}\right)^2 e^{-\frac{2r^2}{w^2}} (r)^2 r dr = I_0 \left(\frac{w_0}{w}\right)^2 \int_0^{\infty} e^{-\frac{2r^2}{w^2}} r^3 dr.$$

Substituting $u = r^2 \rightarrow du = 2rdr$ and omitting the constants from the equation for now, leads to:

$$\int e^{-\frac{2r^2}{w^2}} r^3 dr = \frac{1}{2}\int u e^{-\frac{2u}{w^2}} du.$$

Using another substitution of $v = -u/w \rightarrow dv = -1/w^2 du$ and again omitting the constant from the equation, leads to:

$$\int u e^{-\frac{2u}{w^2}} du = w^4 \int v e^{2v} dv.$$

The last part can be integrated by parts with $f = v, f' = 1$ and $g' = e^{2v}, g = e^{2v}/2$:

$$\int ve^{2v}dv = \frac{ve^{2v}}{2} - \int \frac{e^{2v}}{2}dv = \frac{ve^{2v}}{2} - \frac{e^{2v}}{4}.$$

Substituting the solved integrals and solving the outer integral (2π), leads to:

$$\left[\frac{-\pi I_0 w_0^2 r^2 e^{-\frac{2r^2}{w^2}}}{2} - \frac{-\pi I_0 w_0^2 w^2 e^{-\frac{2r^2}{w^2}}}{4}\right]_{r=0}^{r=\infty} = \left[-\frac{-\pi I_0 w_0^2 \cdot \left(2r^2 + w^2\right) e^{-\frac{2r^2}{w^2}}}{4}\right]_{r=0}^{r=\infty} = \frac{\pi I_0 w^2 w_0^2}{4} \tag{50}$$

Solving the denominator follows the same approach, but with r instead of r^3:

$$\int_0^\infty I_0 \left(\frac{w_0}{w}\right)^2 e^{-\frac{2r^2}{w^2}} r dr = I_0 \left(\frac{w_0}{w}\right)^2 \int_0^\infty e^{-\frac{2r^2}{w^2}} r dr.$$

Substituting $u = -2r^2/w^2 \rightarrow du = -4r/w^2 dr$ leads to:

$$\int e^{-\frac{2r^2}{w^2}} r dr = \int e^u du = e^u$$

Substituting the solved integral and solving the outer integral (2π), leads to:

$$I_0 \left(\frac{w_0}{w}\right)^2 \int_0^\infty e^{-\frac{2r^2}{w^2}} r dr = \left[\frac{-\pi I_0 w_0^2 r^2 e^{-\frac{2r^2}{w^2}}}{2}\right]_{r=0}^{r=\infty} = \frac{\pi I_0 w_0^2}{2}. \tag{51}$$

Next, Equation 50 and Equation 51 can be substituted in Equation 49 and solved for w, see Equation 52:

$$\begin{aligned} D4\sigma &= 4\sqrt{\frac{\int_0^{2\pi}\int_0^\infty I_0 \left(\frac{w_0}{w}\right)^2 e^{-\frac{2r^2}{w^2}} (r)^2 r dr d\theta}{\int_0^{2\pi}\int_0^\infty I_0 \left(\frac{w_0}{w}\right)^2 e^{-\frac{2r^2}{w^2}} r dr d\theta}} \\ &= 4\sqrt{\frac{\frac{\pi I_0 w^2 w_0^2}{4}}{\frac{\pi I_0 w_0^2}{2}}} \\ &= 4\sqrt{\frac{w^2}{2}}. \end{aligned} \tag{52}$$

Lastly, solving for w leads to Equation 53:

$$w = \frac{\sqrt{2} D4\sigma}{4} \tag{53}$$

F. Lookup Table

Videos, wherein the results of Equation 37 were shown, indicate an inaccuracy of the method, as it does not take obscured or clipped parts of the spot into account. Furthermore, the spot size also deviates as it is computed with the center are the spot location, see Equation 38. Figure 30 is a still frame showing this deviation. The spot center clearly lies more to the top left, perhaps even outside the aperture or even the 512x512 image.

As stated in section III a lookup table is created to correctly estimate the spot location and size. How it is created is shown in subsubsection D-F1. The verification is shown in subsubsection D-F2.

1) LUT Creation: The lookup table is created using the intensity distribution, see Equation 54:

$$I(r, z) = I_0 \left(\frac{w_0}{w(z)}\right)^2 e^{-\frac{2r^2}{w(z)^2}}. \tag{54}$$

A Gaussian spot is imaged on an image size 1.5x as large, as used in the test, to allow for spot locations outside the image used in the test. Furthermore, Gaussian spots can be plotted with Equation 54, if w and w_0 are changed to an elliptical pattern, see Equation 55 andEquation 56:

$$w = \frac{w_x w_y}{\sqrt{w_x^2 sin(\theta)^2 + w_y^2 cos(\theta)^2}}, \tag{55}$$

$$w_0 = \frac{w_{0,x} w_{0,y}}{\sqrt{w_{0,x}^2 sin(\theta)^2 + w_{0,y}^2 cos(\theta)^2}}, \tag{56}$$

where

$$w_{0,x} = \frac{w_x}{\sqrt{w_y^2 + w_x^2}} w_0, \tag{57}$$

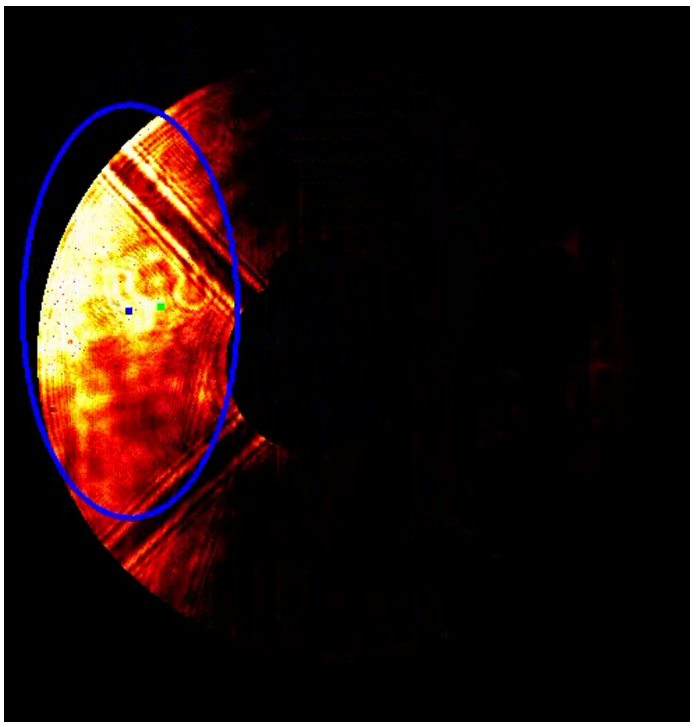

Fig. 30: Still frame showing inaccurately computed C.o.G. location (blue dot) and spot size (blue ellipse). The green dot is the average computed spot location location over the measurement.

where θ $[rad]$ is the angle along the ellipse, $w_{0,x}$ $[m]$ the horizontal waist radius and $w_{0,y}$ $[m]$ the vertical waist radius, computed analogously to Equation 57.

After the image is plotted the mask from section III is placed on top, after which the C.o.G. and $D4\sigma$ are computed. As the inputs are known and also the results after the mask has been introduced, a link is made between an unobscured and unclipped image to an obscured and clipped image. This is repeated for an array of locations on the image, with various spot sizes per location. For the inputs of this, see Table II.

A perfect Gaussian spot is used (without scintillation effects), as the effect of scintillation is a randomized process, which is influenced by wind direction and turbulence effects. These turbulence effects are influenced by many effects, including temperature and ground effects. These ground effects differ along the path due to the existence of fences, buildings and vegetation, which makes it, together with the other influences described above, deemed impossible to accurately incorporate the scintillations encountered in the test. Even more because for different turbulence conditions different scintillations occur, which would mean a different lookup table must be created for each of the 2656 measurements.

Note that the radii of the elliptical Gaussian spot are only varied in x- and y-direction and not also rotated in the image plane, even though the real spot can rotate around the boresight axis. Computing power is a limiting factor in this case, as the number of radial inputs scales the LUT size quadratically due to the image being 2D. A sensitivity analysis (subsubsection D-F2) shows that, due to the assymetrical obscuration, more spot locations in the LUT improves the performance much more than adding more spot sizes. Furthermore, interpolation between the spot sizes can be done fairly well, see subsubsection D-F2.

2) LUT Verification: To verify if the LUT fulfills its intended purpose, a method has been developed in which a spot is imaged, which is then approximated by with the LUT. Several iterations, each with increasing number of LUT entries, are compared to analyze which factors affect the LUT performance most.

The imaged spots consist of two types: a moving spot of roughly the expected spot size ($1/e^2$) at the Beam Profiler and a spot, which is fixed in its location, but changes its spot size. The moving spot has a $1/e^2$ spot radius of 16.4 cm and the changing spot varies from 9.5-21.5 cm. The moving spot furthermore moves from the left to the right of the 768x768 grid, which is equal to the LUT grid size. Lastly, the location of the spot is verified at two positions, one at the center of the image (0, 0) and one in the top left of the aperture (100, 100).

Five LUTs are used in the sensitivity analysis. The number of entries of each LUT are shown in Table V. For each LUT the number of entries in locations and spot sizes increases. As the number of entries increases, also the integration time for a LUT increases. On the available hardware LUT 1 would take up to two days to convert the test data results, while LUT 5 would take more than 500 days.

The lookup tables were assessed in a controlled environment in which a perfect Gaussian spot is imaged. The imaged spot is created with Equation 54. Afterwards, the mask used in the data analysis (section III) is placed on top. The spot location

TABLE V: Settings for lookup tables used in analysis and the optimized lookup table.

		Range	# Entries
LUT 1	**Location (x & y)**	1-768 pix	7
	Spot size	29-70 cm	3
LUT 2	**Location (x & y)**	1-768 pix	21
	Spot size	29-70 cm	8
LUT 3	**Location (x & y)**	1-768 pix	30
	Spot size	29-70 cm	12
LUT 4	**Location (x & y)**	1-768 pix	40
	Spot size	29-70 cm	16
LUT 5	**Location (x & y)**	1-768 pix	50
	Spot size	29-70 cm	21
Optimized LUT	**Location (x & y)**	1-768 pix	88
	Spot size	19-43 cm	4

and size are retrieved with Equation 37 and Equation 38, after which the lookup table is used to retrieve the actual result.

Four different situations were put to the test, see Figure 31: two in which the spot size increases, while the spot stays in the same position, and two in which a spot moves horizontally across the aperture, while the spot size is constant. The spot size is chosen to equal the average expected spot size at the receiver (32.8 cm). Note that for small spots the maximum intensity can exceed the maximum intensity, which the camera can capture ($4.16\ W/m^2$). Therefore, in the creation and analysis of the lookup tables, all values above the saturation intensity are cut off.

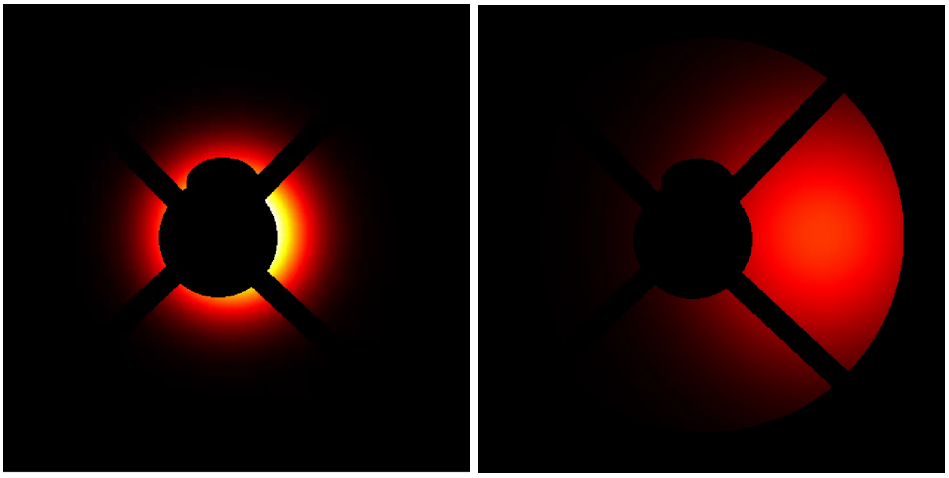

(a) Still frame of changing spot size in the image center

(b) Still frame of horizontally moving spot at $y = 0$ pix (left to right).

(c) Still frame of changing spot size at $x = y = -100$ pix.

(d) Still frame of horizontally moving spot at $y = -100$ pix (left to right).

Fig. 31: Still frames from LUT analysis with perfect Gaussian spot imaged and mask from data analysis placed on top.

Due to the importance of LUT size, the number of entries must be kept reasonably low, while maintaining accuracy. The error of the performances of the LUTs is computed for the four cases shown in Figure 31. For LUT 1 the results of the analysis

are shown in Figure 32, Figure 33, Figure 34 and Figure 35.

As can be seen, for a low amount of LUT entries, the accuracy of the LUT is worse than for the original analysis method. The LUT over-estimates the spot size and misplaces the spot. Furthermore, the spot size analysis in Figure 33 and Figure 35 shows how the original methodology under-estimates the spot size. This can be attributed to the clipping effect.

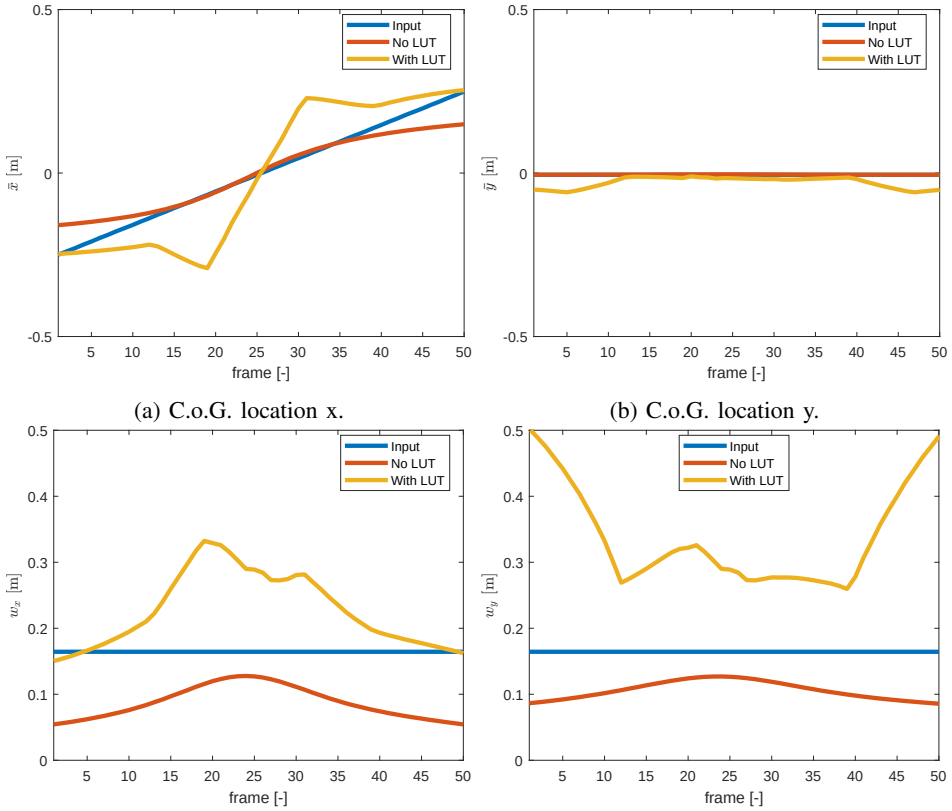

(a) C.o.G. location x.

(b) C.o.G. location y.

(c) Spot size x.

(d) Spot size y.

Fig. 32: Results of LUT 1 for a spot moving along $y = 0$ pix.

The inaccuracy of LUT 1 has lead to a study of the effect of LUT entries. This is the reason multiple lookup tables have been created with various amount of entries, see Table V.

For each of LUT 1-5, results as above have been created. These results can be analyzed together by expressing an error, see Equation 58:

$$Error = LUT\ result - Input. \tag{58}$$

This error can be plotted for each LUT as an intantaneous error, see Figure 36 and Figure 38. Lastly, the error can be plotted cumulatively, see Figure 37 and Figure 39.

The results show that the spot size and center of gravity estimation improve significatnly from LUT 1 to LUT 2. However, looking at the cumulative results of Figure 37 and Figure 39, LUT 4 and LUT 5 show a significant better performance than LUT 2 and LUT 3: $\sim$0.5 m and $\sim$0.2 m, respectively.

The difference between LUT 4 and LUT 5 is minimal. However, the computation time of both LUT varies drastically: LUT 5 would take $>$500 days to analyze the data, while LUT 4 would take $\sim$30 days. Both computation times are too long to use and therefore the lookup table must be optimized.

This optimization showed that interpolation for spot size, was fairly accurate with little inputs (4), while the amount of LUT entries for spot locations is paramount. The reasoning behind this is that the assymetrical obscuration/clipping cannot be estimated by linear interpolation, while a change in spot size can for the same locations. The optimized LUT takes around 12 days to analyze the data, as long as LUT 3.

Figure 36 and Figure 38 show that the performance of the optimized LUT is better than LUT 4 and approaches the performance of LUT 5, while being more than 40 times as fast in computation. The individual results of the optimized LUT for the cases shown in Figure 31 are presented in Figure 40, Figure 41, Figure 42 and Figure 43.. These results show the improvement of the LUT with respect to the results shown for LUT 1 (Figure 32-Figure 35). Furthermore, the LUT now outperforms the original methods. The spot size error is smaller than 0.004 m and the location error smaller than 0.002 m.

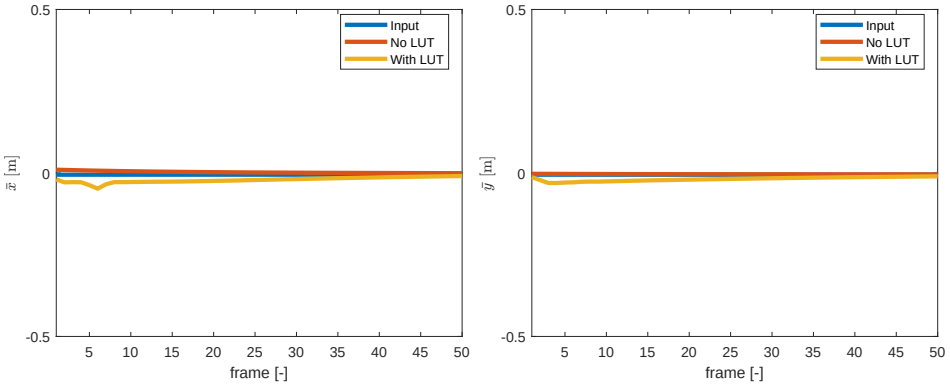

(a) C.o.G. location x.

(b) C.o.G. location y.

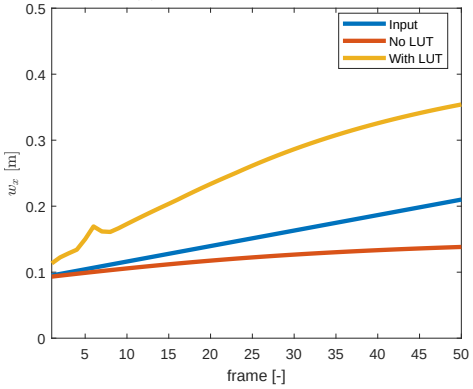

(c) Spot size x.

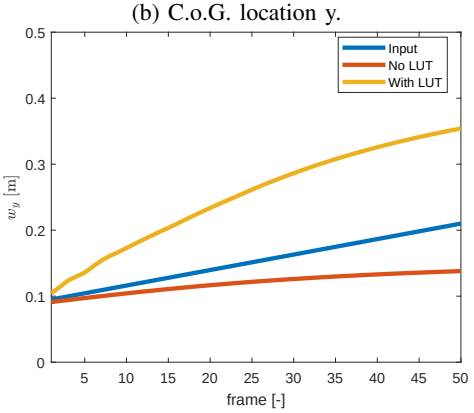

(d) Spot size y.

Fig. 33: Results of LUT 1 for a spot changing size, which is centered in the image.

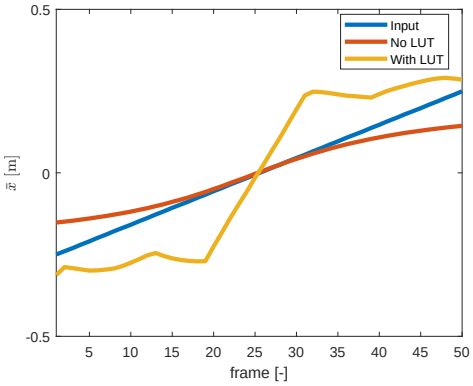

(a) C.o.G. location x.

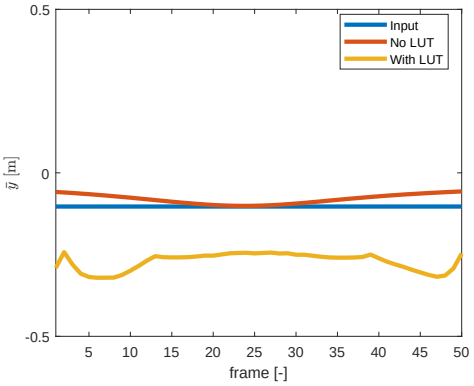

(b) C.o.G. location y.

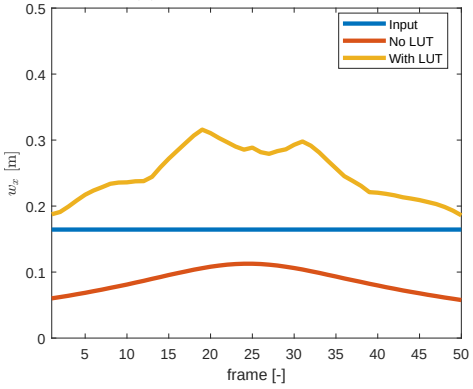

(c) Spot size x.

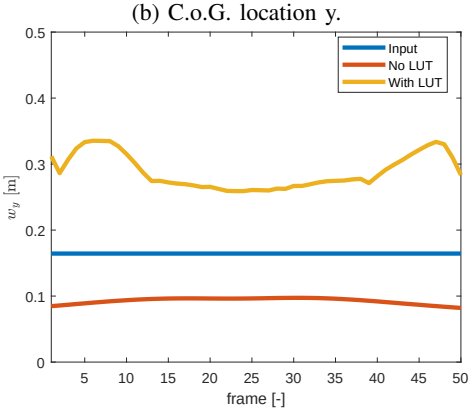

(d) Spot size y.

Fig. 34: Results of LUT 1 for a spot moving along $y = -100$ pix.

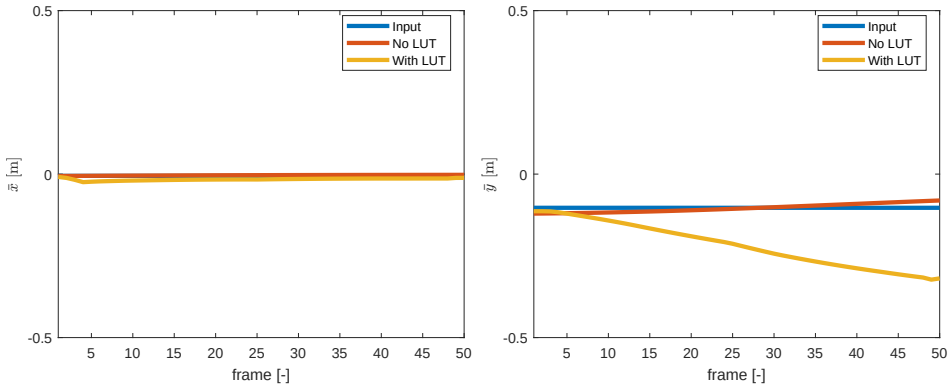

(a) C.o.G. location x.

(b) C.o.G. location y.

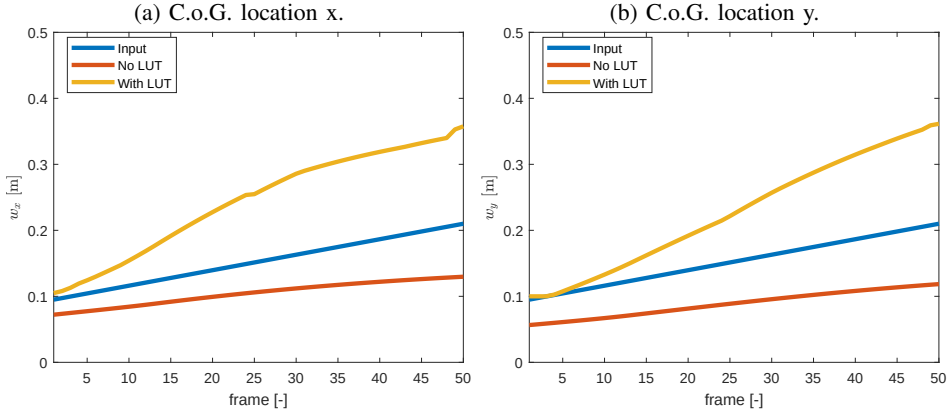

(c) Spot size x.

(d) Spot size y.

Fig. 35: Results of LUT 1 for a spot changing size, which is offset in the image.

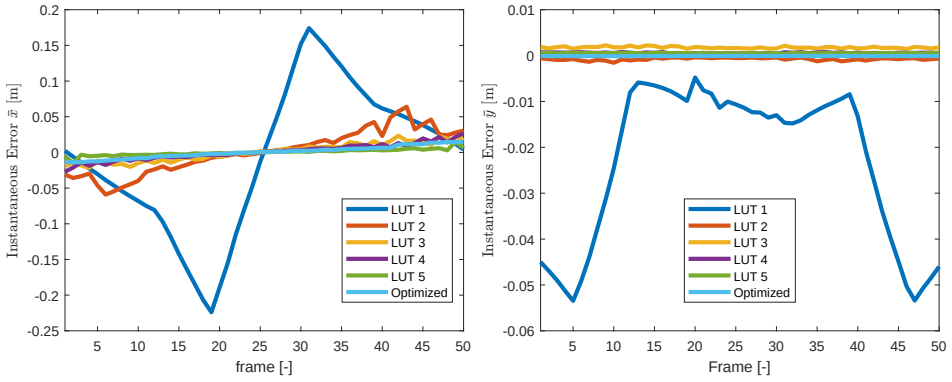

(a) C.o.G. location x.

(b) C.o.G. location y.

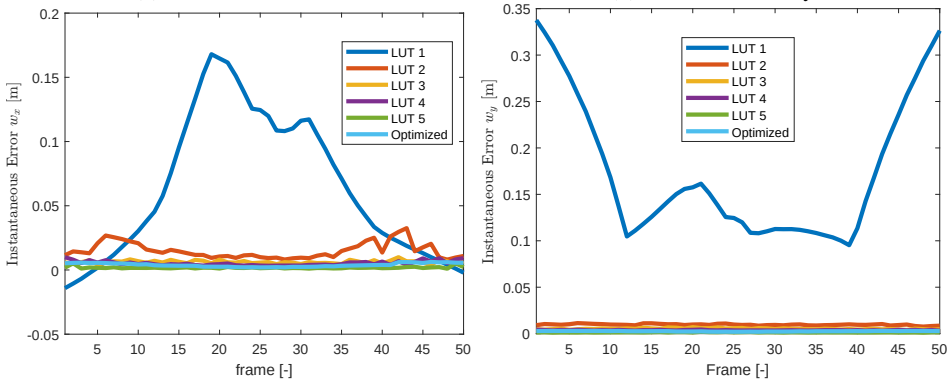

(c) Spot size x.

(d) Spot size y.

Fig. 36: Instantaneous error for lookup tables for a spot moving along $y = 0$ pix.

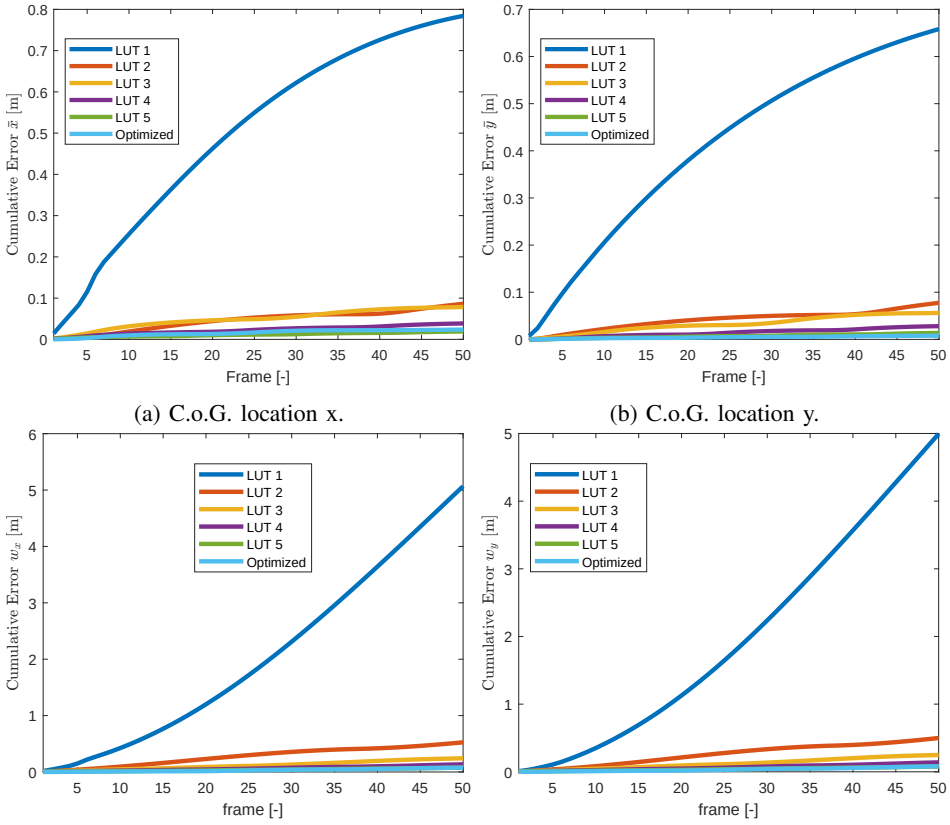

(a) C.o.G. location x.

(b) C.o.G. location y.

(c) Spot size x.

(d) Spot size y.

Fig. 37: Cumulative error for lookup tables for a spot changing size, which is centered in the image.

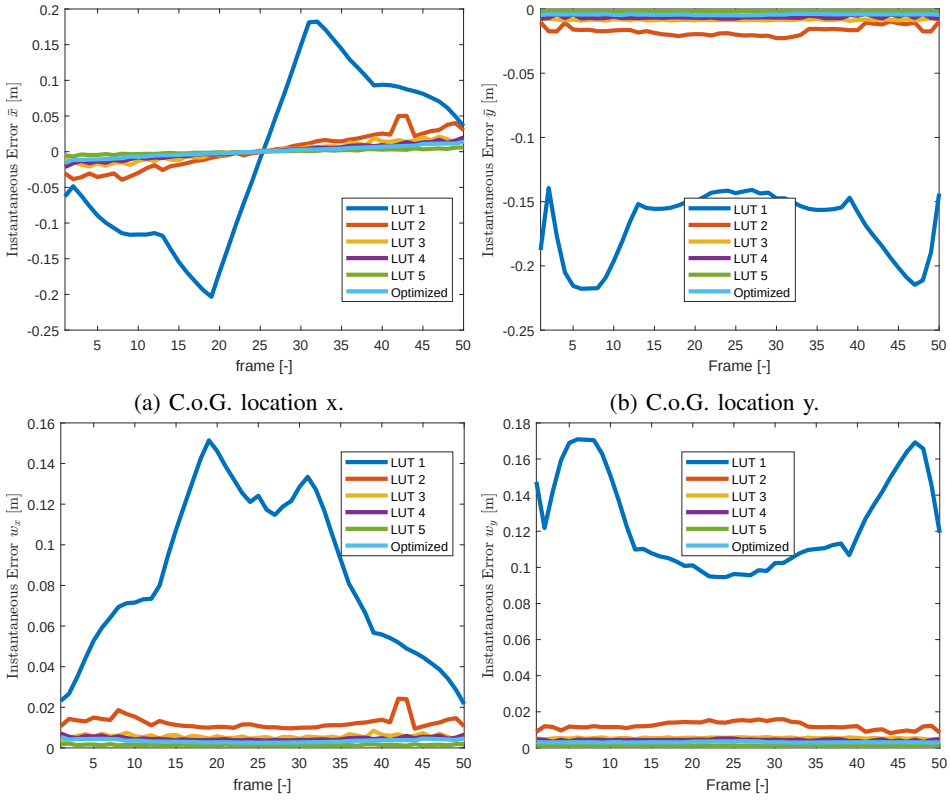

(a) C.o.G. location x.

(b) C.o.G. location y.

(c) Spot size x.

(d) Spot size y.

Fig. 38: Instantaneous error for lookup tables for a spot moving along $y = -100$ pix.

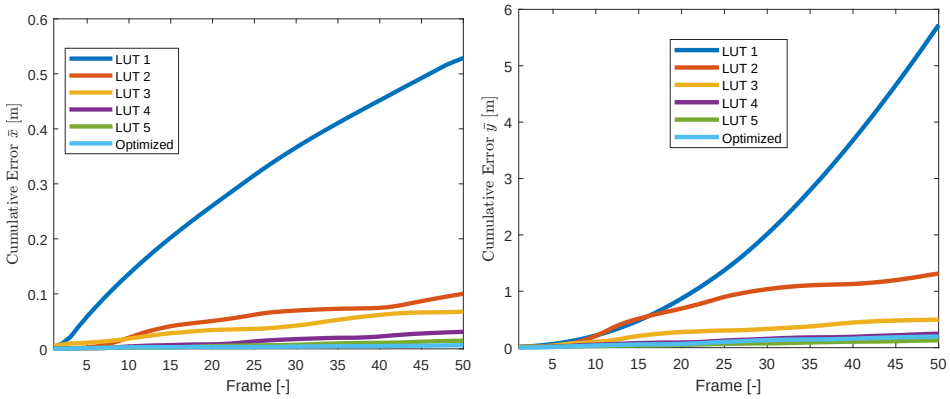

(a) C.o.G. location x.

(b) C.o.G. location y.

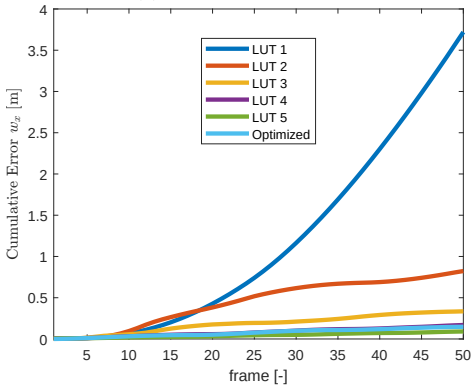

(c) Spot size x.

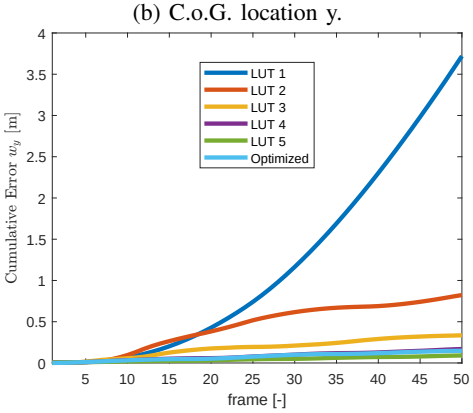

(d) Spot size y.

Fig. 39: Cumulative error for lookup tables for a spot changing size, which is offset in the image.

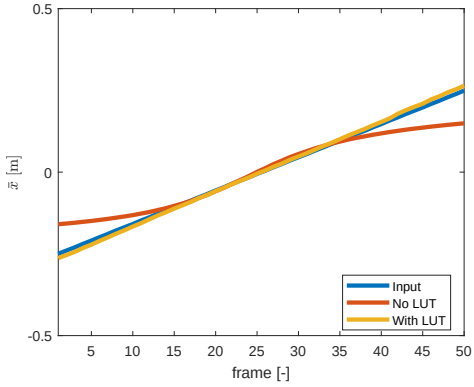

(a) C.o.G. location x.

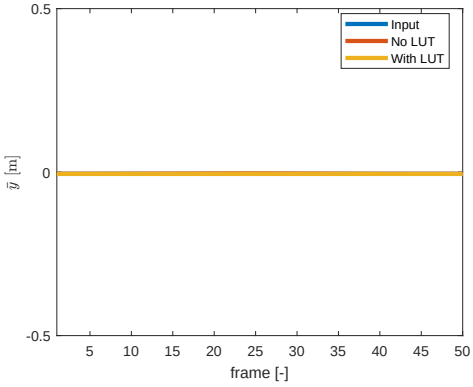

(b) C.o.G. location y.

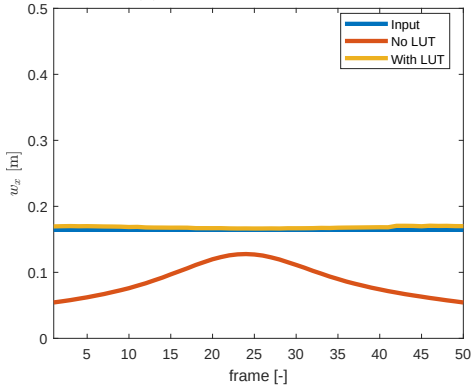

(c) Spot size x.

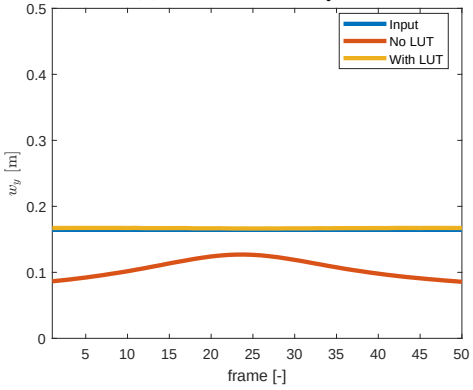

(d) Spot size y.

Fig. 40: Results of LUT 23 for a spot moving along $y = 0$ pix.

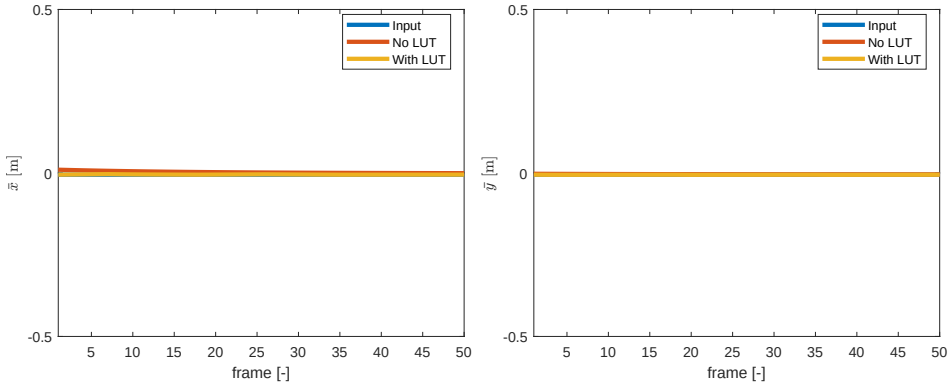

(a) C.o.G. location x.

(b) C.o.G. location y.

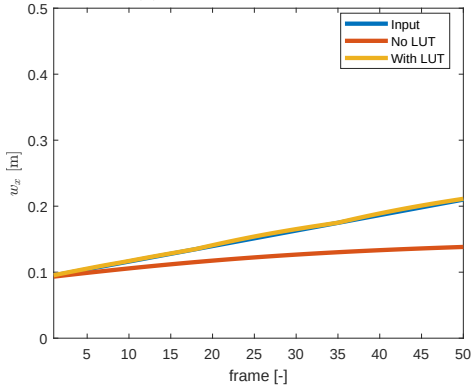

(c) Spot size x.

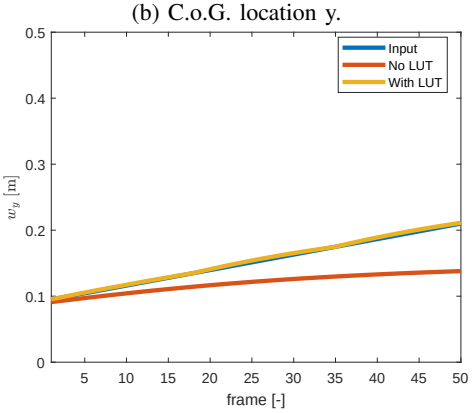

(d) Spot size y.

Fig. 41: Results of LUT 23 for a spot changing size, which is centered in the image.

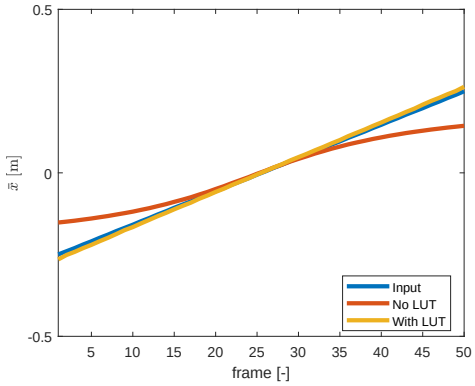

(a) C.o.G. location x.

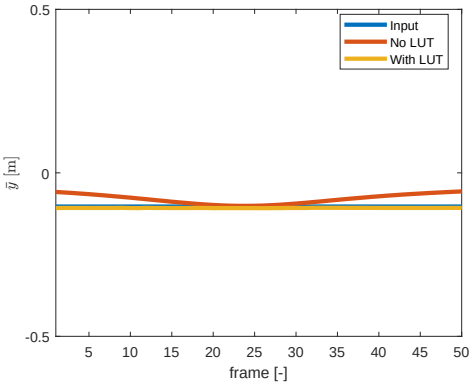

(b) C.o.G. location y.

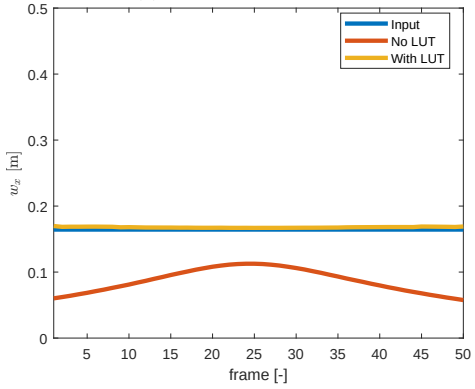

(c) Spot size x.

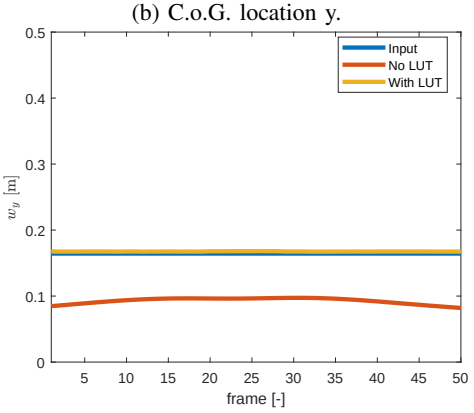

(d) Spot size y.

Fig. 42: Results of LUT 23 for a spot moving along $y = -100$ pix.

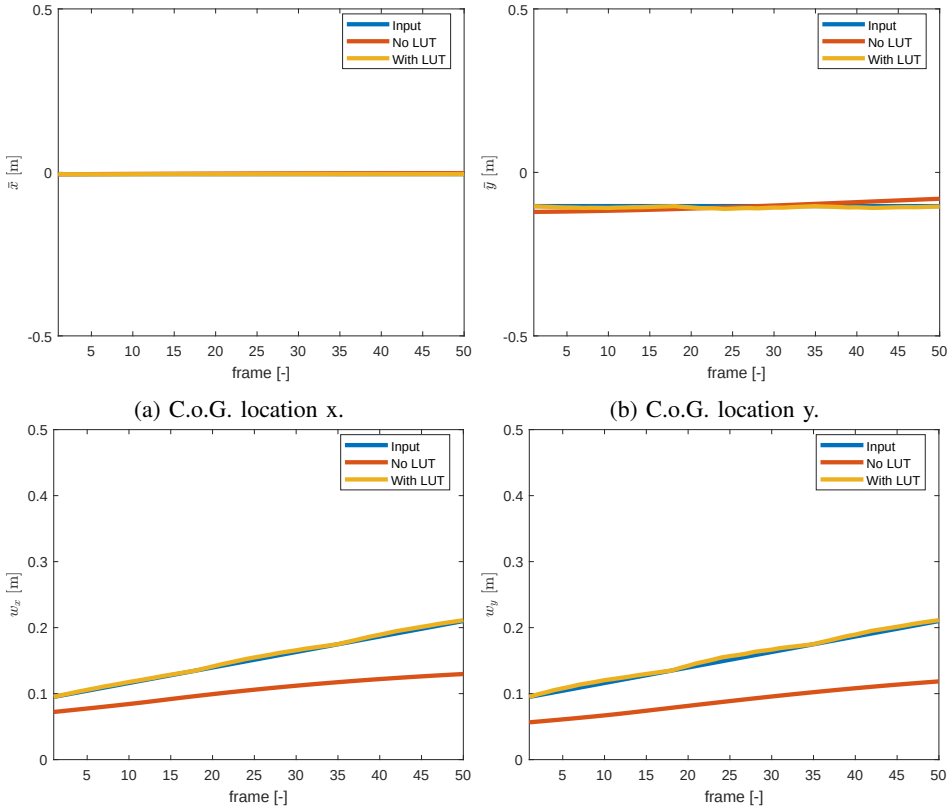

(a) C.o.G. location x.

(b) C.o.G. location y.

(c) Spot size x.

(d) Spot size y.

Fig. 43: Results of LUT 23 for a spot changing size, which is offset in the image.

G. Verification Data Analysis

To prove the functionality of the complete data analysis including lookup table even further, histograms have been made. These histograms focus on beam wander (subsubsection D-G1), short-term spot size (subsubsection D-G2) and scintillation (subsubsection D-G3).

1) Beam Wander: The beam wander should follow a Gaussian distribution [9]. Therefore, the beam wander results have been put in histograms for various analyzed measurements. As the histograms are all comparable, the histograms for one measurement are shown below, see Figure 44. As can be seen, the beam wander in x and y follow a Gaussian distribution. The median of the distribution does not lie at 0 m, because the tail of the histogram is slightly asymmetrical. However, this does not weaken the proof that the analysis provides a correct distribution.

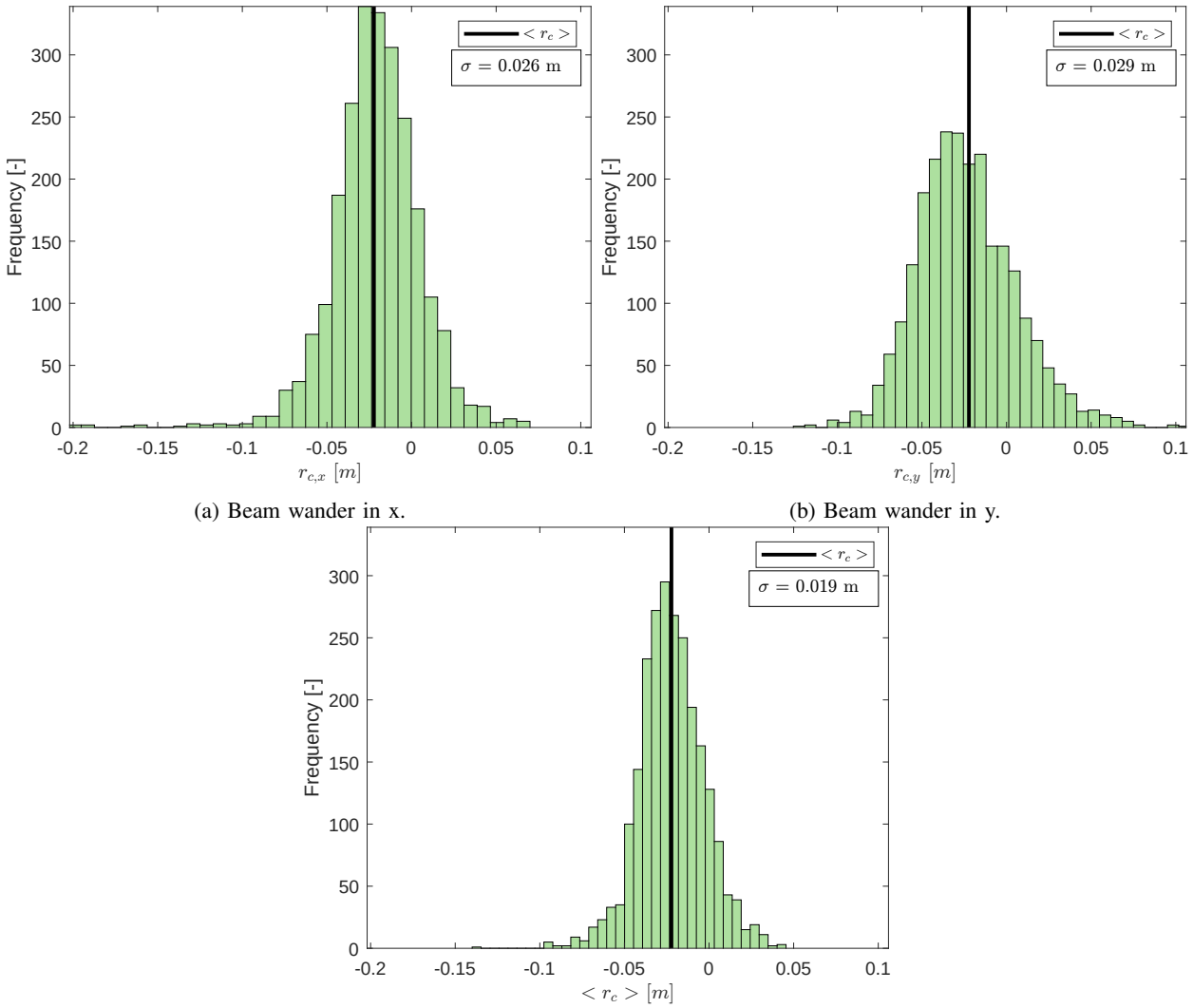

(a) Beam wander in x.

(b) Beam wander in y.

(c) Beam centroid displacement.

Fig. 44: Beam wander histograms for a measurement.

2) Spot Size: The spot size histograms for x and y and the combined result are shown in Figure 45. As can be seen, the spot size also follows a normal distribution, which is correct [9]. Note that the edges of the spot size are cropped, as the LUT accuracy requires a smaller spot size range to execute the analysis within a reasonable time (twelve days). For this particular run 4.6% of the results lie outside of this spot size range. Next to this, it becomes clear the spot is not circular but elliptical, with the horizontal axis as the major axis.

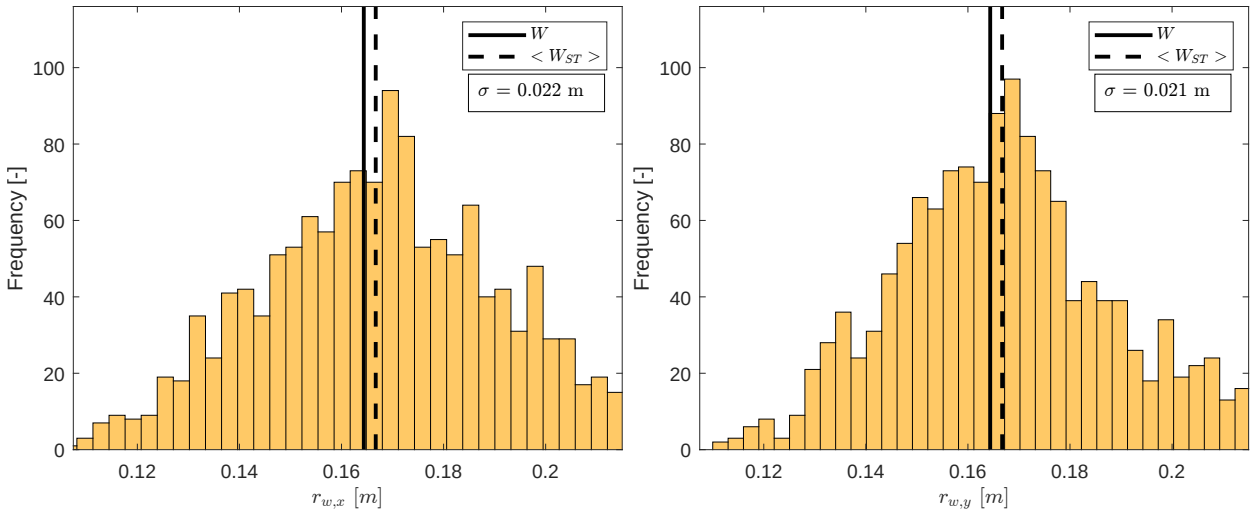

(a) Short-term spot size in x.

(b) Short-term spot size in y.

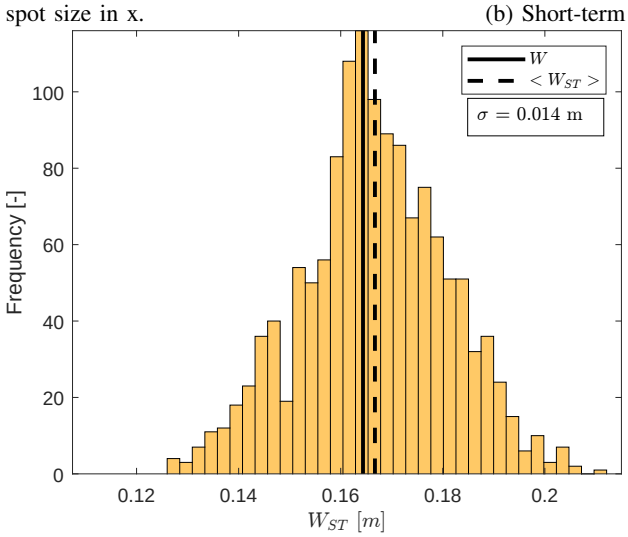

(c) Combined short-term spot size.

Fig. 45: Short-term spot size histograms for a measurement.

3) Intensity: The scintillation index can only be acquired accurately, if the image is not saturated. If the image is saturated, information is lost at the higher end of the intensity range. As the scintillation index is the "normalized variance of the intensity" [13], the intensity range must be available.

Figure 46 shows the histogram of the intensity for a single frame measurement. The intensity of all pixels is gathered. The zero values are omitted in this graph, as they are numerous with respect to the higher intensity values, as much of the aperture does not receive light. As can be seen on the right side, the spot intensity is retrieved while the absolute maximum intensity values saturate the camera.

The constructive interference spots of scintillation have a high intensity. The full well capacity of the CCD is fixed, thus the shuttertime must be decreased to increase its dynamic range and image the brightest spots. However, as the bit depth is also fixed, increasing the dynamic range to image the brightest spots leads to a loss of information in the most important part of the image: the generic spot.

This can be explained by looking at the histogram in Figure 46. Imagine the number of bars is kept equal, but, for example, the range is quadrupled. Then, instead of $\sim$11 bins containing information on the spot, only three bins would. The same would be the case for the pixel values of the camera. Increasing the dynamic range, leads to an increase in the intensity range included in each pixel value. Concluding, as the brightest spots cannot be reasonably imaged with a camera, while at the same time retrieving enough information of the rest of the spot, the spot is deemed acceptably captured to estimate the scintillation.

Halfway through the test, the transmitter power was changed from 0.2 W to 0.6 W. To ensure the validity of the analysis, the saturation is also checked for this part of the test. An overview of randomized runs from the second half of the field test are shown in Figure 47. As can be seen, the spot still does not saturate the receiver camera.

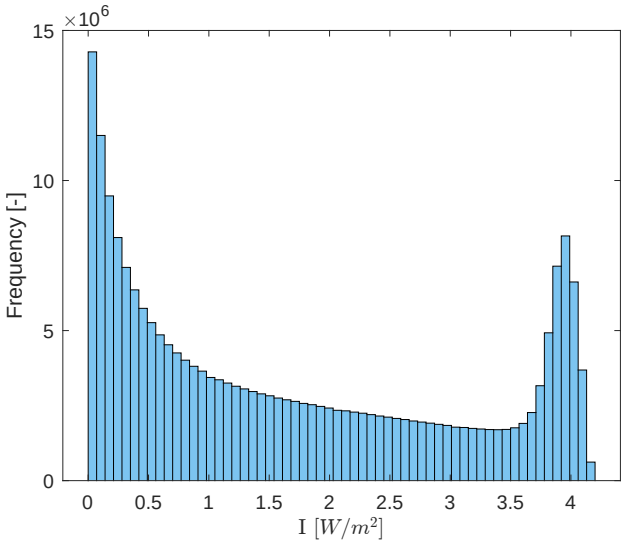

Fig. 46: Intensity histogram for a measurement with $P_{Tx} = 0.2\ W$ ($I = 0\ W/m^2$ omitted).

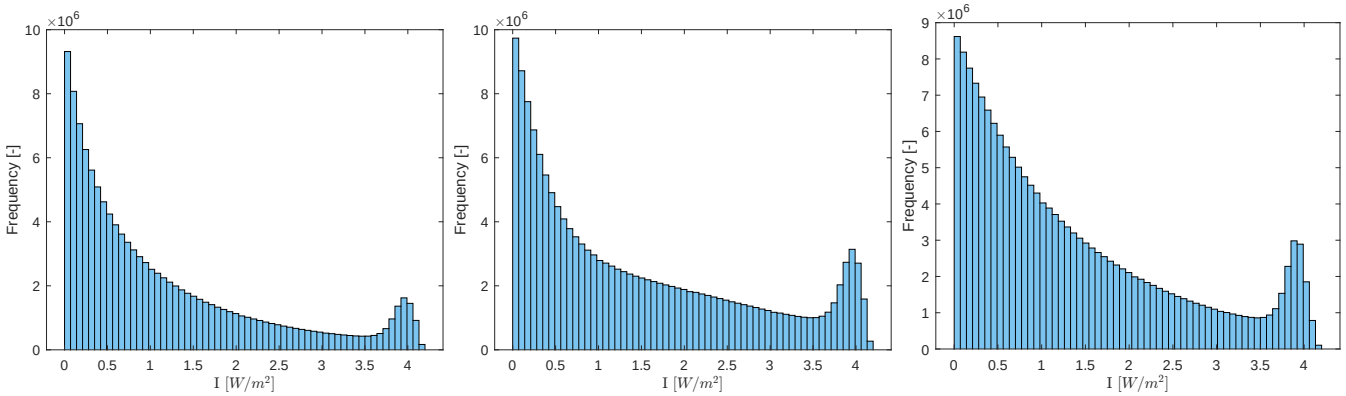

(a) Measurement 1223. (b) Measurement 1468. (c) Measurement 1730.

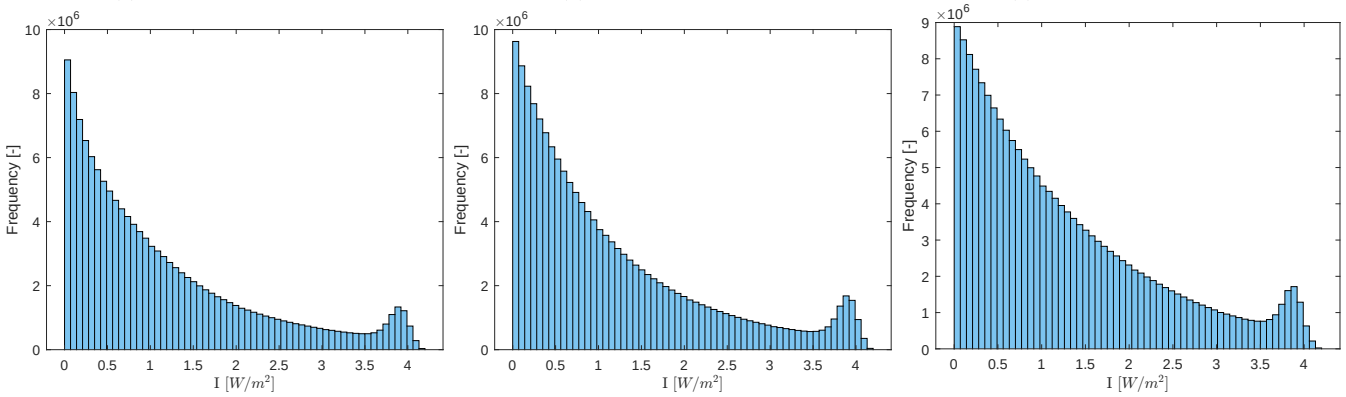

(d) Measurement 1918. (e) Measurement 2065. (f) Measurement 2704.

Fig. 47: Intensity histograms for measurements with $P_{Tx} = 0.6\ W$ ($I = 0\ W/m^2$ omitted).

H. Normalizing Results

To study the effect of higher order AO modes, the results of these higher modes can be normalized with respect to the tip/tilt results. Each higher AO mode (8, 16, 28, 40) in the test is preceded and succeeded by a tip/tilt measurement. The results for each higher AO mode can therefore be normalized by dividing its results by the results of the accompanying tip/tilt measurements, see Equation 59 for the normalization of long-term spot size results:

$$W_{LT,norm,m} = \frac{W_{LT,m,n}}{\frac{W_{LT,2,n-1}+W_{LT,2,n+1}}{2}}, \tag{59}$$

where $W_{LT,norm,m}$ $[-]$ is the normalized beam wander for m AO modes, n $[-]$ the measurement number and $W_{LT,2}$ $[m]$ the beam wander result for 2 AO modes.

APPENDIX E
ADAPTIVE OPTICS PRE-CORRECTION EFFECTS

Below, the empirical results are presented, showing the impact of Adaptive Optics. Furthermore, the simulations predicting the performance of tip/tilt pre-corrections and 28 AO modes are compared to the field test results.

A. Results

The normalized results for varying AO modes are shown in Figure 48. As can be seen in Figure 48a, the beam wander variance reduces for higher modes, except 40 modes. For 16 modes it can even be reduced for a factor 2.

The short-term and long-term spot size do not significantly change, see Figure 48b and Figure 48b. The reason the short-term spot size does not change significantly for changing turbulence conditions if higher AO modes are used, is that the spot size does not seem to be influenced by turbulence for the turbulence range analyzed in this research. Only for $C_n^2 >$ 5E-15 $m^{-2/3}$ does the spot start to increase significantly. However, due to the beam breaking up for those turbulence conditions this part is not analyzed. Thus, as turbulence does not influence the spot size for the turbulence conditions analyzed, the pre-correction can also not improve the performance. The performance is already optimal, as the spot size equals the free-space spot size.

The long-term spot size does not change significantly, even though the beam wander variance does, as the beam wander variance is very small, see Figure 15, which due to how Equation 19 is set up, does not lead to an increase in long-term spot size. The Pythagoras theorem limits the effect of a reduction in the already small beam wander. The short-term spot size is leading in this regard. However, that does not change significantly for higher AO modes.

The longitudinal, radial and on-axis scintillation index all decrease for higher AO modes, except for 40 modes. For all three scintillation indices, 8, 16 and 28 modes lie close together. The peak in normalized on-axis scintillation index for 28 modes at $C_n^2 =$6E-16 $m^{-2/3}$ is the result of an outlier.

The results for the average total received and on-axis power are shown in Figure 49. Again, the performance increases for 8, 16 and 28 AO modes, while the performance decreases for 40 AO modes.

Next to this, as can be seen, the received power stays reasonably consistent, if the turbulence strength increases. Only after $C_n^2 >$5E-15 $m^{-2/3}$, the power drops. This is the results of beam break up. Less power reaches the aperture and the the beam consist of several hot spots instead of a single one.

The total average received power for higher AO modes could higher than the results show. The reason for this is that the beam wander for higher AO modes, except 40 is less than for tip/tilt pre-correction. This means that more of the beam could be obscured by the beacon and secondary mirror leading to a lower measured received power than actually reaches the pupil plane.

The simulation results of TNO for tip/tilt pre-correction are shown in Figure 50. As can be seen, the simulation results generally lie closer than the theoretical results. However, the spread in on-axis and longitudinal scintillation is very large. This large spread is not found in the theory on which it is based. This raises questions on the implementation of the scintillation theory in the simulation software.

The simulation results of TNO for 28 AO modes are shown in Figure 51. The beam wander variance in the simulation is estimated to be zero, which retrieved to be nonzero from the field test.

The simulation results for long-term and short-term spot size match the empirical results more closely than for the tip/tilt pre-correction. The mean of the empirical results lies close to the lower end of the simulation results. Again the simulated scintillation results contain a large spread. Especially for the on-axis scintillation index, the empirical and simulation results deviate more than for the tip/tilt-corrected results.

B. Conclusion

Concluding, the reduction in beam wander predicted by the simulation results matches the empirical results, even if it is set to zero in the simulation for 28 modes. The amount of reduction deviates between simulation and field test, though. Furthermore, the reduction in scintillation measured during the field test is not represented in the simulation results. The measured spot size does not change significantly for higher AO modes, which it does for the simulated results.

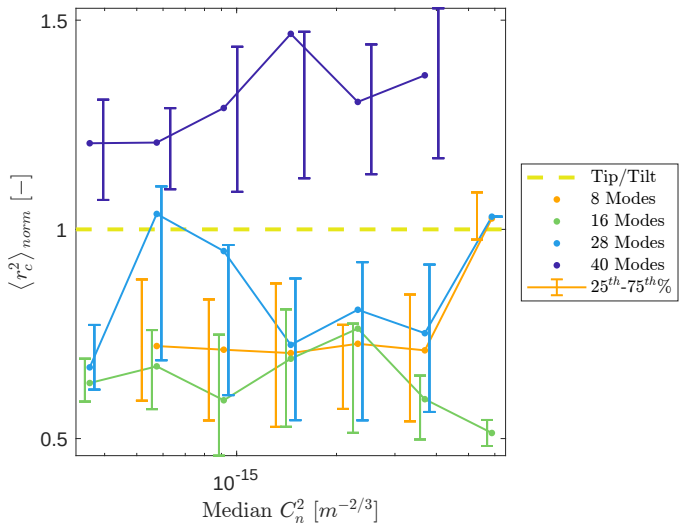

(a) Normalized beam wander variance.

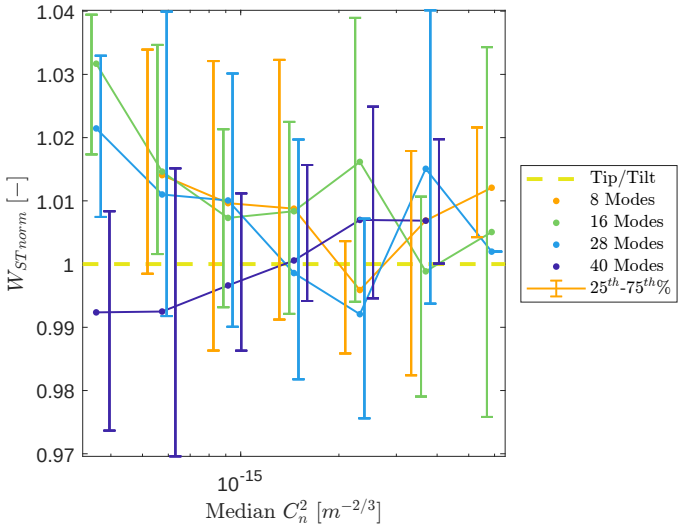

(b) Normalized short-term spot radius.

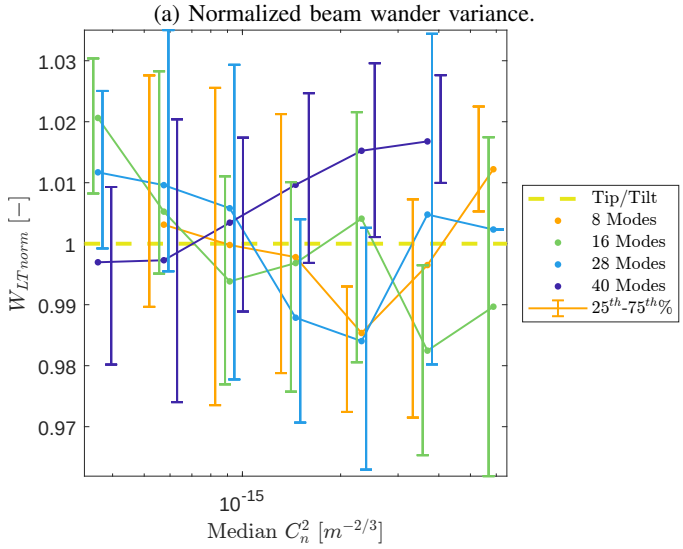

(c) Normalized long-term spot radius.

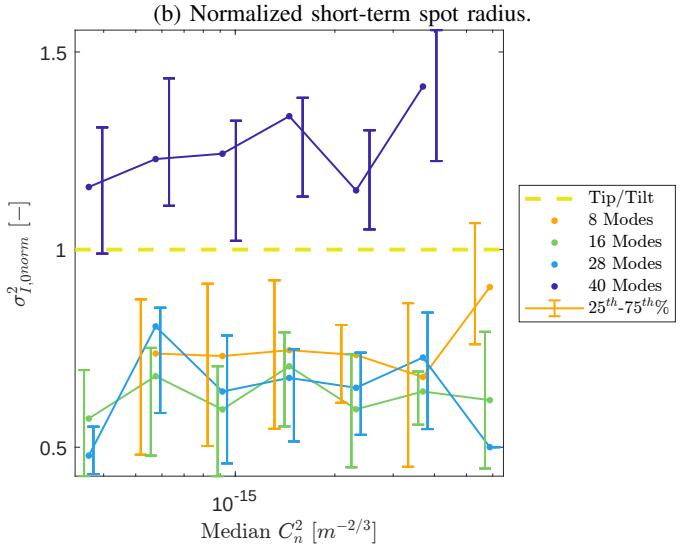

(d) Normalized longitudinal scintillation.

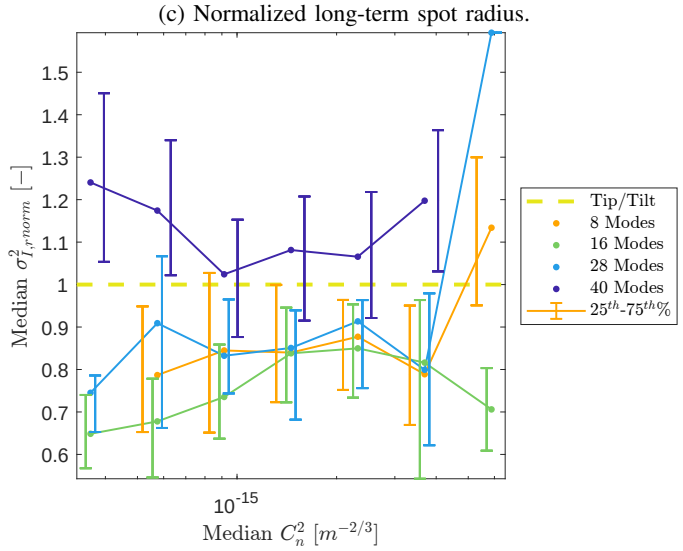

(e) Normalized radial scintillation.

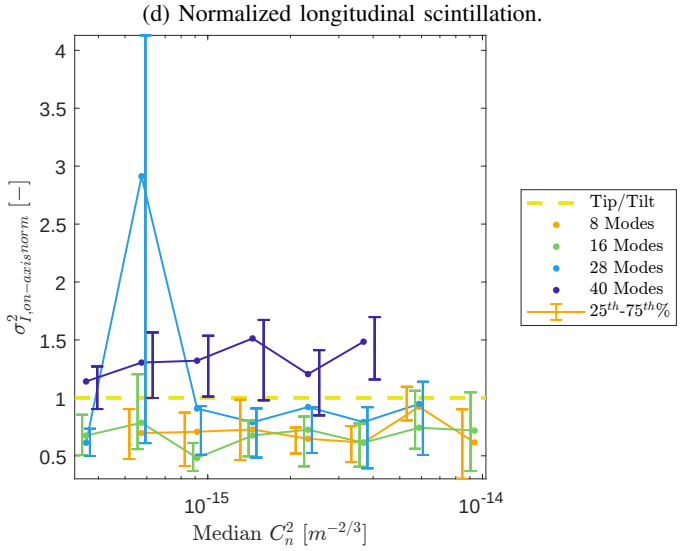

(f) Normalized on-axis scintillation.

Fig. 48: Normalized results of field test data.

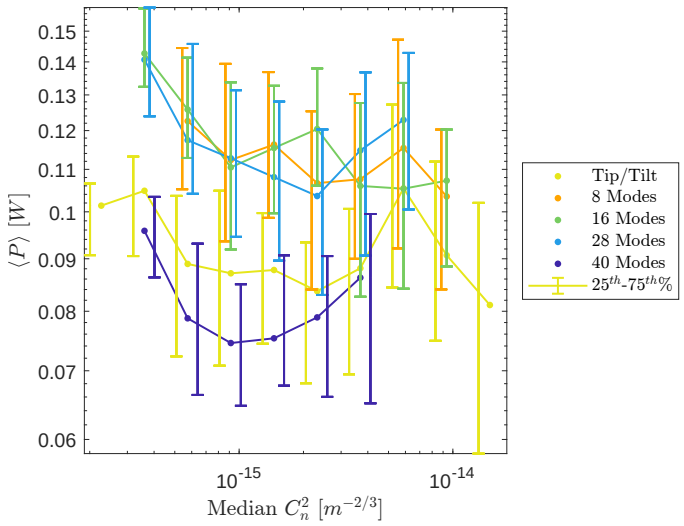

(a) Total received power.

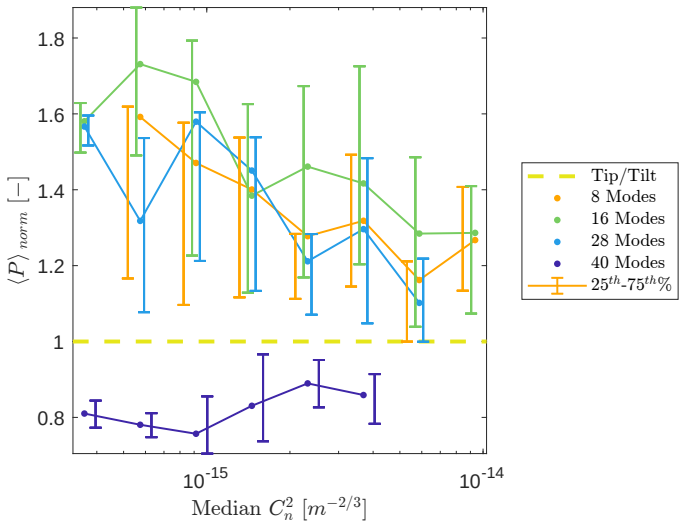

(b) Normalized total received power.

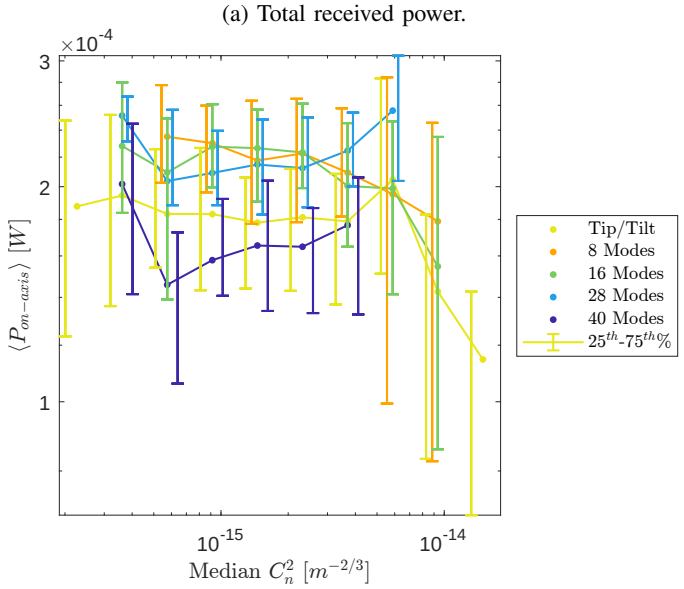

(c) Received on-axis power.

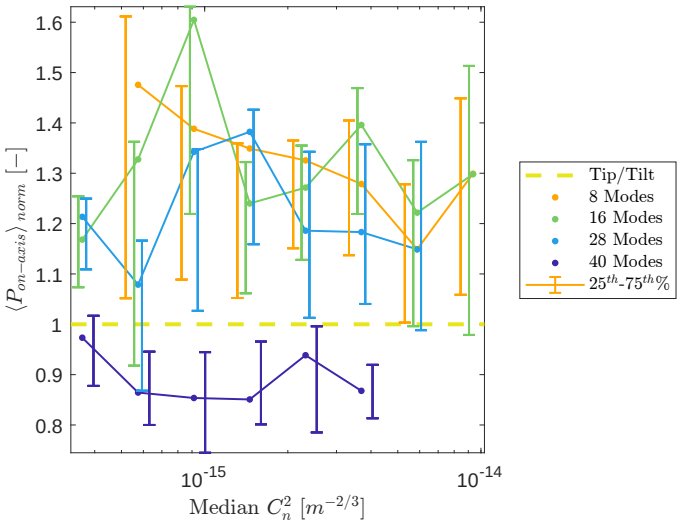

(d) Normalized received on-axis power.

Fig. 49: Results of received power in the field test.

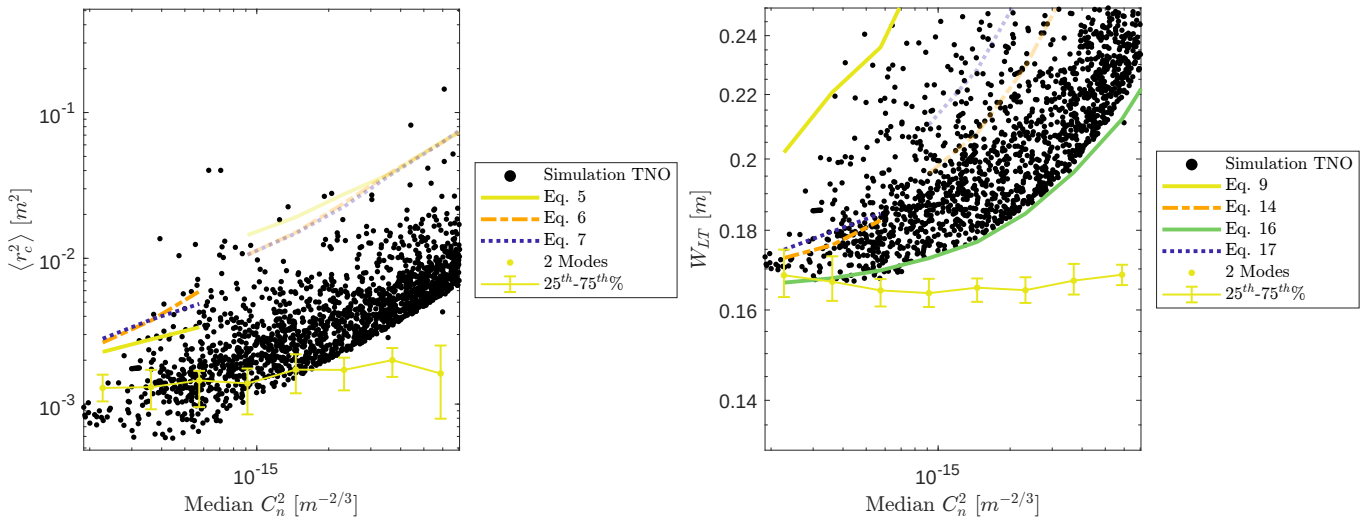

(a) Beam wander variance.

(b) Long-term spot radius.

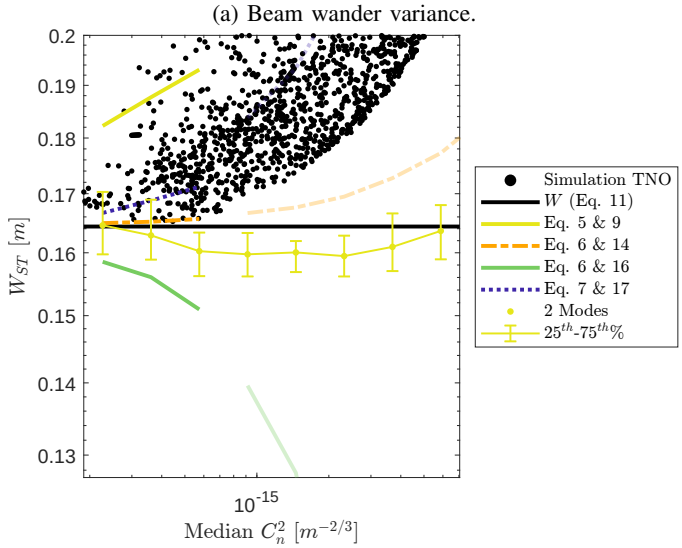

(c) Short-term spot radius.

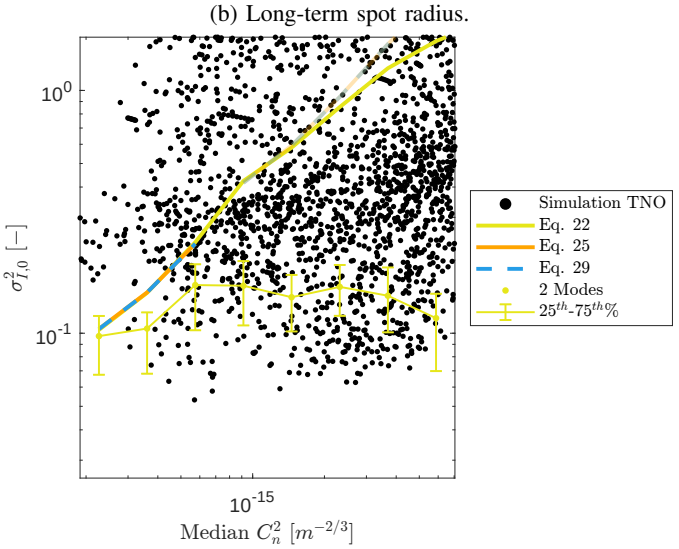

(d) Longitudinal scintillation.

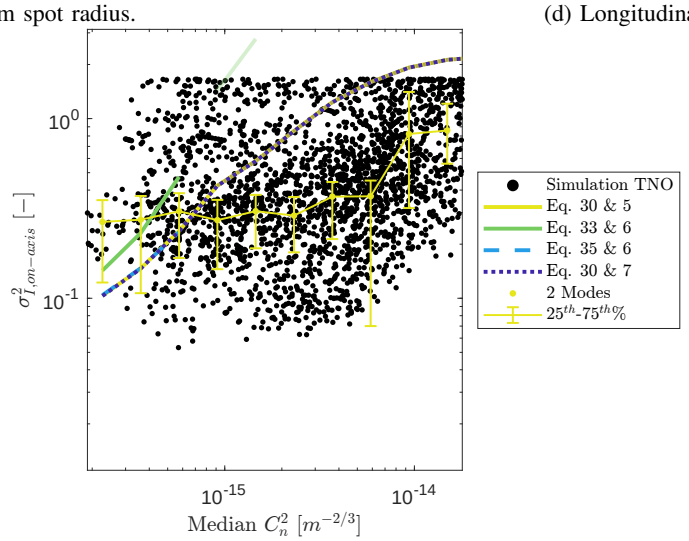

(e) On-axis scintillation.

Fig. 50: Tip/Tilt pre-correction results of field test data and TNO simulation software.

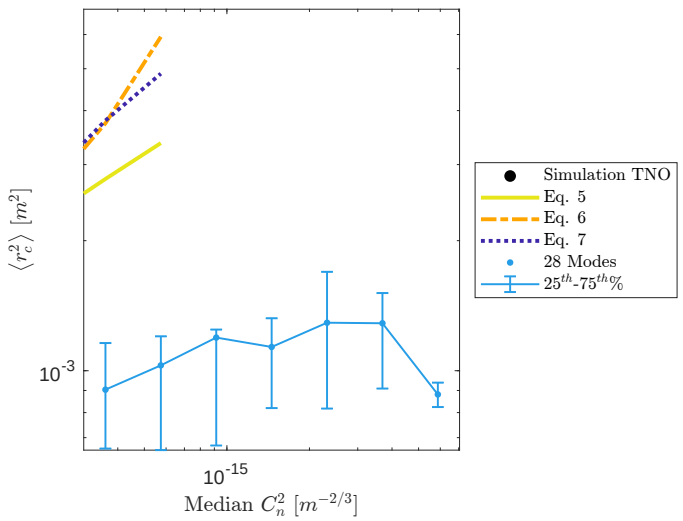

(a) Beam wander variance.

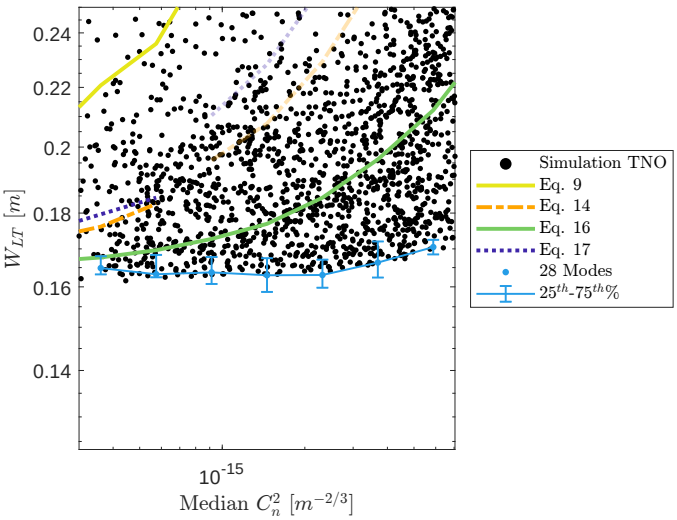

(b) Long-term spot radius.

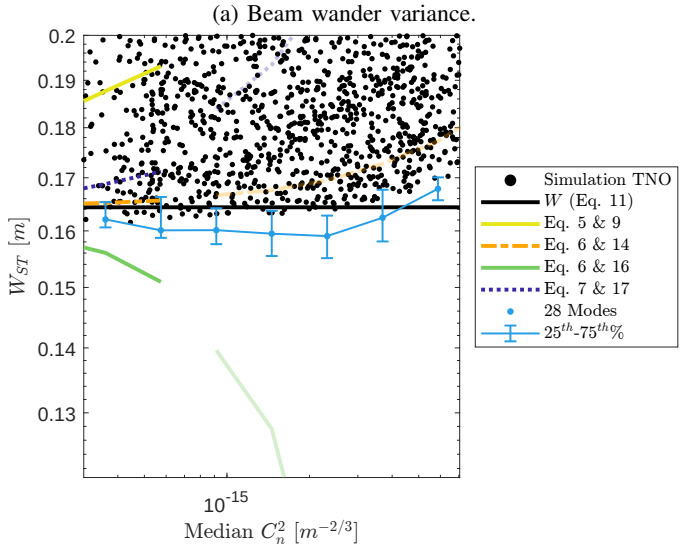

(c) Short-term spot radius.

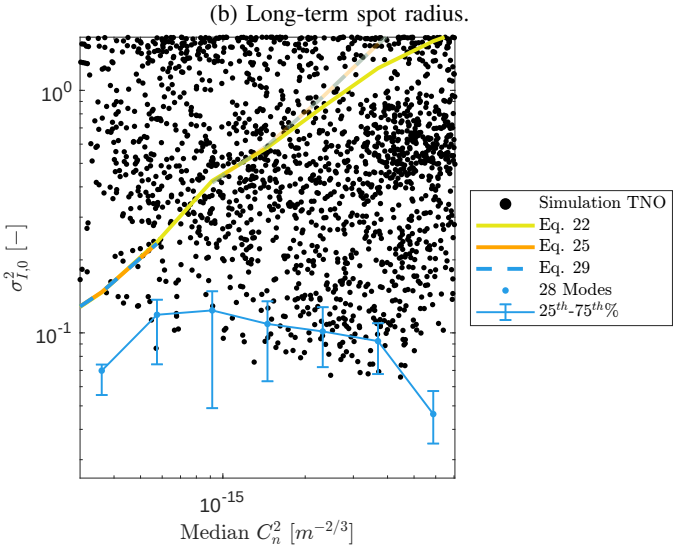

(d) Longitudinal scintillation.

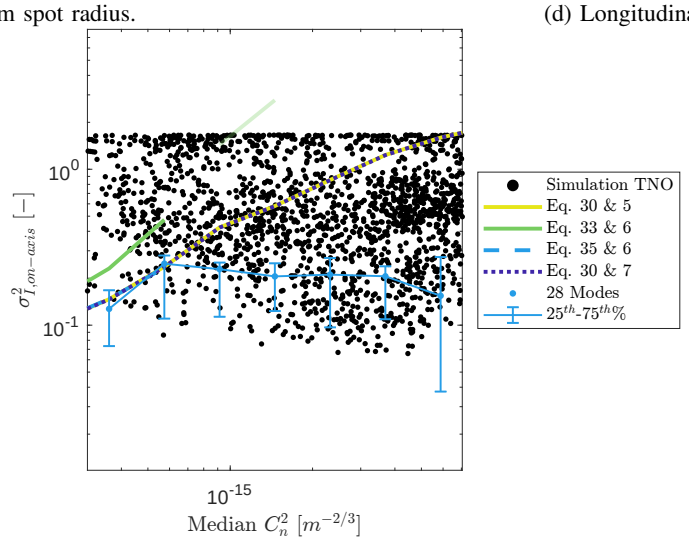

(e) On-axis scintillation.

Fig. 51: 28 AO modes results of field test data and TNO simulation software.

APPENDIX F
RECOMMENDATIONS

Following the research performed, several recommendations can be given for future research and developments.

A. Data Analysis

The data analysis could be extended in several ways.

- The orientation of the elliptical Gaussian beam could be retrieved via singular value composition. However, the lookup table should be adjusted to implement rotation of elliptical beams.
- The lookup table could be extended with the use of speckles for its creation. However, as scintillation is a random process influenced by the current turbulence conditions, the lookup table size would grow substantially.
- Removing the system and beam jitter from the beam wander results, will lead to a more direct comparison with theory.
- Currently, beam break up is not analyzed even though the data analysis shows it starts to play a significant role for strong turbulence conditions. By analyzing the effect of beam break up, it can be characterized for changing turbulence strengths. This is also the case for the various AO modes, as it has been found that beam break up for higher AO modes occurs at higher turbulence conditions than for tip/tilt pre-correction.
- The time of day, wind speed and wind direction can be used to get more insight in how the empirical result scatter plots are built up. Once could even differ the mean empirical results on this basis to get a clear indication of the differences.
- The GTB uses the downlink beam for pre-correction. However, in this research the quality and power of the received beacon is not included in the analysis. There might be runs where those are too low for pre-correction of an acceptable quality. By adding this to the data analysis, additional outliers might be found and removed.
- The wavefront error of the uplink beam at the GTB can be included in the data analysis to understand how much the uplink beam is already distorted.
- The beam wander analysis is influenced by the accuracy and speed of the tip/tilt pre-correction algorithm. By checking the control response to the beam displacement response, one could find how much of the beam wander can still be mitigated by improvement of the control algorithms and speed.

B. Test Setup

The Beam profiler setup can be improved in several ways:

- Tracking of the Beam Profiler location would increase the accuracy of the beam wander variance. The Gerbrandy tower sways, and thus the location of the Beam Profiler changes. By measuring the movement of the Beam Profiler, the tower sway can be removed from the measurements.
- If the beam jitter (angle of arrival fluctuation) are removed from the measurements, the accuracy of the beam wander variance analysis improves. However, this would require additional instruments at the retriever side.
- If another test is performed, an increase in the imaged plane size and omitting of an obscuration will lead to a higher accuracy of the data analysis. Currently, the clipped and obscured intensity information is estimated by the lookup table.

Furthermore, the turbulence profile accuracy can be improved as follows:

- The accuracy of the C_n^2 profiles could be improved by simulating the turbulence using weather data and measurements of the turbulence monitor data. This way the linear interpolation can be changed to a more accurate estimation.
- For a next test, the turbulence monitors on the tower should be placed further from the tower platform. Currently, the tower structure will influence the turbulence monitor measurements. As these turbulence monitors influence the median C_n^2 value used in the comparison, an improvement in their accuracy will lead to an improvement in the accuracy of the median C_n^2.

An improvement of the accuracy of the turbulence profiles will lead to a more accurate comparison between theory and measurements.

C. Analytic Equations

The research showed that the theory can be improved as follows:

- It has been shown that the time of day, wind speed and wind direction have an impact on the turbulence effects. To improve the accuracy of the theory, these influences should be reflected in the theory, as well.
- Beam break up plays a role for strong turbulence conditions, especially for tip/tilt pre-correction. It should be investigated if and how beam break up is currently included in the theoretical models and if it should be added or changed. It should then also be decided how the spot size is defined if multiple hot spots exist. Understanding of beam break up is especially important for ground-to-GEO links, as a small angular break up near the ground station grows has grown much larger after such a long propagation distance.

D. Simulation Software

The simulation software at TNO can improved in several ways:

- One way is by tracking down why the spread in scintillation index is large.
- The other improvement is to update the theory on which the simulation is based to analytical equation which lie close for the individual turbulence effects. Note that for ground-to-GEO links, the horizontal path models cannot be used.
- The beam wander displacement for higher order AO modes does not equal zero m, as perfect tracking is impossible. A reasonable estimate of the beam wander displacement should be made for higher order AO modes.

APPENDIX G
ADDITIONAL FIGURES

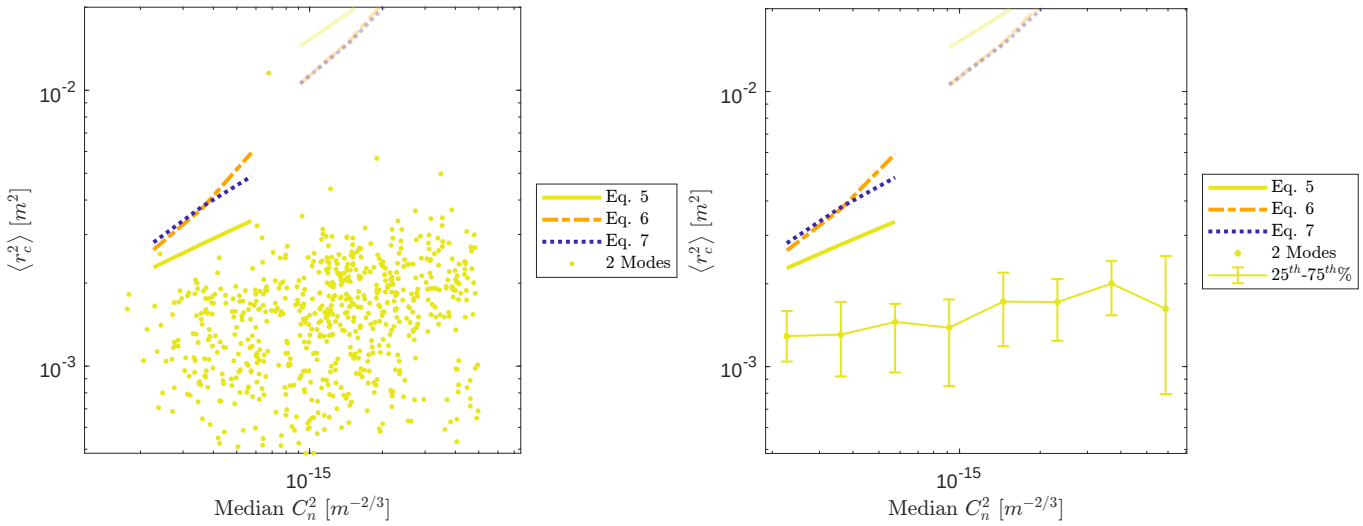

(a) Scatter plot.

(b) Grouped plot.

Fig. 52: Beam wander variance results for tip/tilt pre-correction.

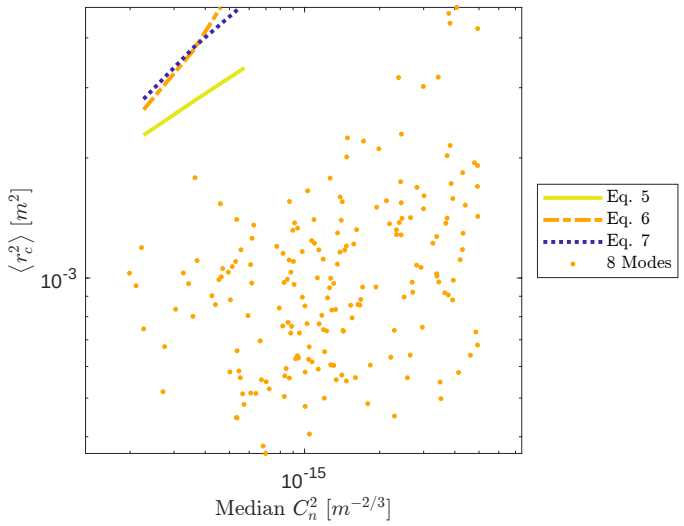

(a) Scatter plot.

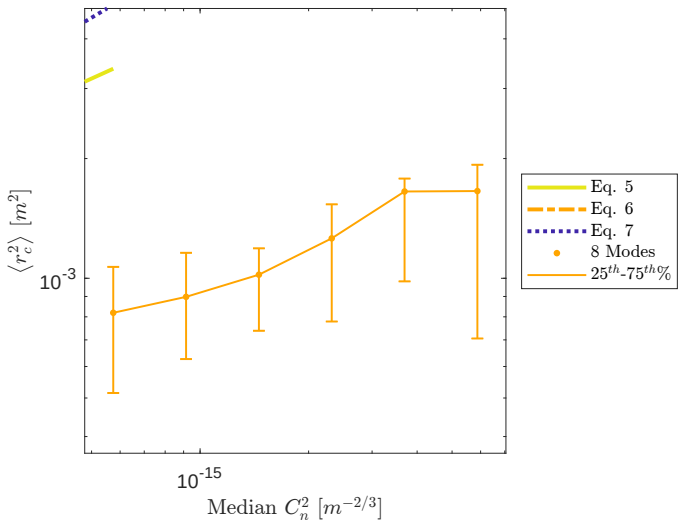

(b) Grouped plot.

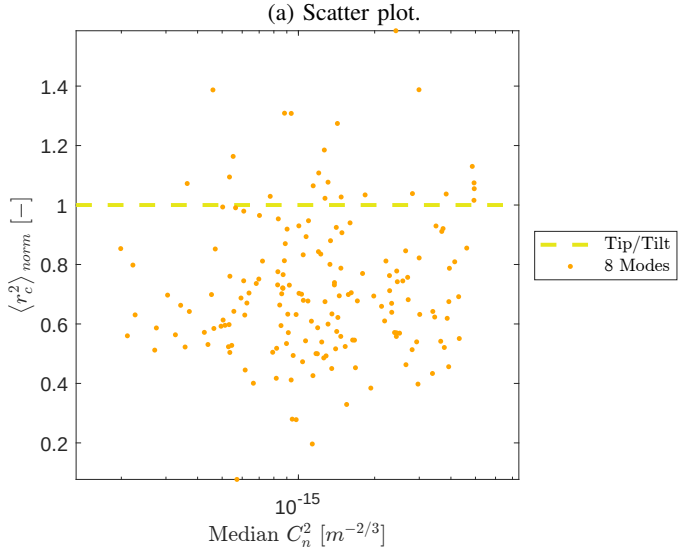

(c) Normalized scatter plot.

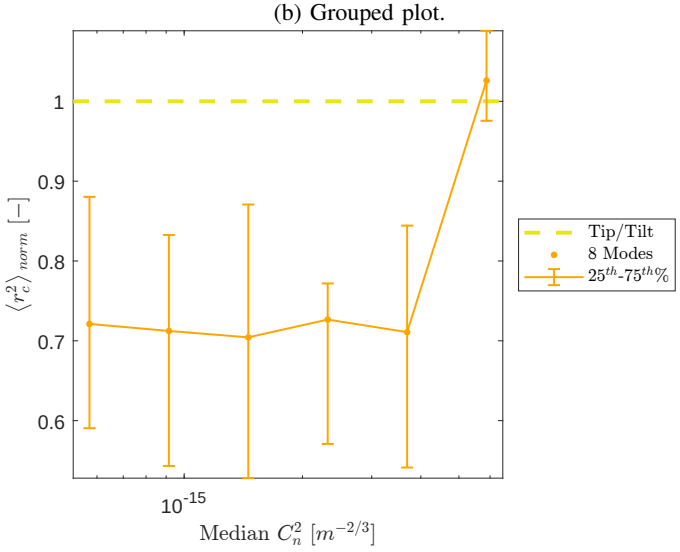

(d) Normalized grouped plot.

Fig. 53: Beam wander variance results for 8 AO modes.

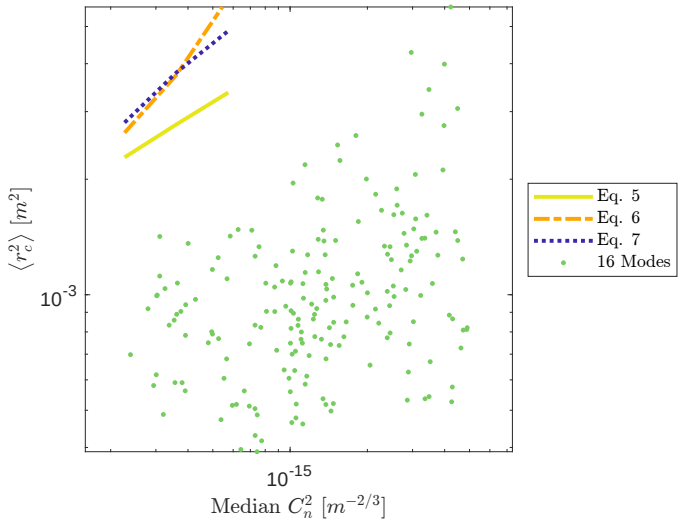

(a) Scatter plot.

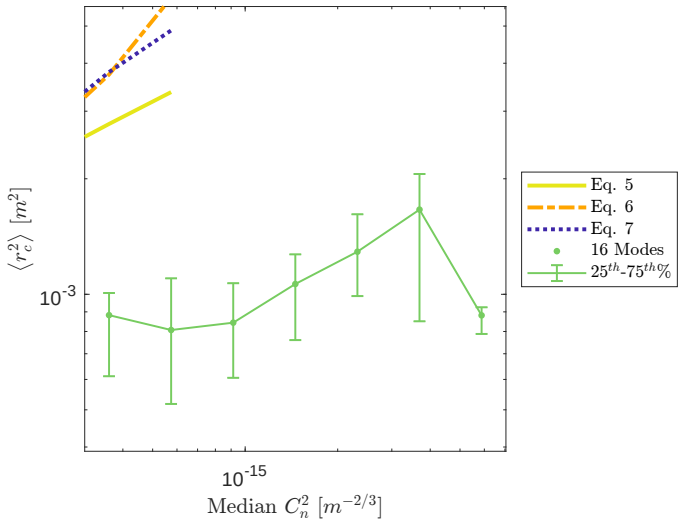

(b) Grouped plot.

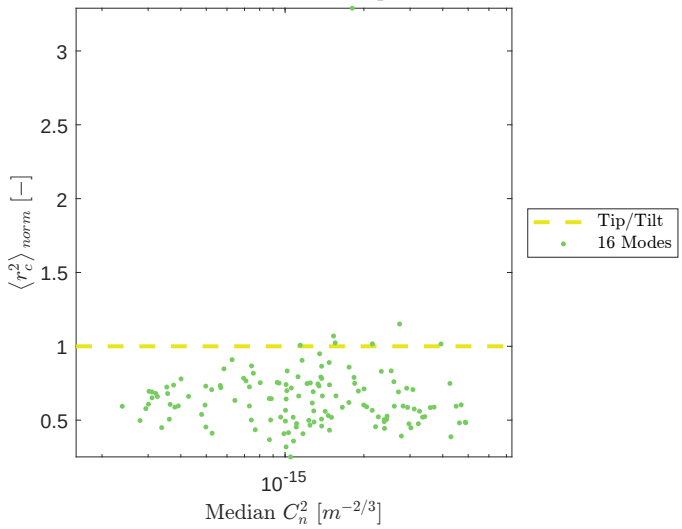

(c) Normalized scatter plot.

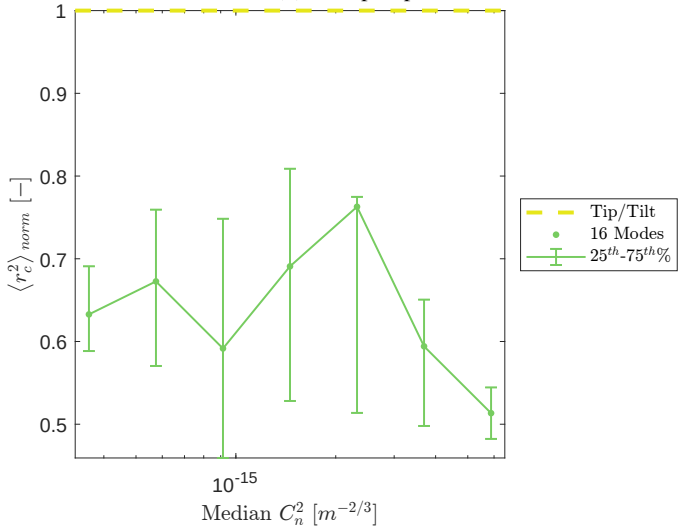

(d) Normalized grouped plot.

Fig. 54: Beam wander variance results for 16 AO modes.

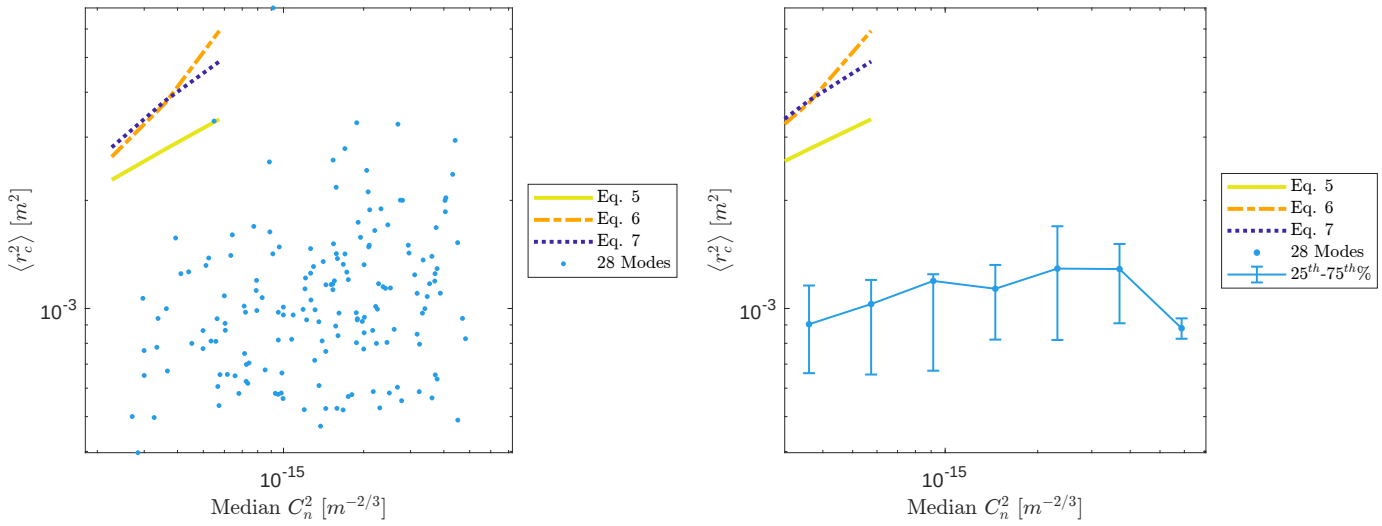

(a) Scatter plot.

(b) Grouped plot.

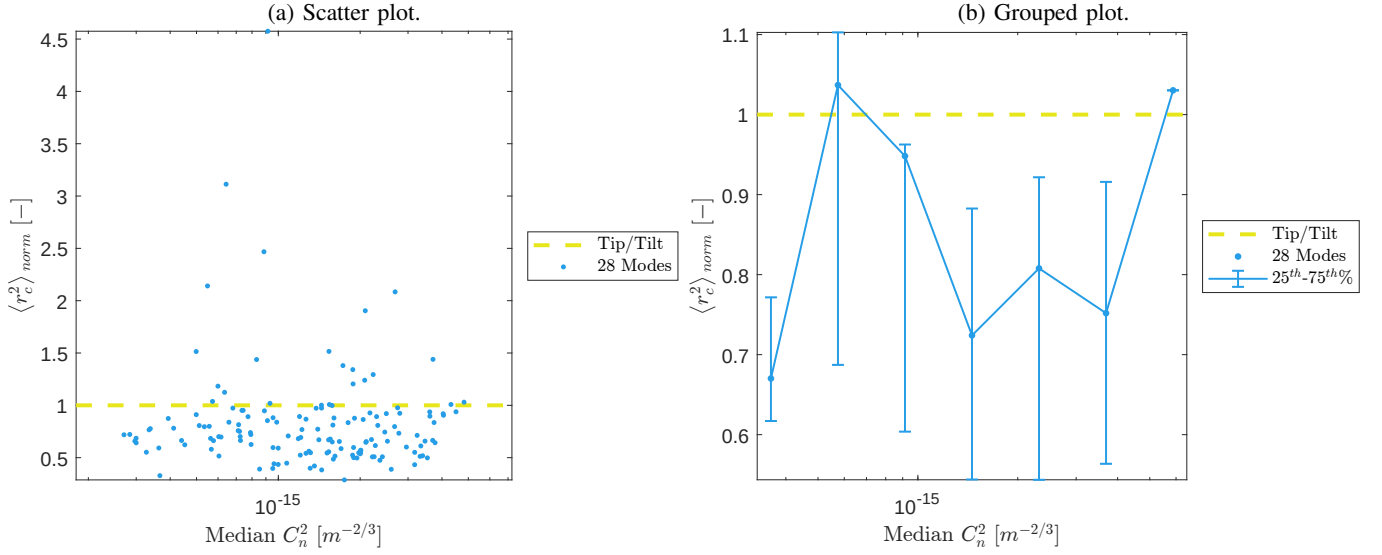

(c) Normalized scatter plot.

(d) Normalized grouped plot.

Fig. 55: Beam wander variance results for 28 AO modes.

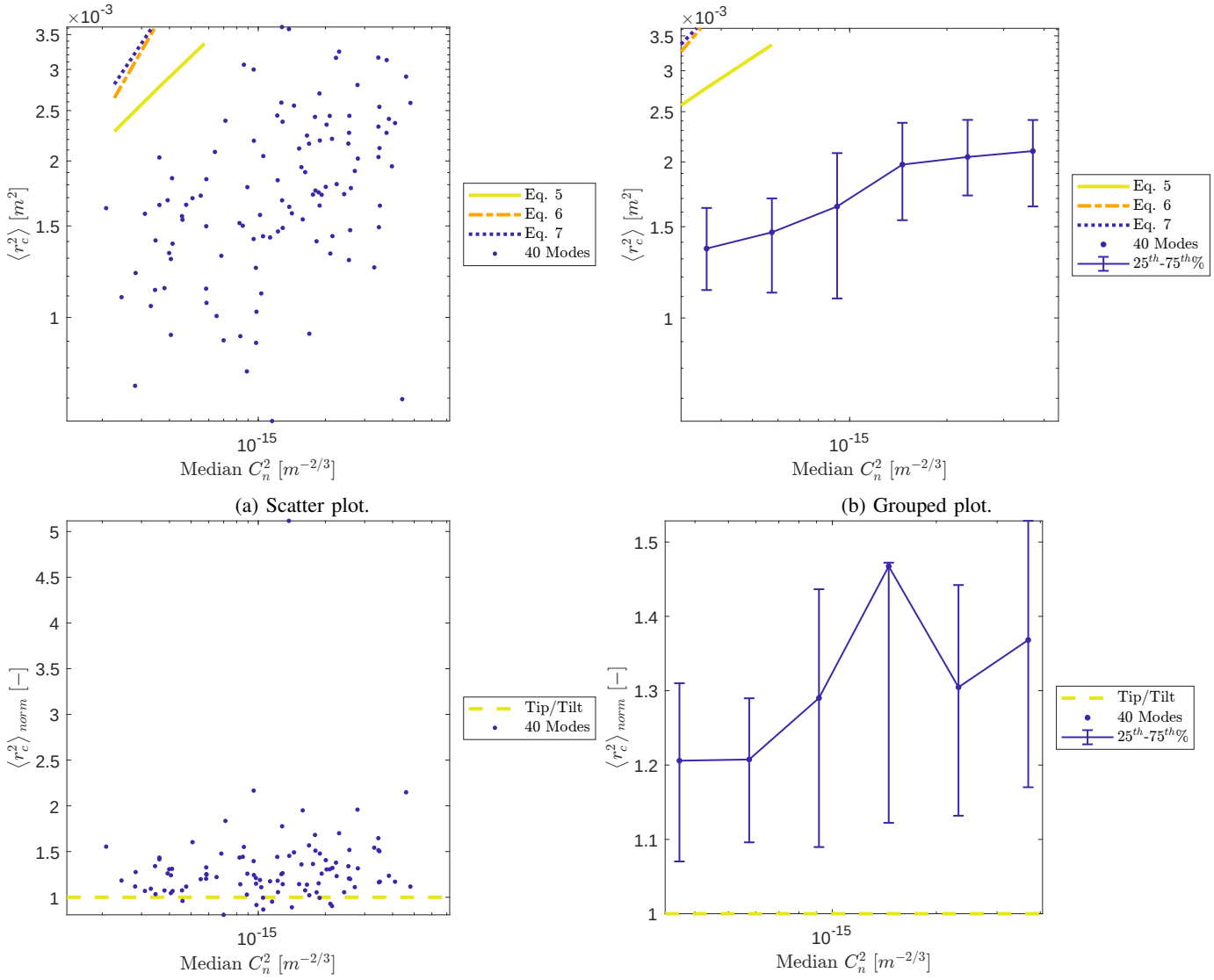

(a) Scatter plot.

(b) Grouped plot.

(c) Normalized scatter plot.

(d) Normalized grouped plot.

Fig. 56: Beam wander variance results for 40 AO modes.

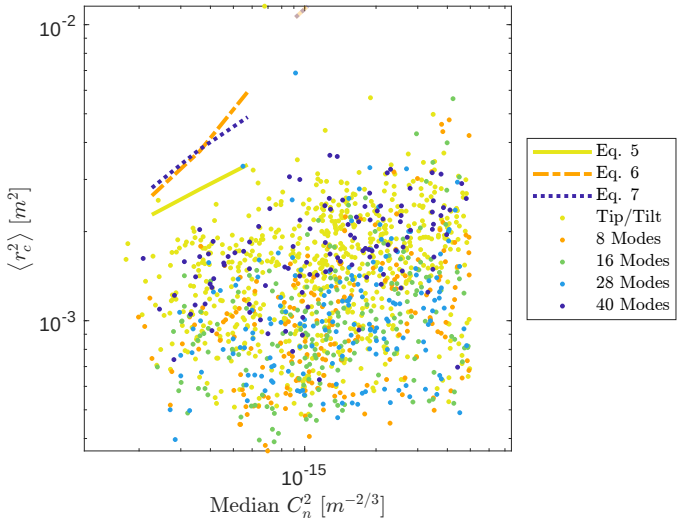

(a) Scatter plot.

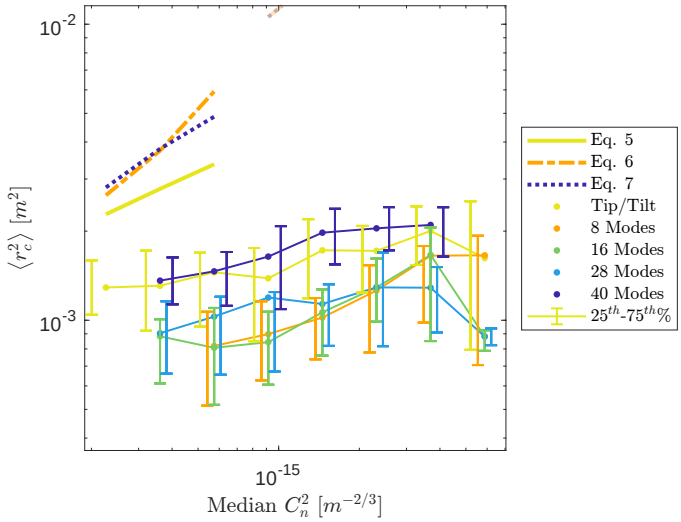

(b) Grouped plot.

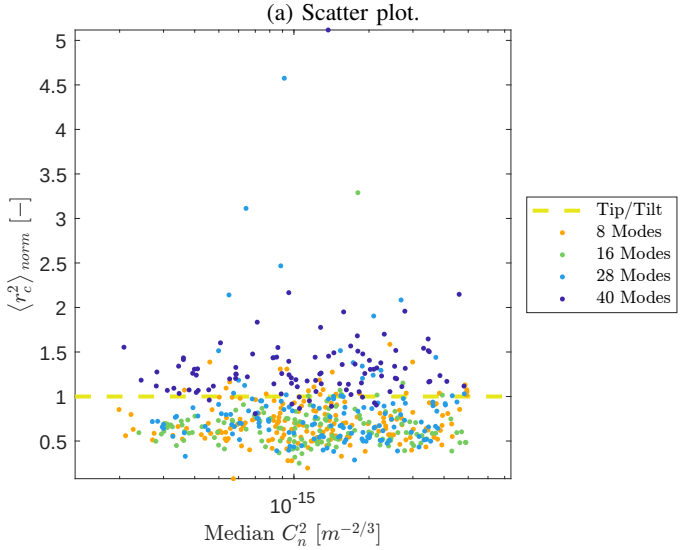

(c) Normalized scatter plot.

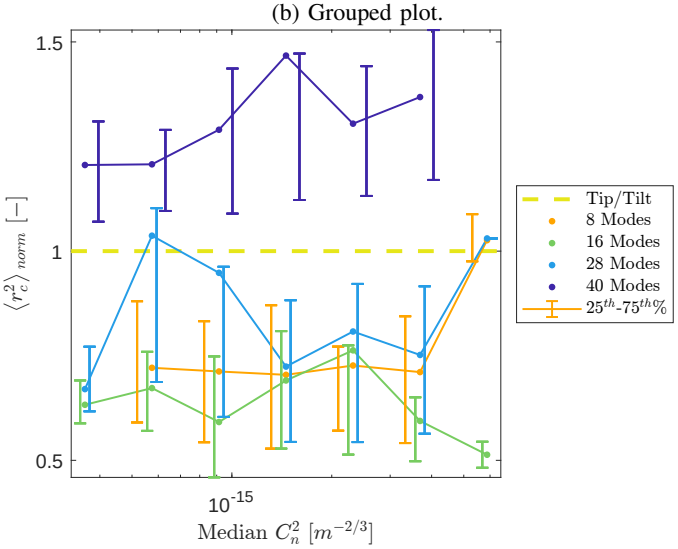

(d) Normalized grouped plot.

Fig. 57: Beam wander variance results for all AO modes.

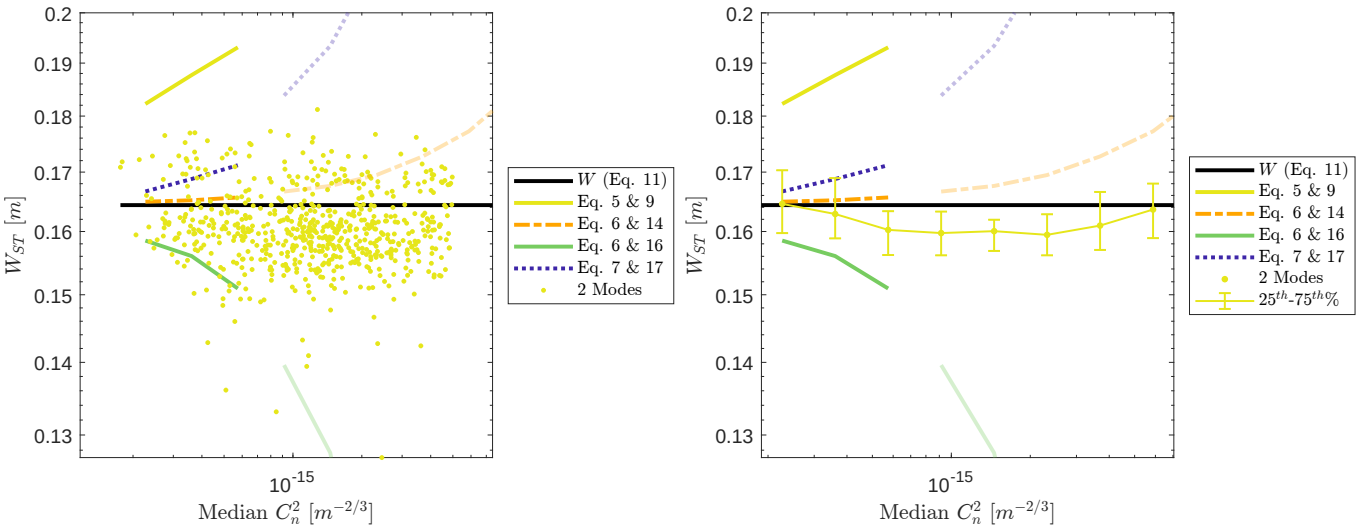

(a) Scatter plot.

(b) Grouped plot.

Fig. 58: Short-term spot size results for tip/tilt pre-correction.

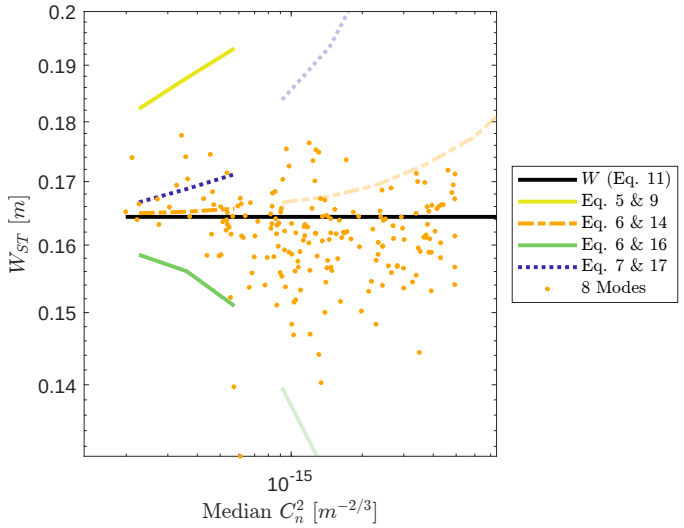

(a) Scatter plot.

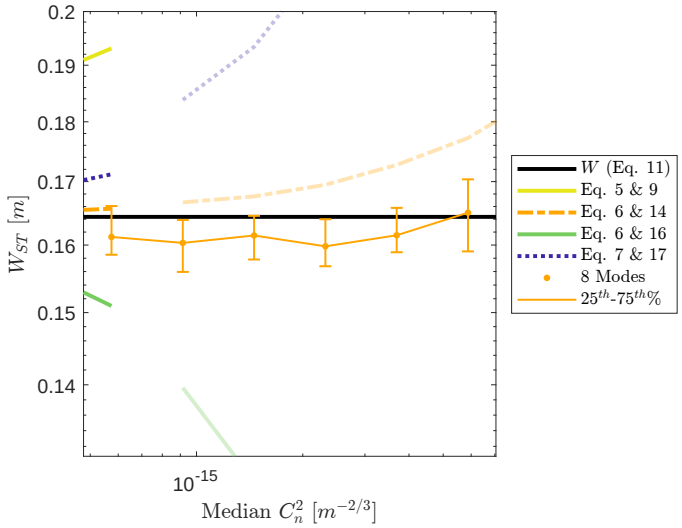

(b) Grouped plot.

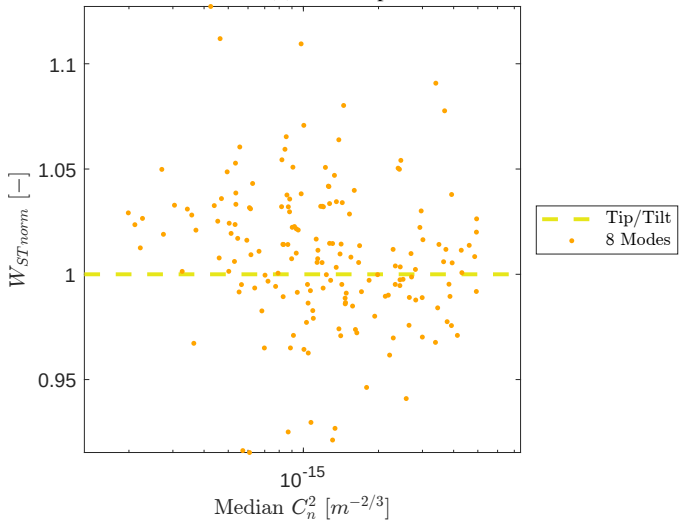

(c) Normalized scatter plot.

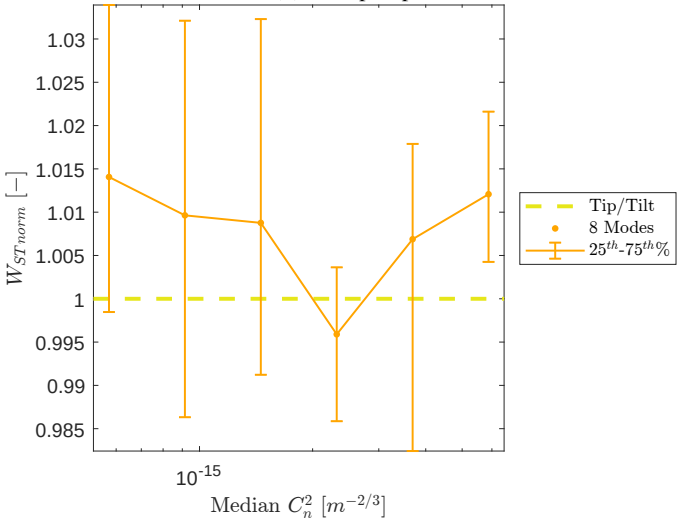

(d) Normalized grouped plot.

Fig. 59: Short-term spot size results for 8 AO modes.

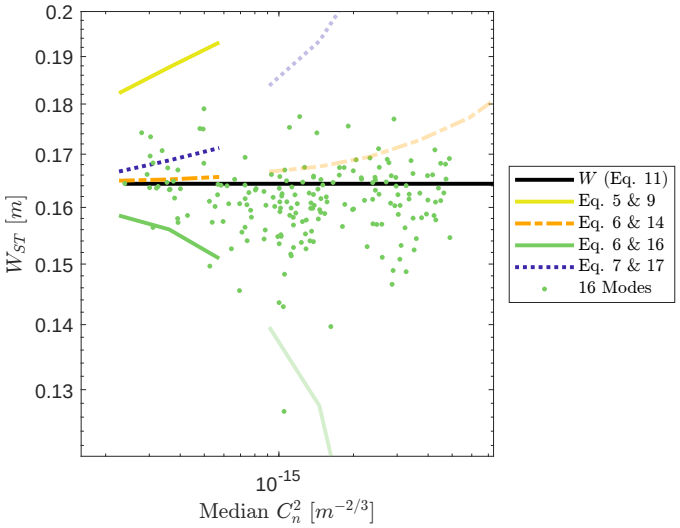

(a) Scatter plot.

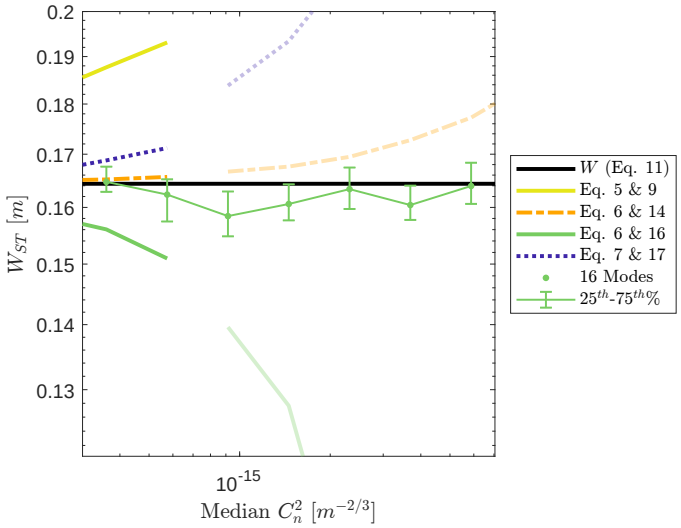

(b) Grouped plot.

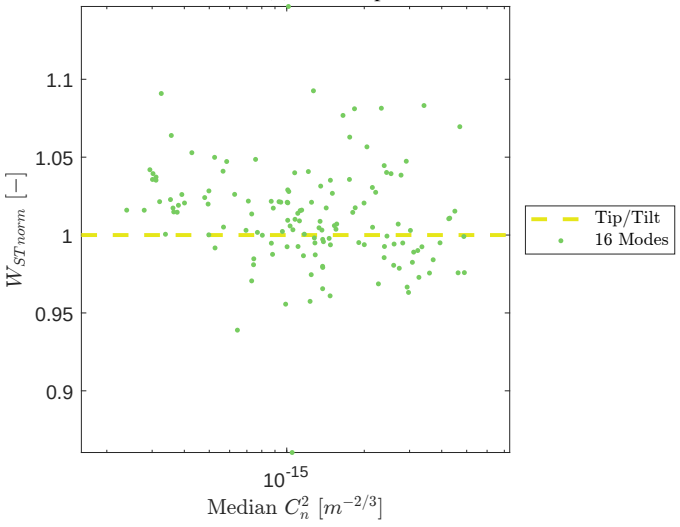

(c) Normalized scatter plot.

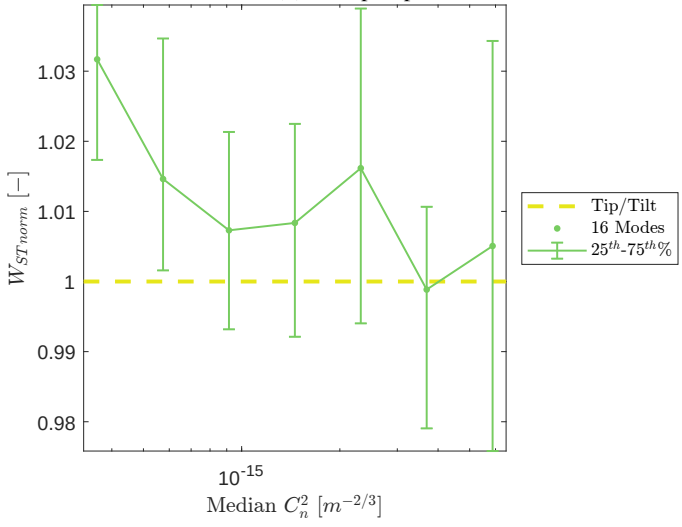

(d) Normalized grouped plot.

Fig. 60: Short-term spot size results for 16 AO modes.

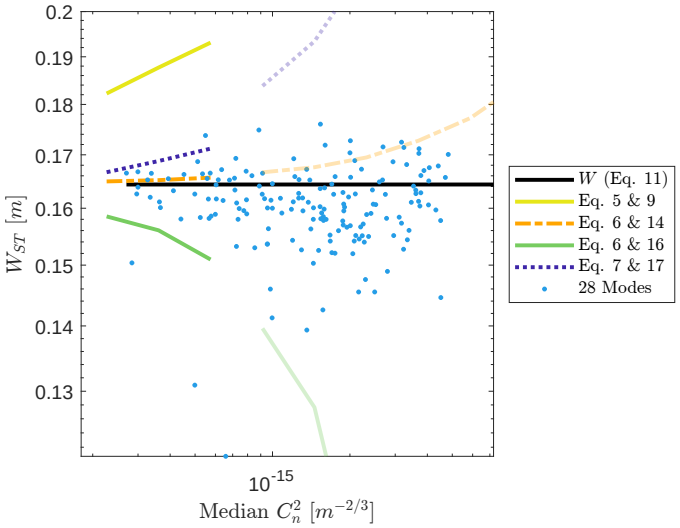

(a) Scatter plot.

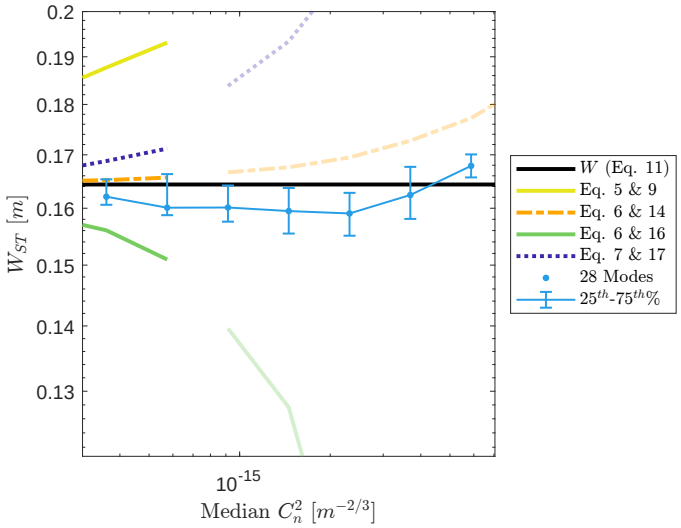

(b) Grouped plot.

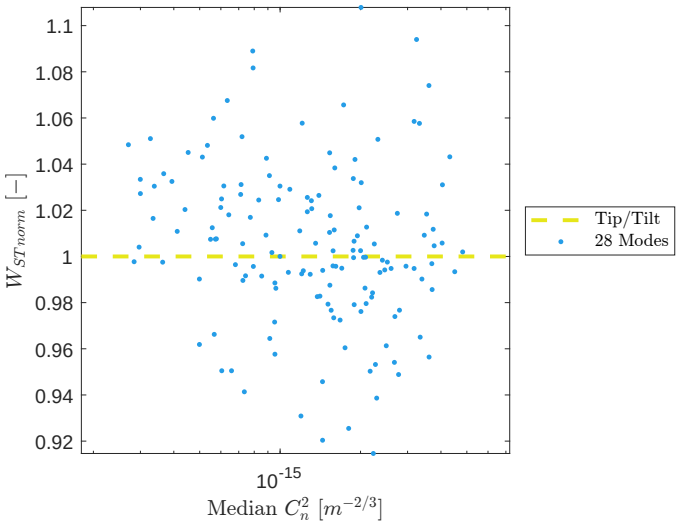

(c) Normalized scatter plot.

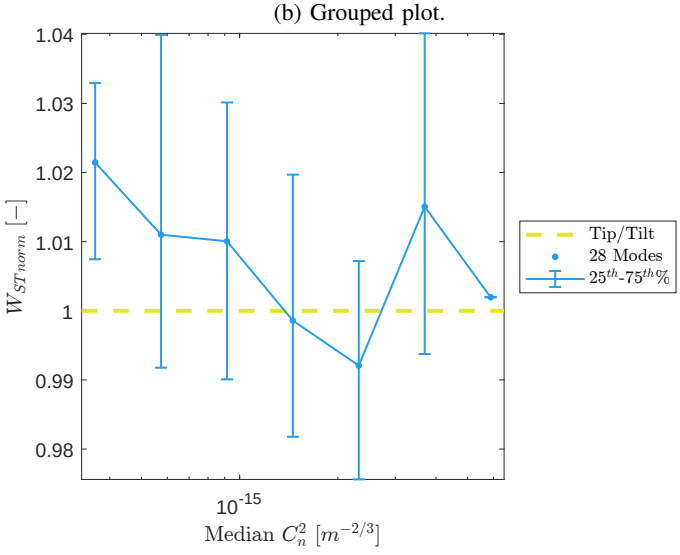

(d) Normalized grouped plot.

Fig. 61: Short-term spot size results for 28 AO modes.

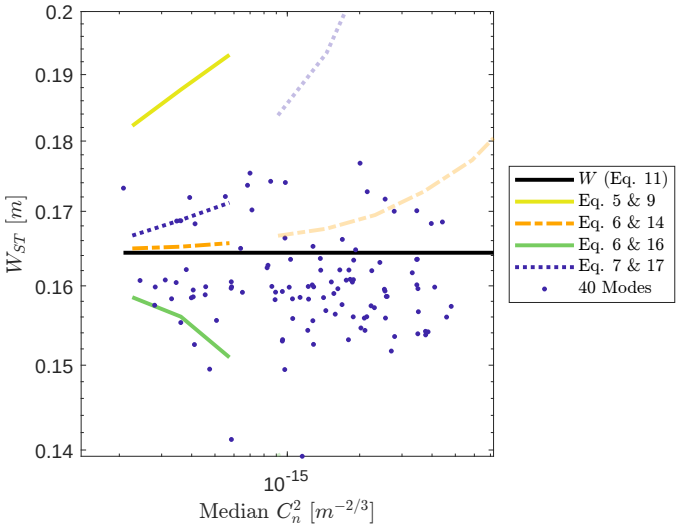

(a) Scatter plot.

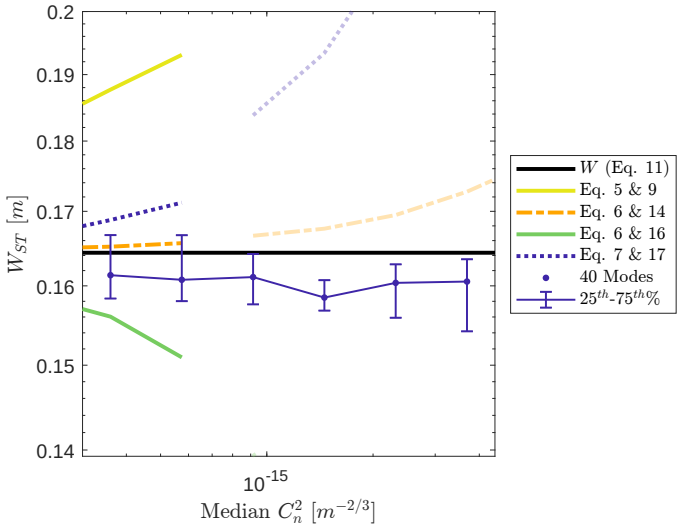

(b) Grouped plot.

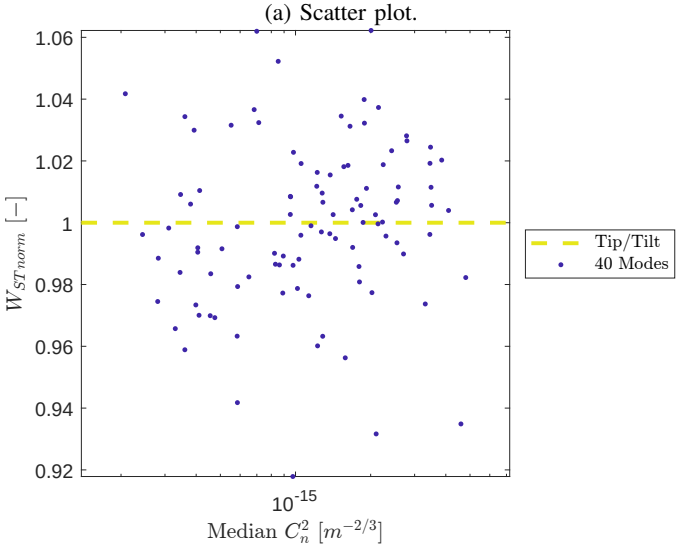

(c) Normalized scatter plot.

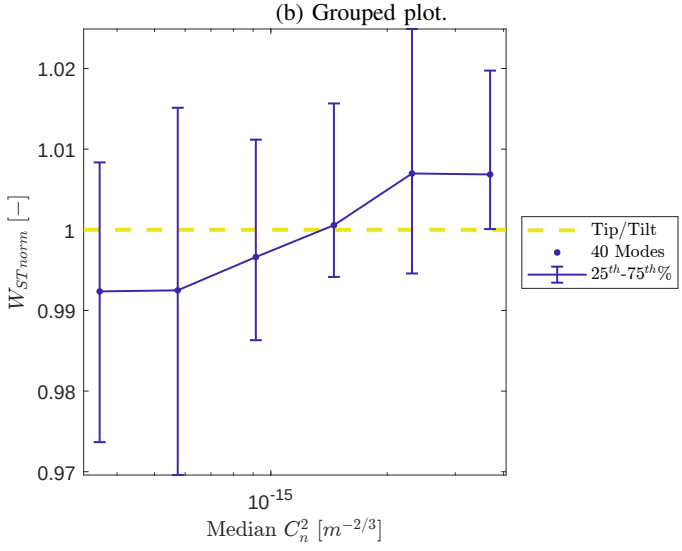

(d) Normalized grouped plot.

Fig. 62: Short-term spot size results for 40 AO modes.

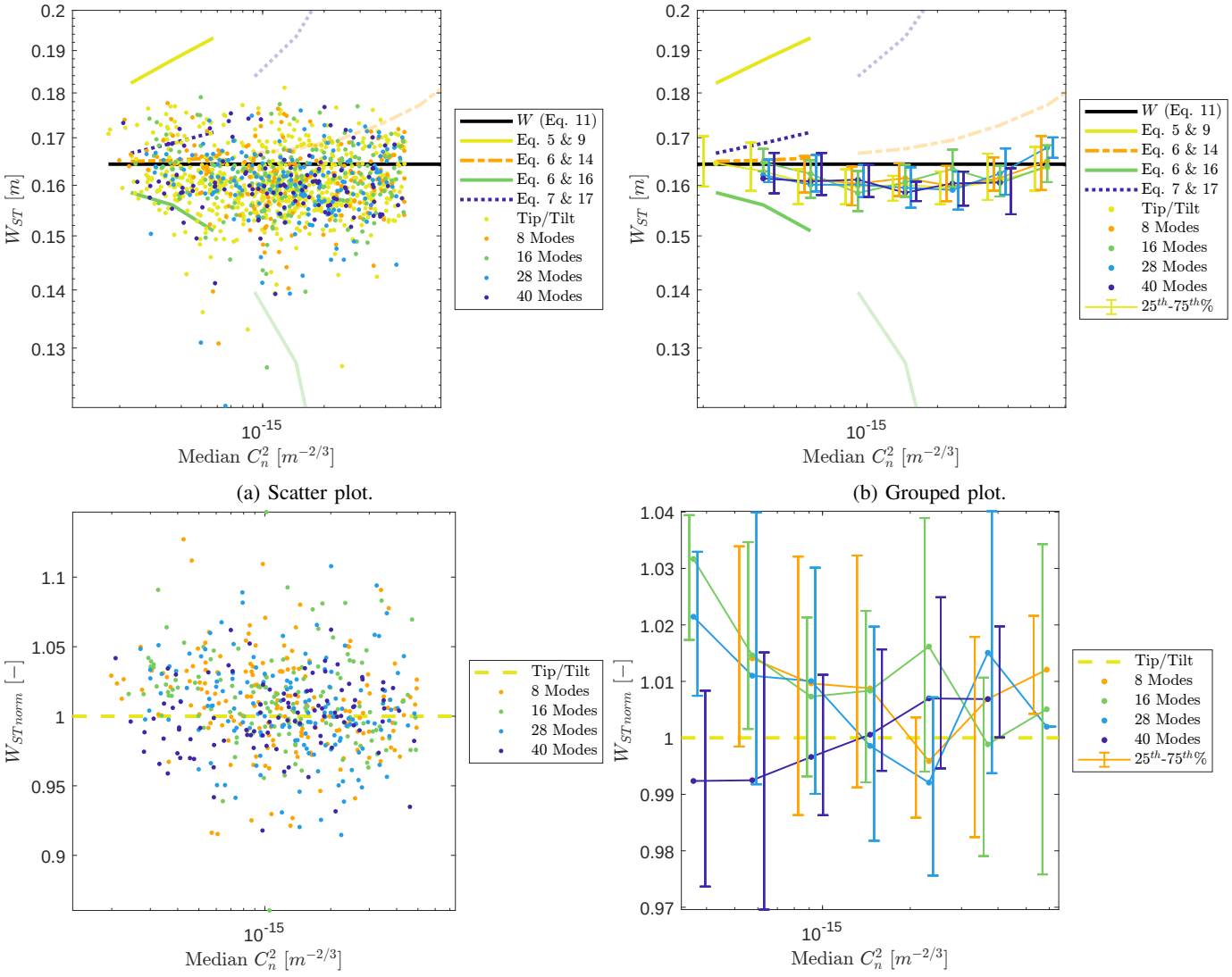

(a) Scatter plot.

(b) Grouped plot.

(c) Normalized scatter plot.

(d) Normalized grouped plot.

Fig. 63: Short-term spot size results for all AO modes.

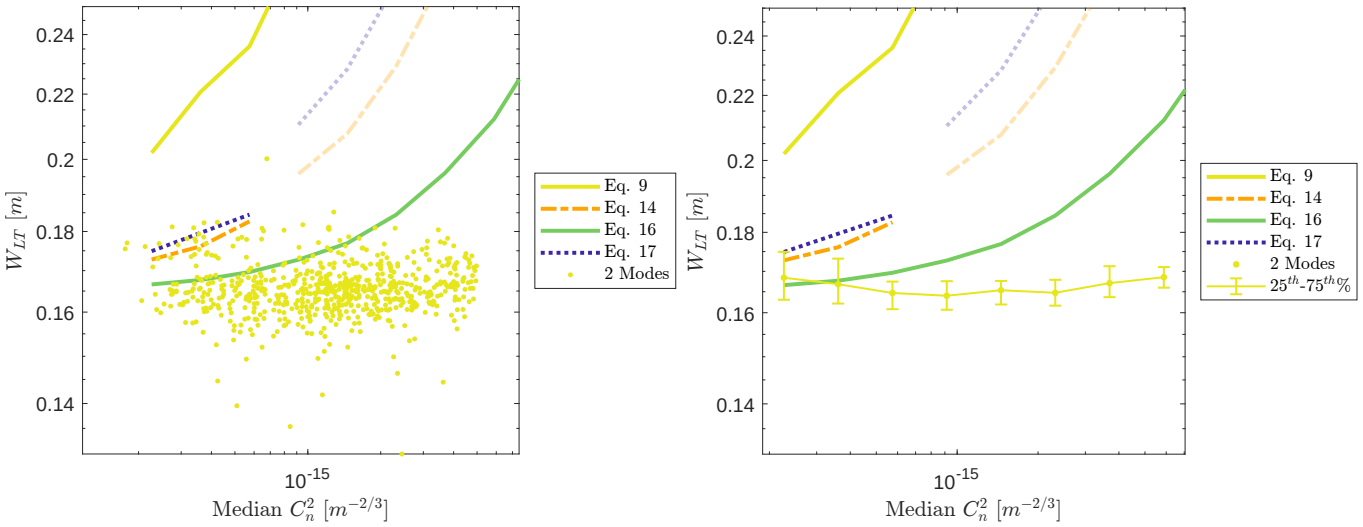

(a) Scatter plot.

(b) Grouped plot.

Fig. 64: Long-term spot size results for tip/tilt pre-correction.

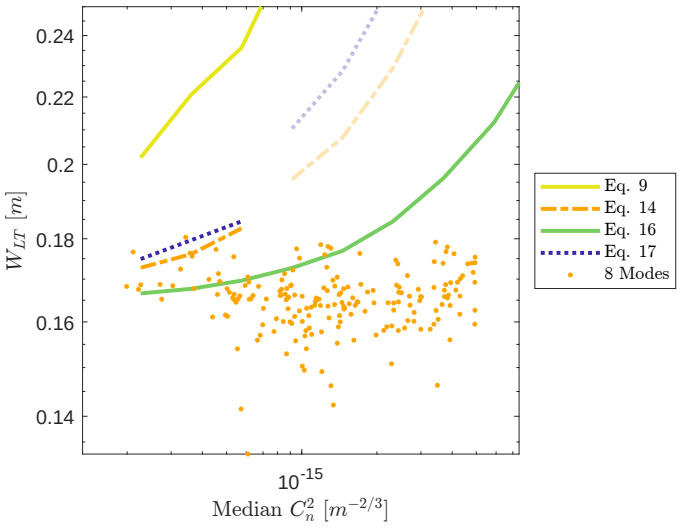

(a) Scatter plot.

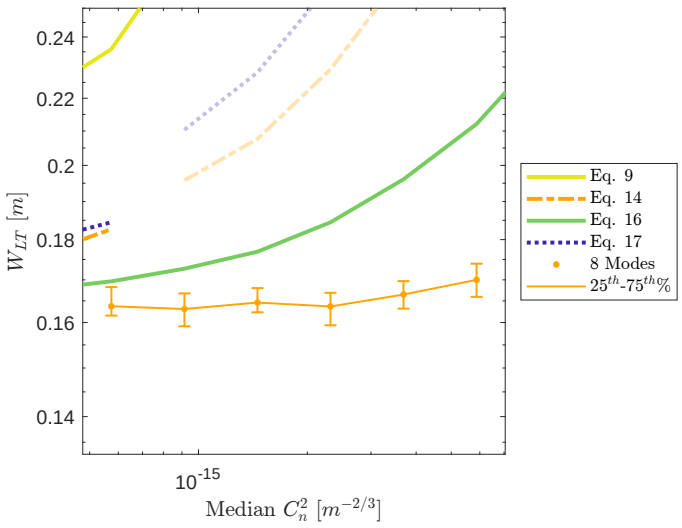

(b) Grouped plot.

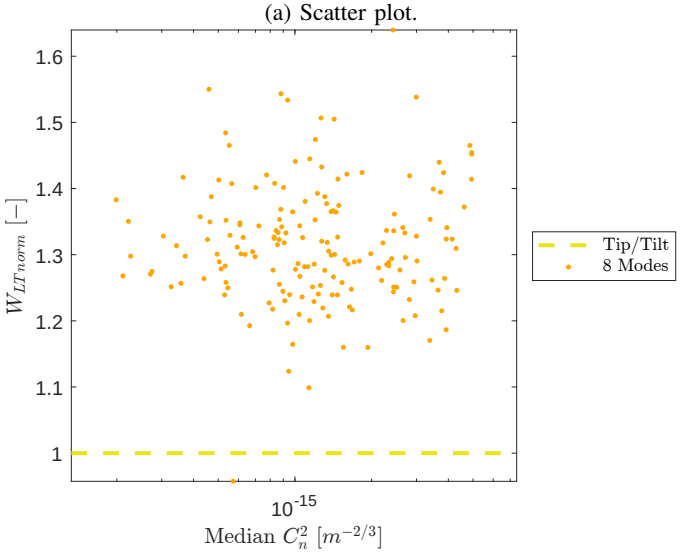

(c) Normalized scatter plot.

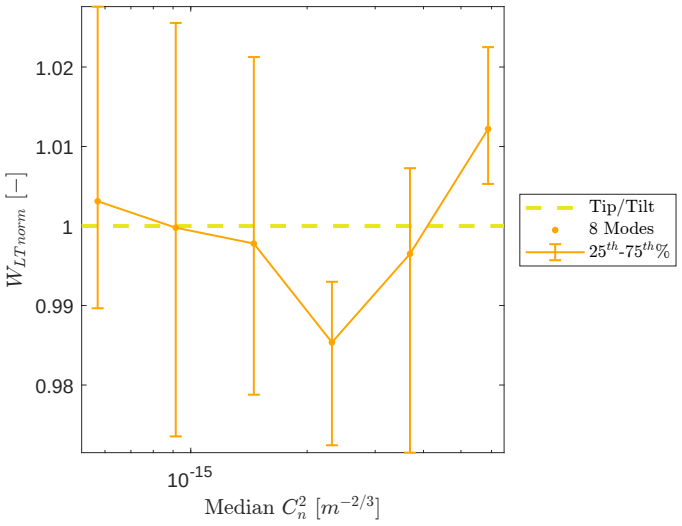

(d) Normalized grouped plot.

Fig. 65: Long-term spot size results for 8 AO modes.

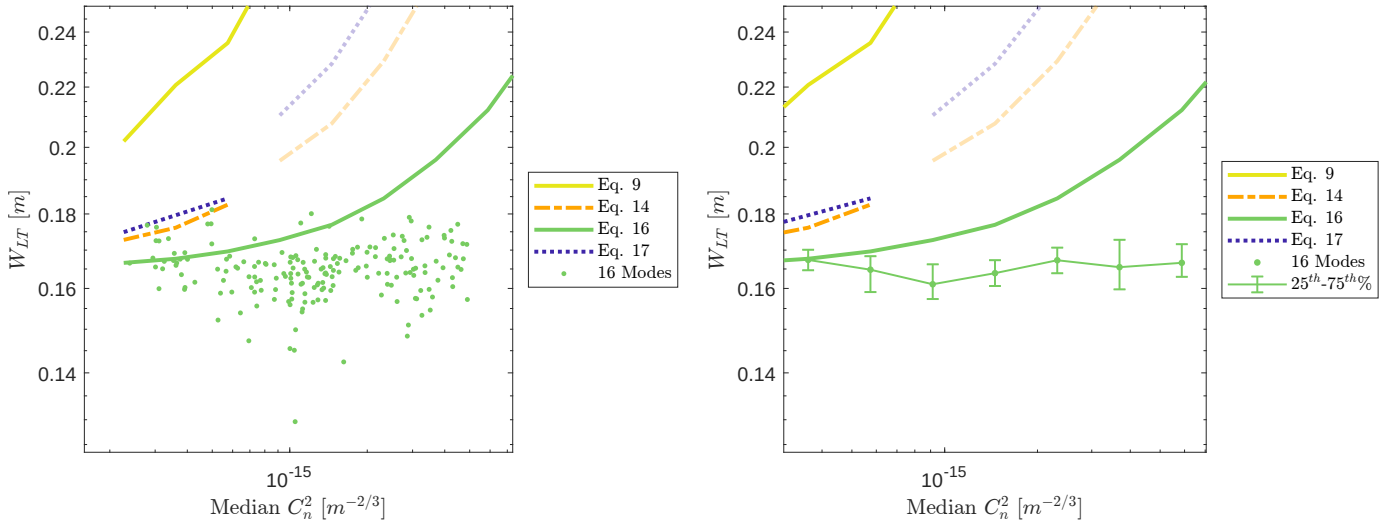

(a) Scatter plot.

(b) Grouped plot.

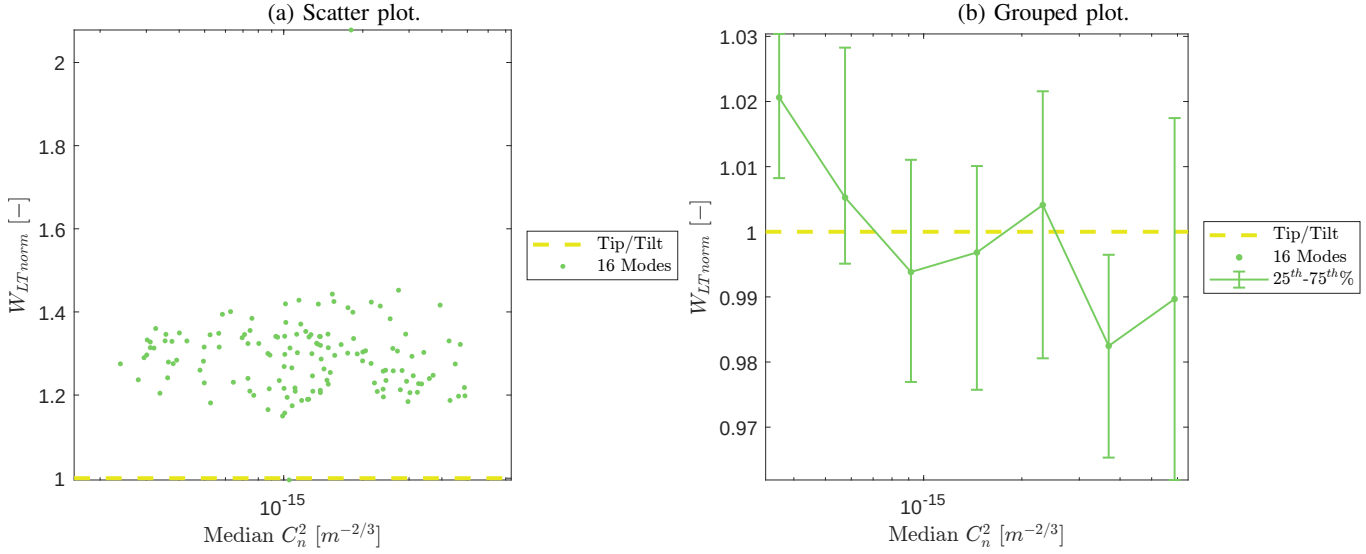

(c) Normalized scatter plot.

(d) Normalized grouped plot.

Fig. 66: Long-term spot size results for 16 AO modes.

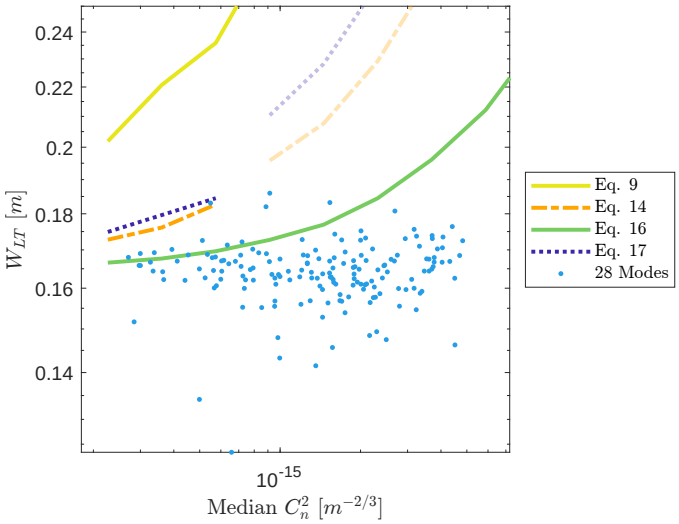

(a) Scatter plot.

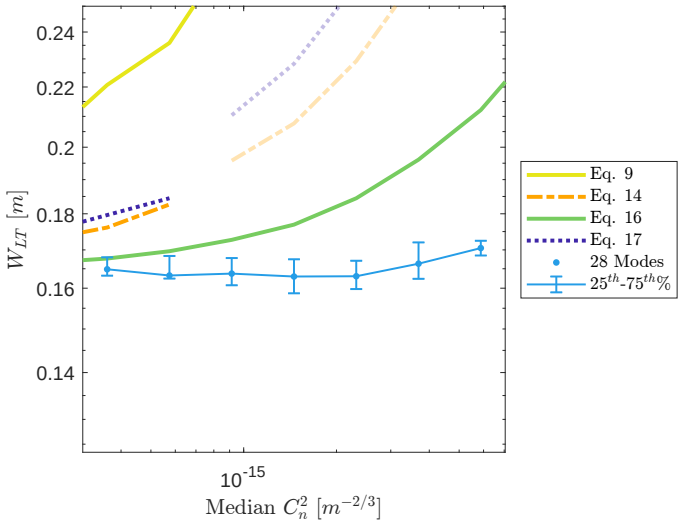

(b) Grouped plot.

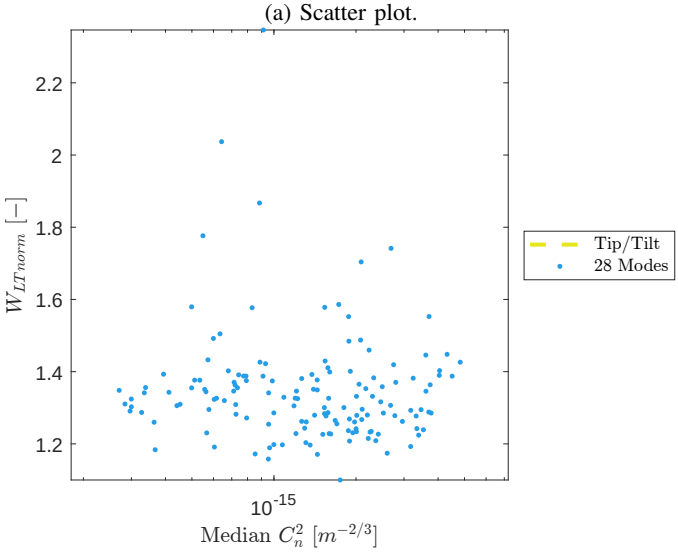

(c) Normalized scatter plot.

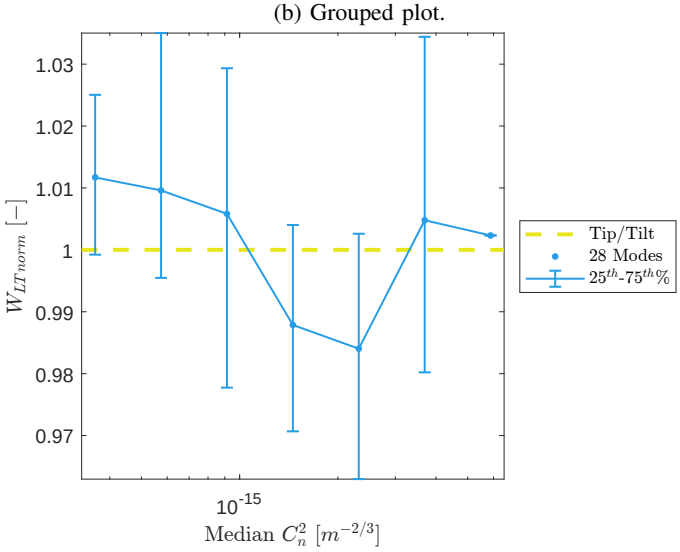

(d) Normalized grouped plot.

Fig. 67: Long-term spot size results for 28 AO modes.

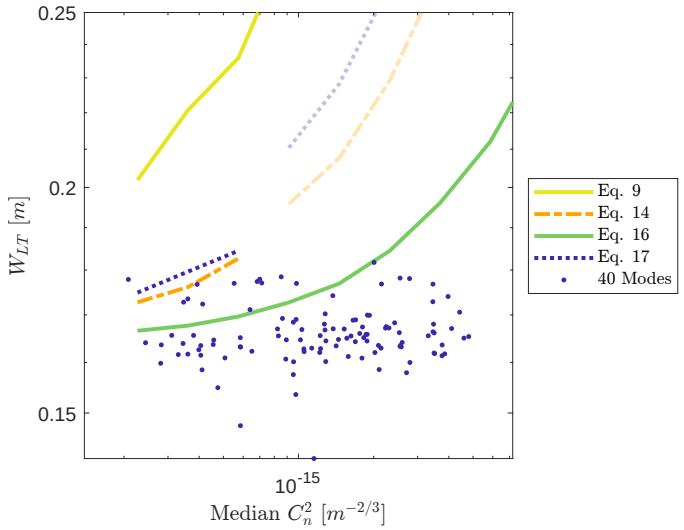

(a) Scatter plot.

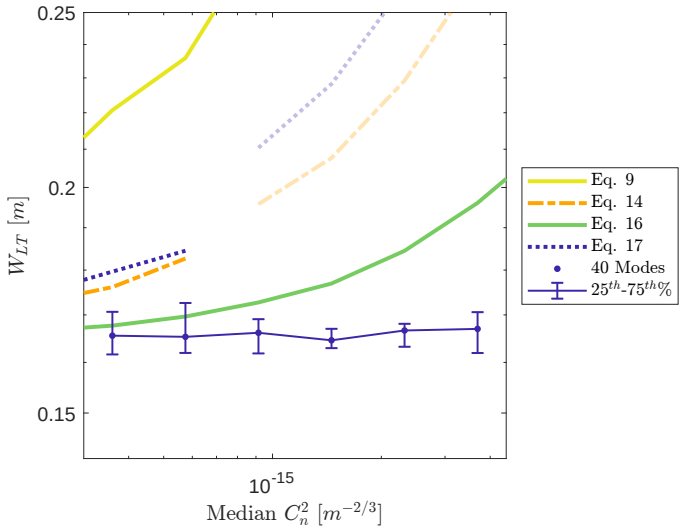

(b) Grouped plot.

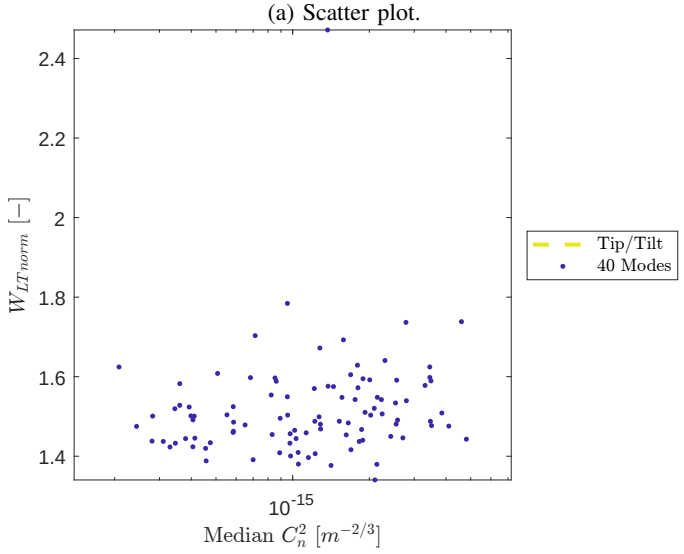

(c) Normalized scatter plot.

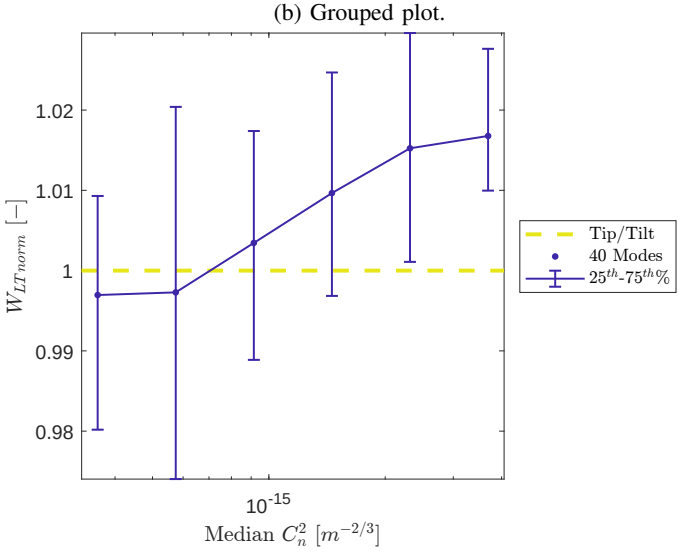

(d) Normalized grouped plot.

Fig. 68: Long-term spot size results for 40 AO modes.

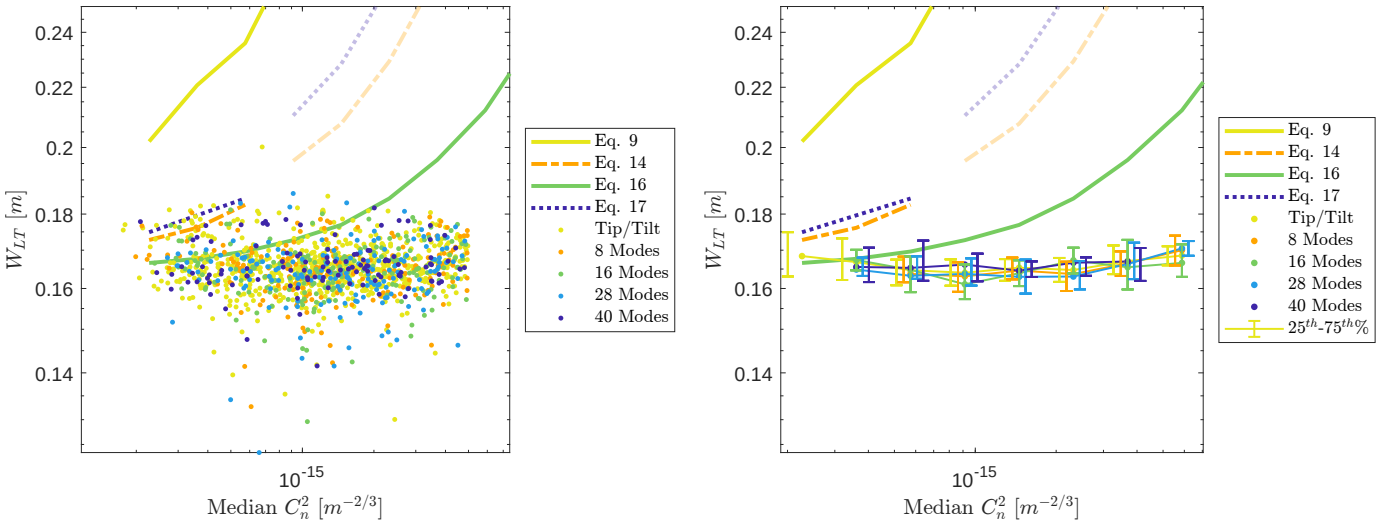

(a) Scatter plot.

(b) Grouped plot.

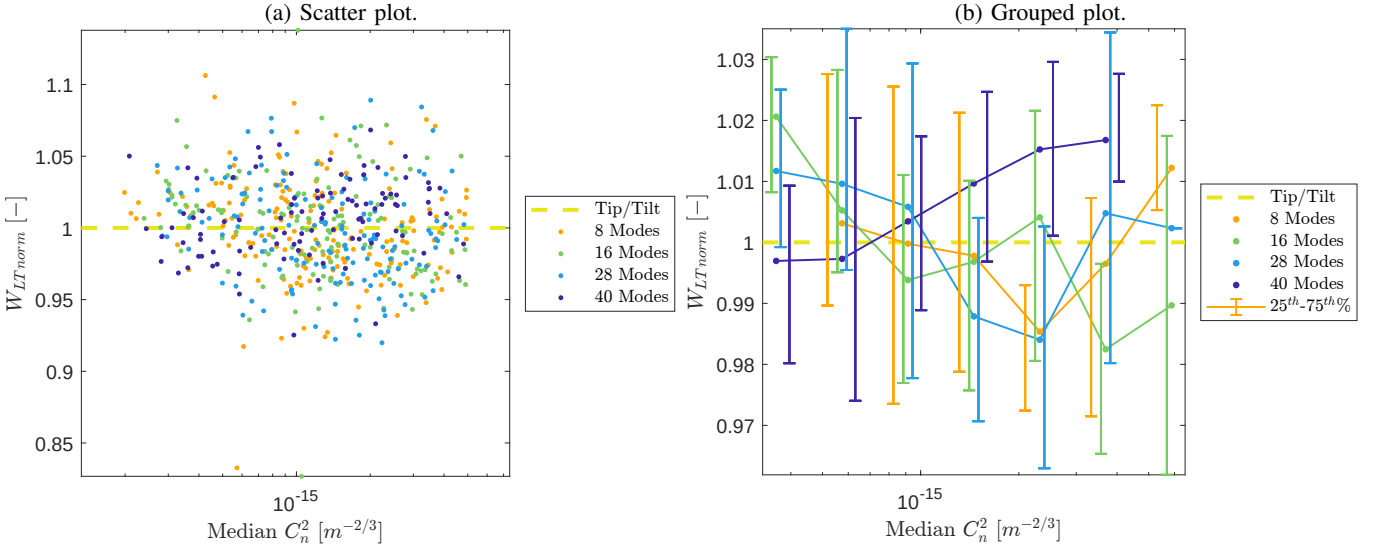

(c) Normalized scatter plot.

(d) Normalized grouped plot.

Fig. 69: Long-term spot size results for all AO modes.

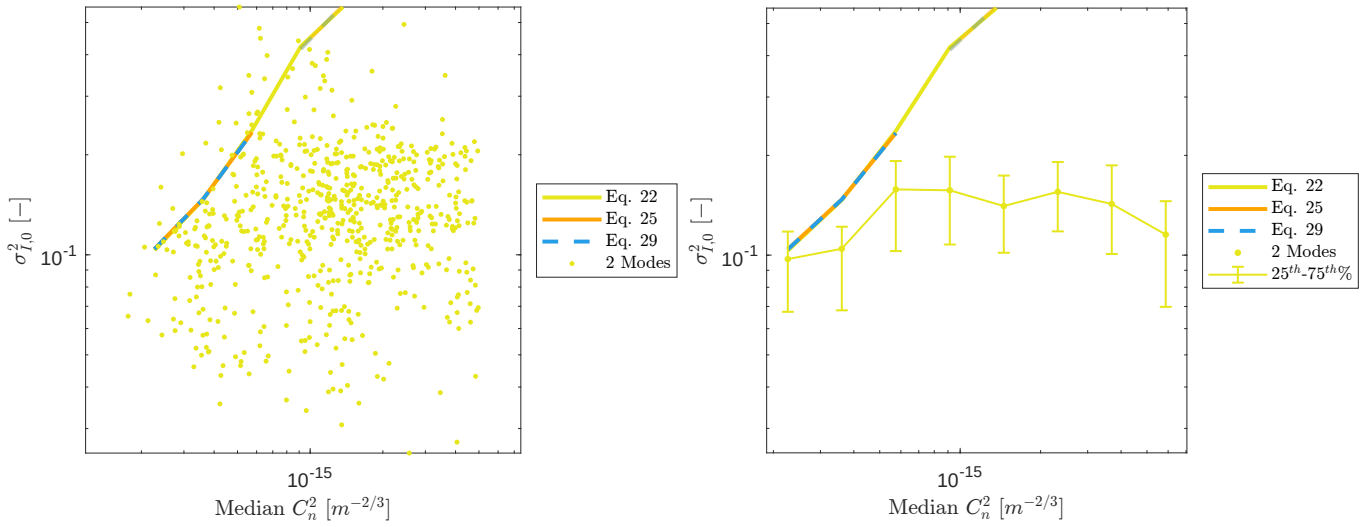

(a) Scatter plot.

(b) Grouped plot.

Fig. 70: Longitudinal scintillation results for tip/tilt pre-correction.

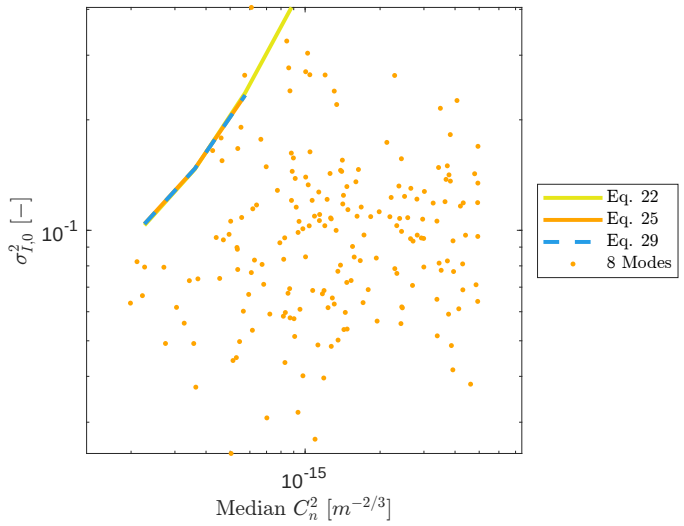

(a) Scatter plot.

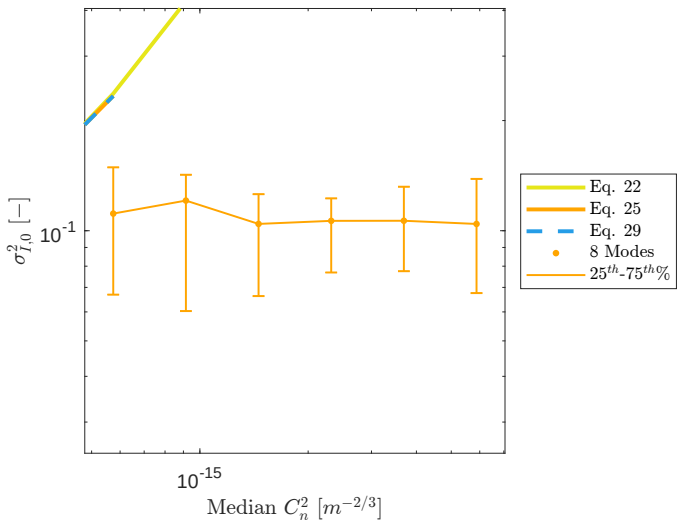

(b) Grouped plot.

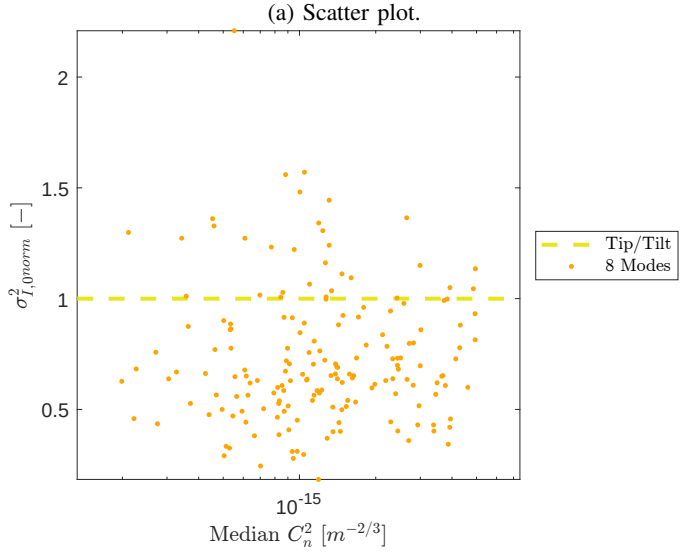

(c) Normalized scatter plot.

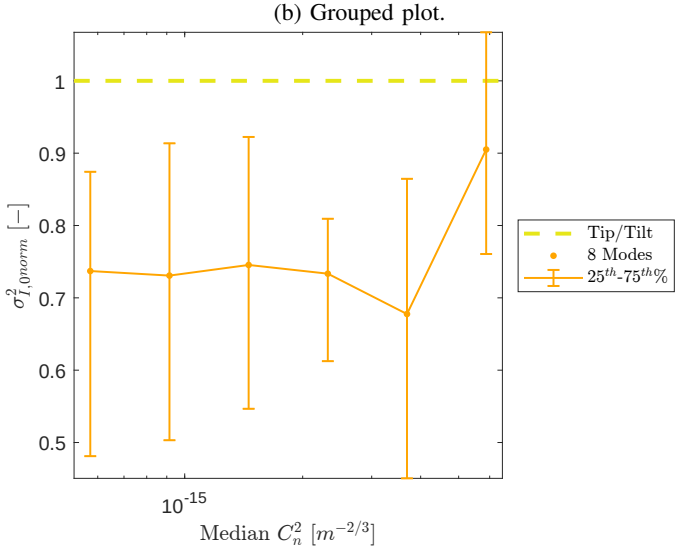

(d) Normalized grouped plot.

Fig. 71: Longitudinal scintillation results for 8 AO modes.

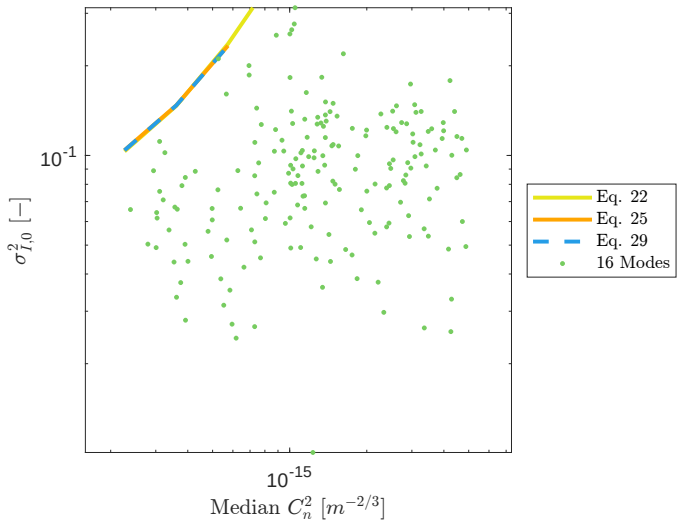

(a) Scatter plot.

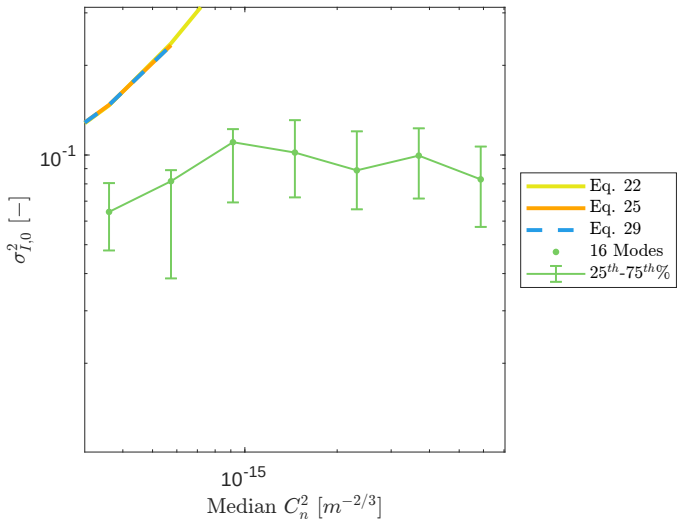

(b) Grouped plot.

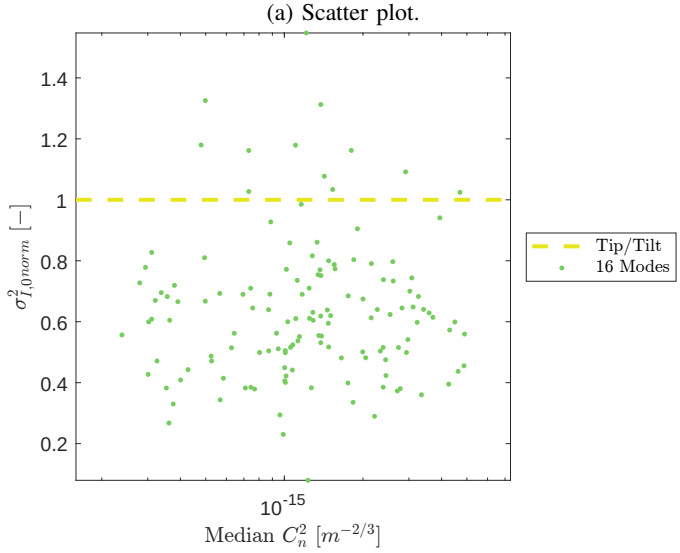

(c) Normalized scatter plot.

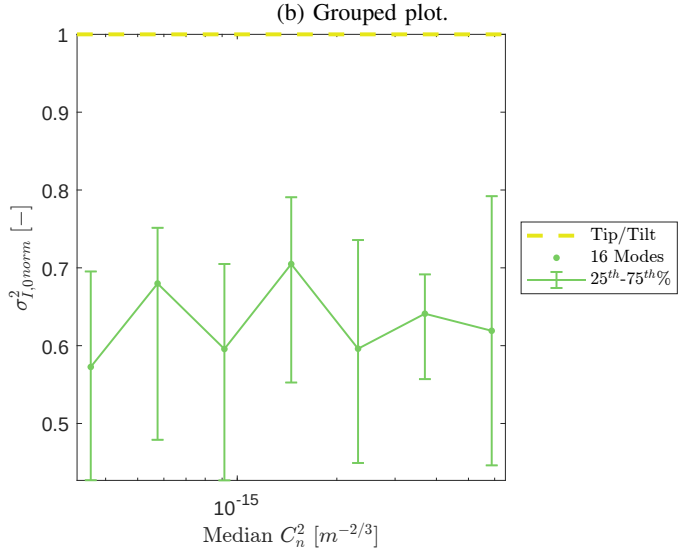

(d) Normalized grouped plot.

Fig. 72: Longitudinal scintillation results for 16 AO modes.

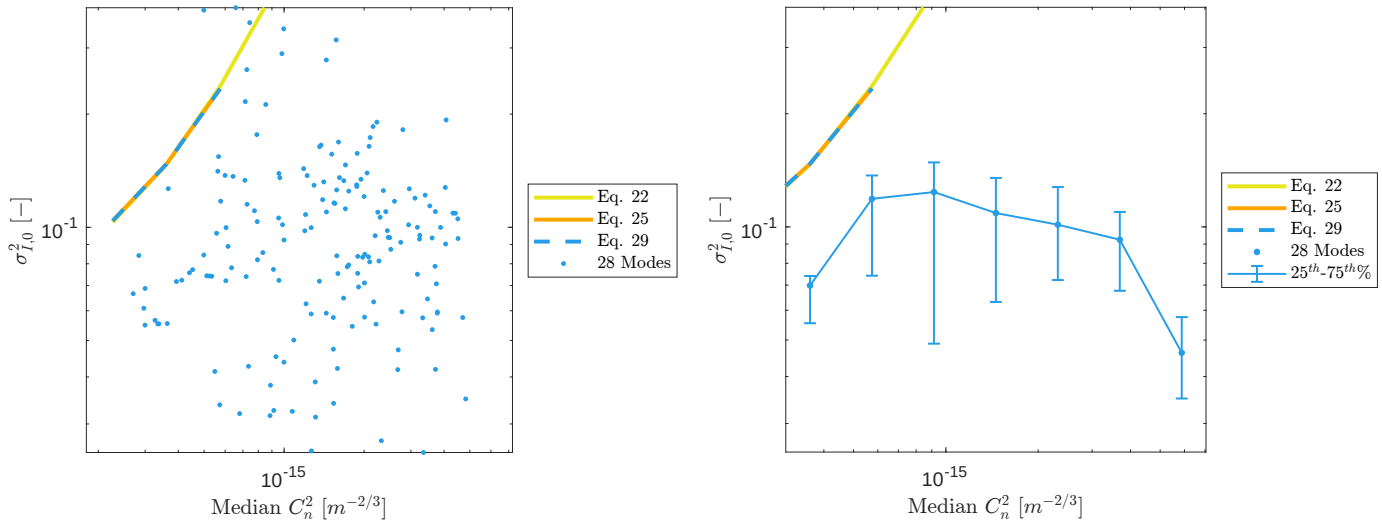

(a) Scatter plot.

(b) Grouped plot.

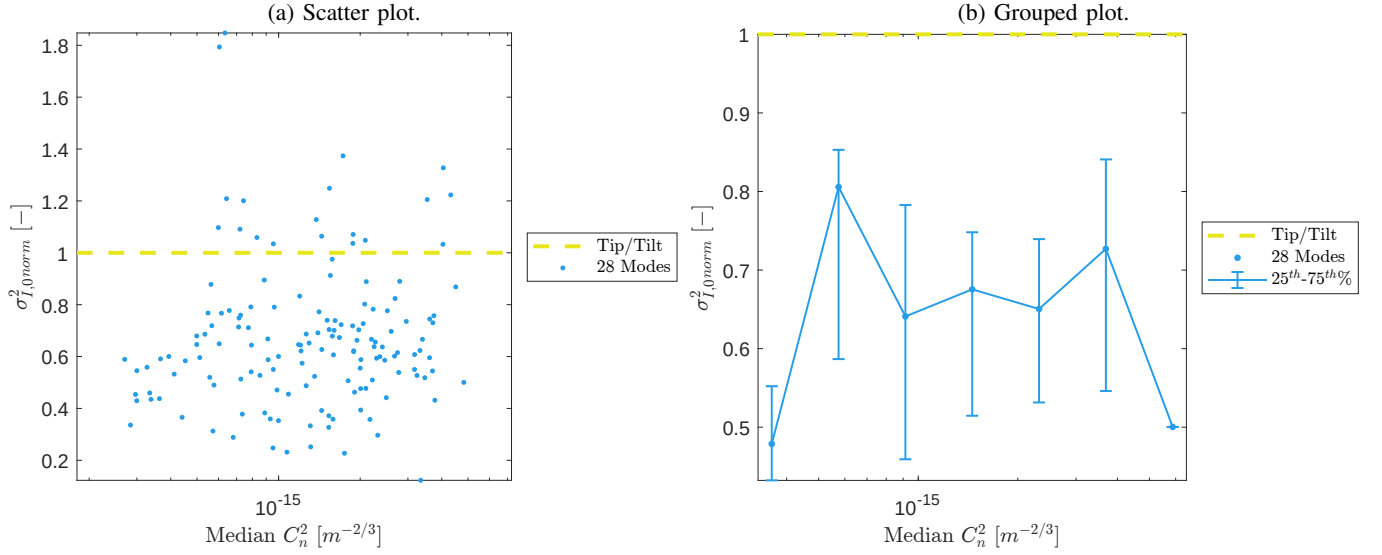

(c) Normalized scatter plot.

(d) Normalized grouped plot.

Fig. 73: Longitudinal scintillation results for 28 AO modes.

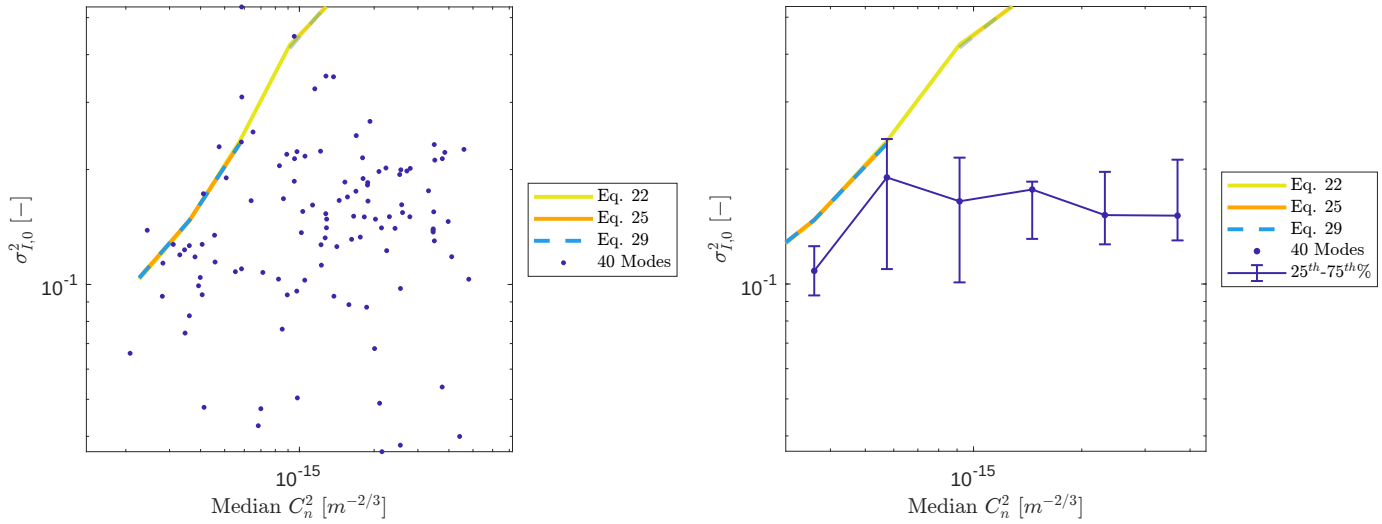

(a) Scatter plot.

(b) Grouped plot.

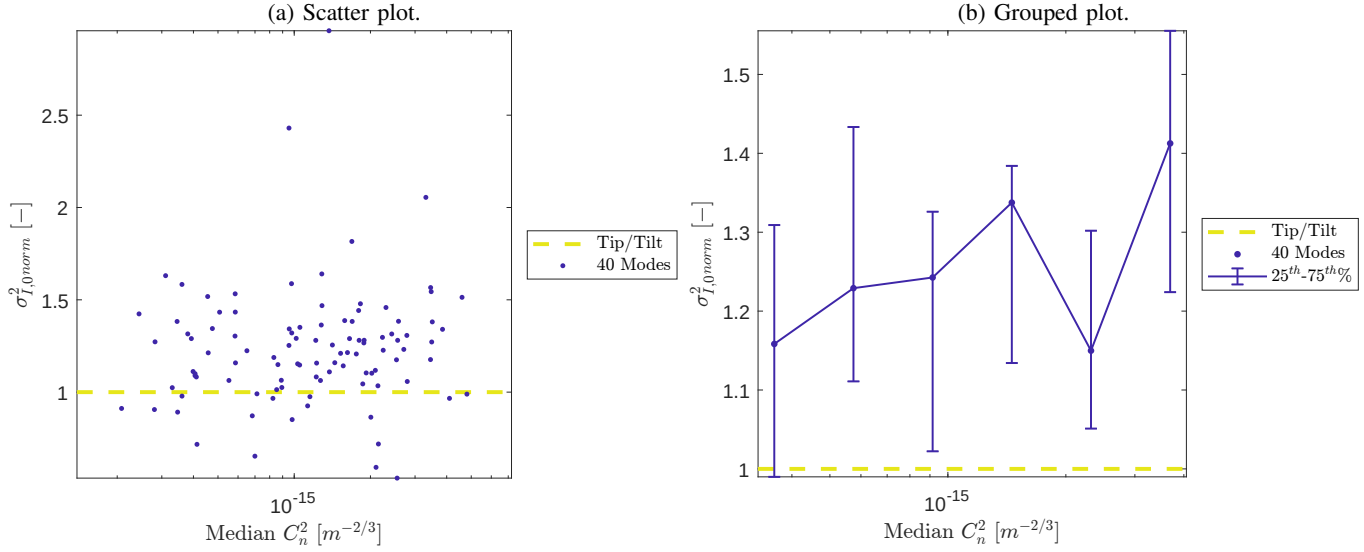

(c) Normalized scatter plot.

(d) Normalized grouped plot.

Fig. 74: Longitudinal scintillation results for 40 AO modes.

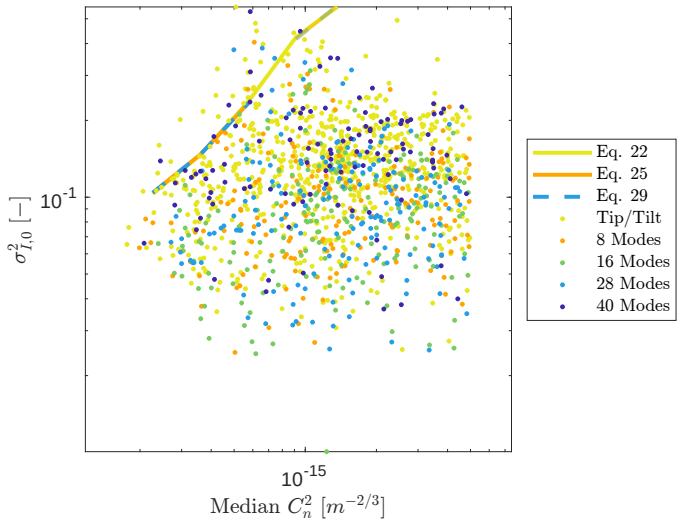

(a) Scatter plot.

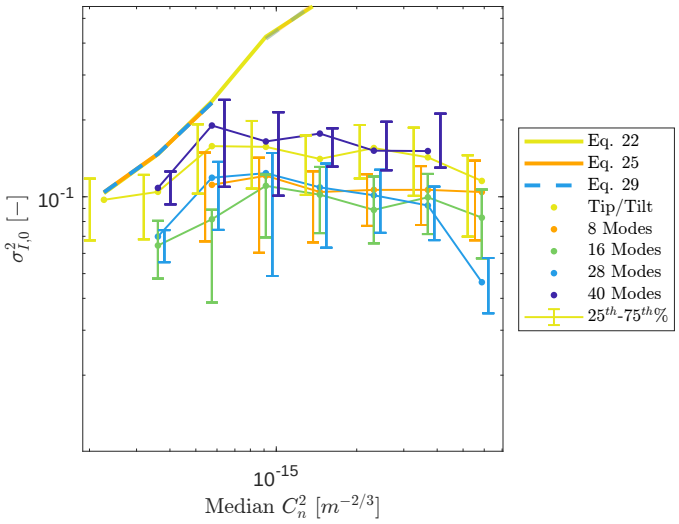

(b) Grouped plot.

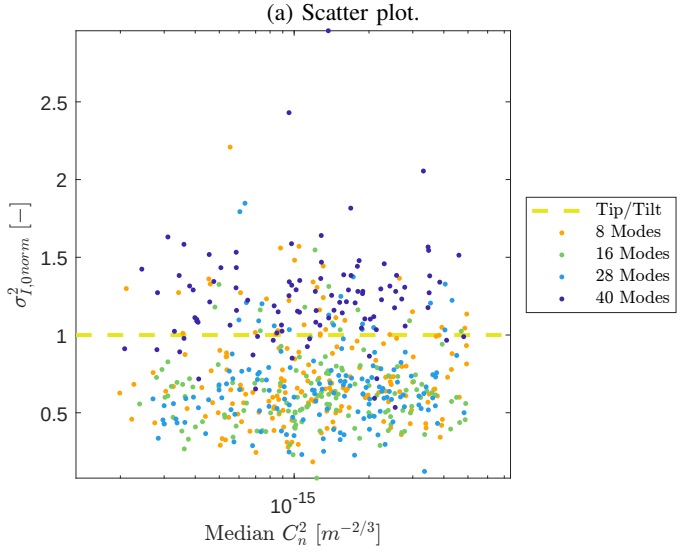

(c) Normalized scatter plot.

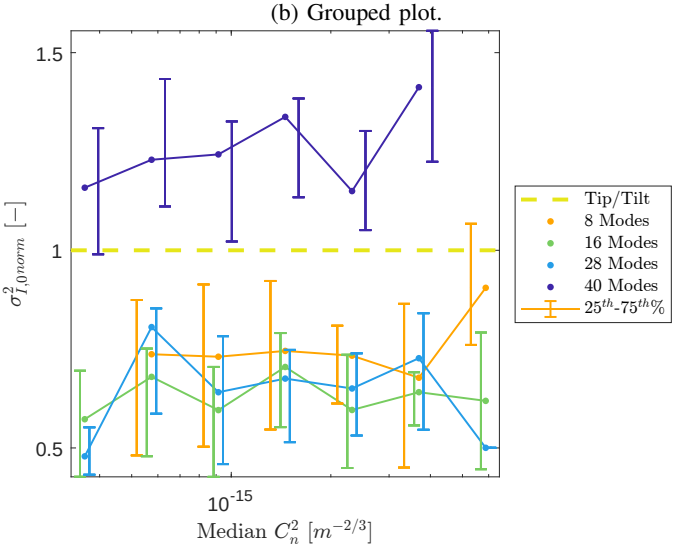

(d) Normalized grouped plot.

Fig. 75: Longitudinal scintillation results for all AO modes.

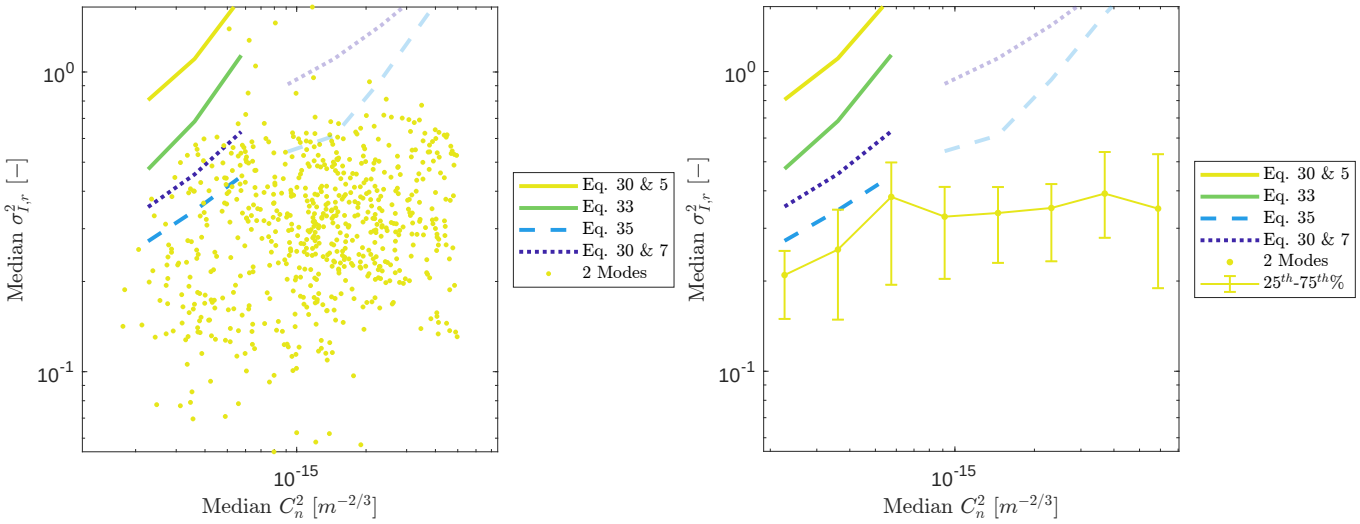

(a) Scatter plot.

(b) Grouped plot.

Fig. 76: Radial scintillation results for tip/tilt pre-correction.

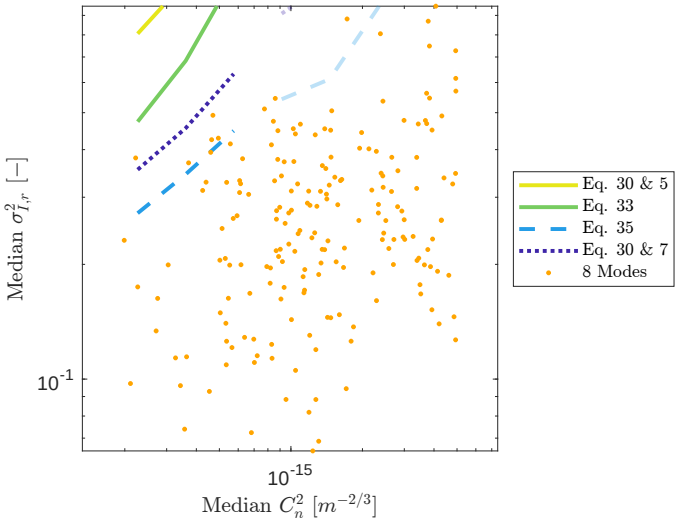

(a) Scatter plot.

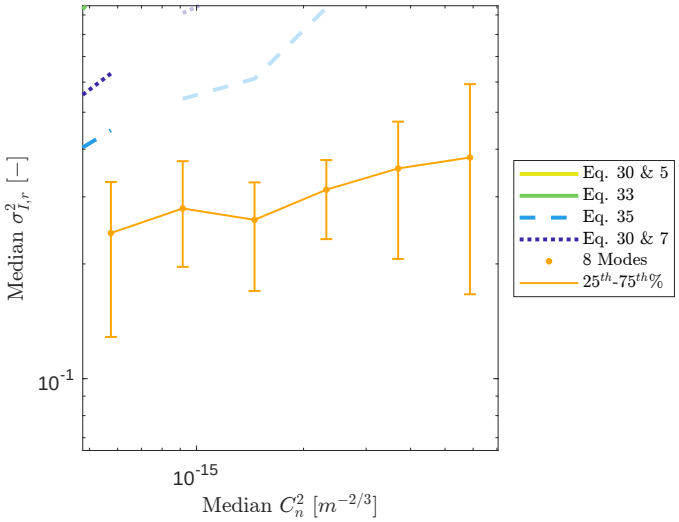

(b) Grouped plot.

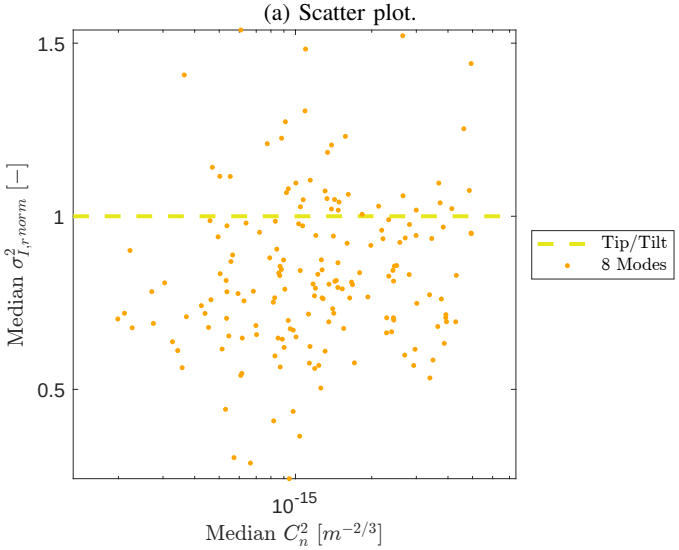

(c) Normalized scatter plot.

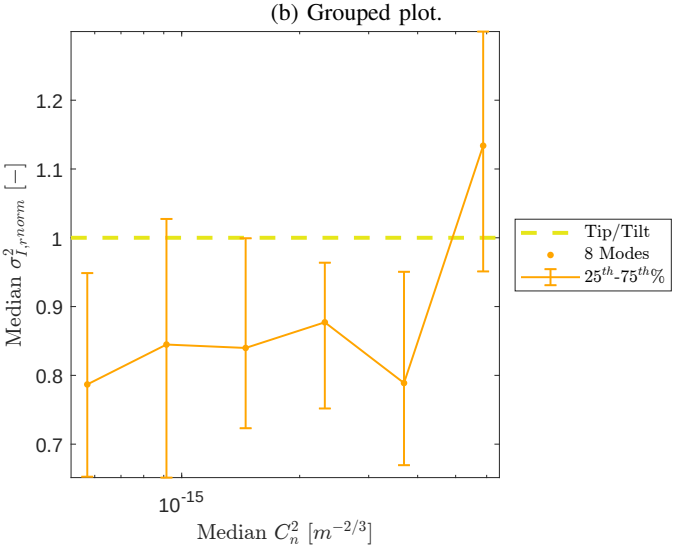

(d) Normalized grouped plot.

Fig. 77: Radial scintillation results for 8 AO modes.

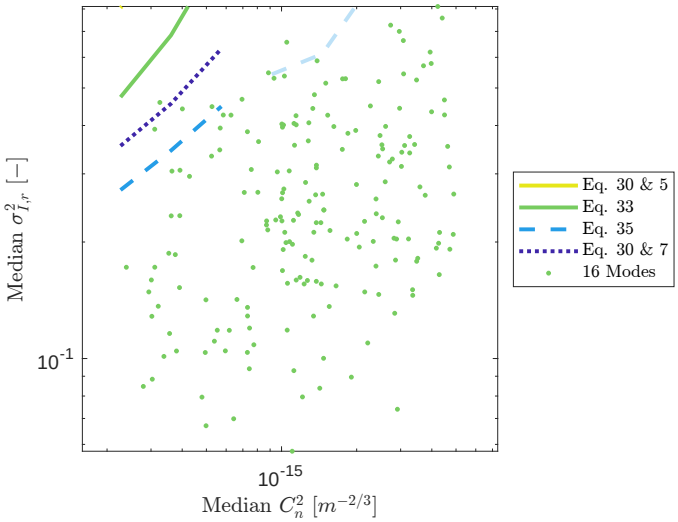

(a) Scatter plot.

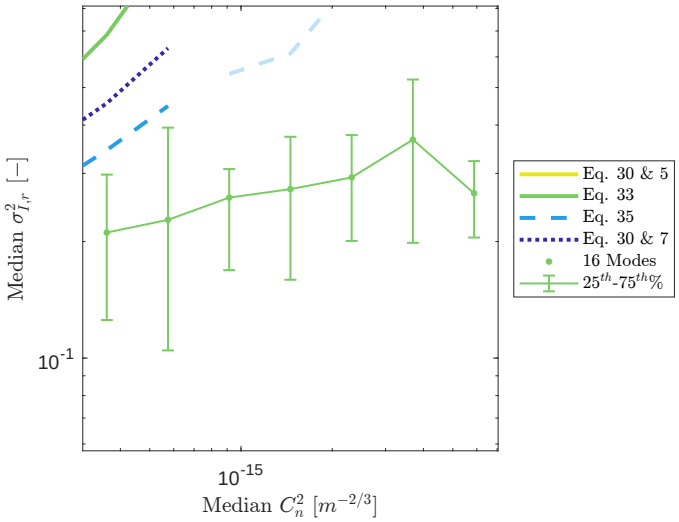

(b) Grouped plot.

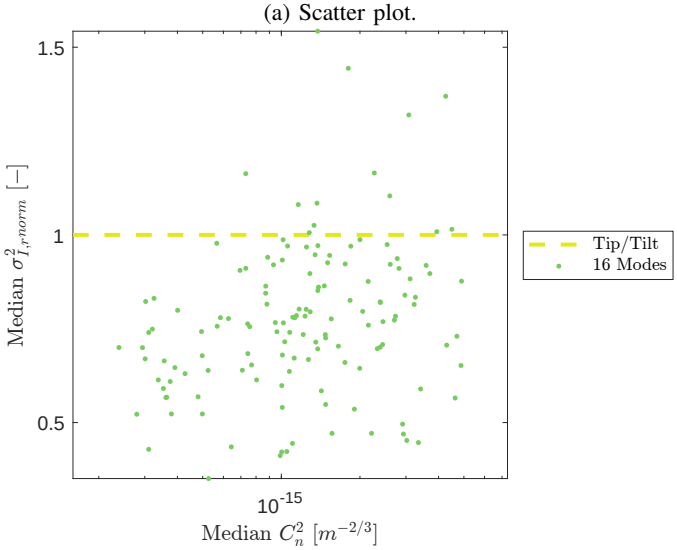

(c) Normalized scatter plot.

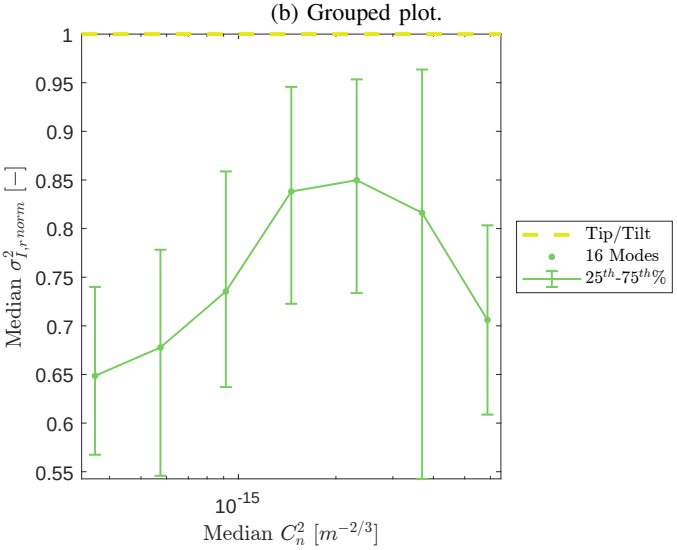

(d) Normalized grouped plot.

Fig. 78: Radial scintillation results for 16 AO modes.

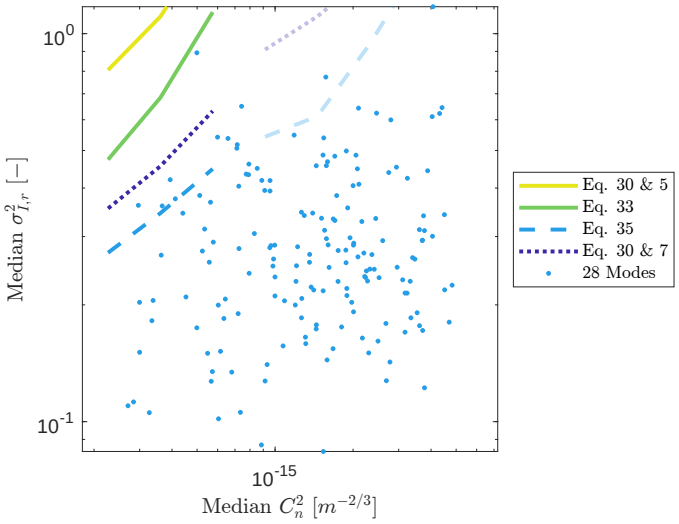

(a) Scatter plot.

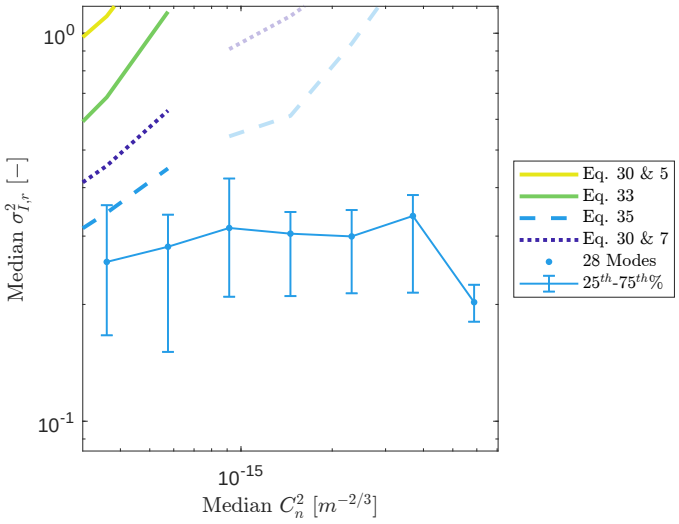

(b) Grouped plot.

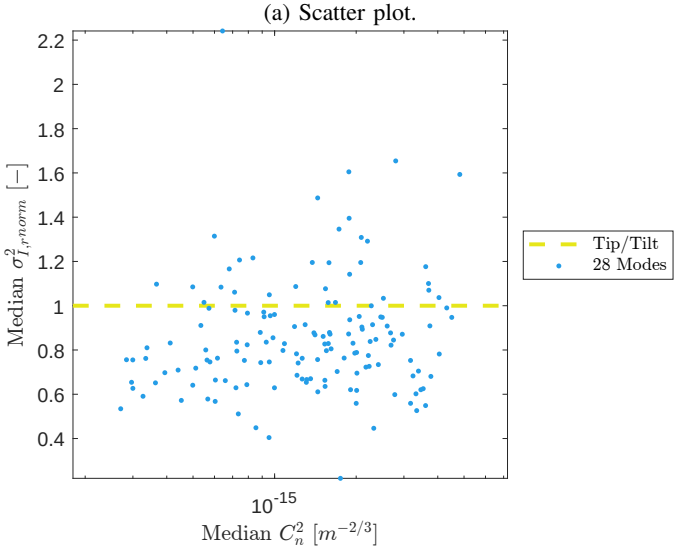

(c) Normalized scatter plot.

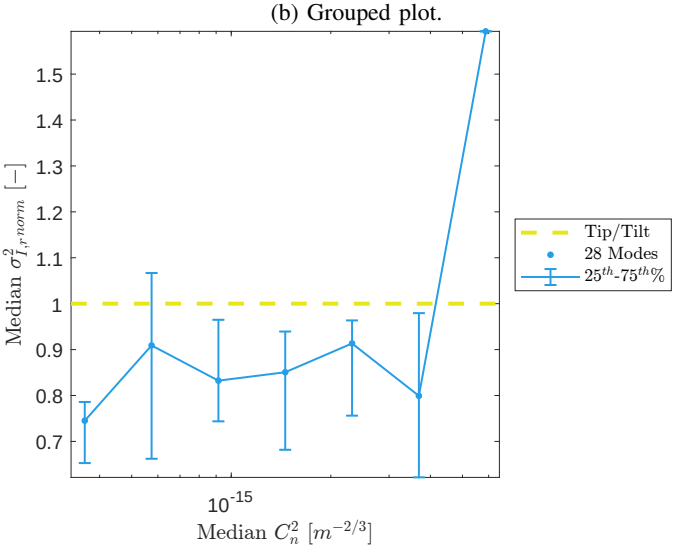

(d) Normalized grouped plot.

Fig. 79: Radial scintillation results for 28 AO modes.

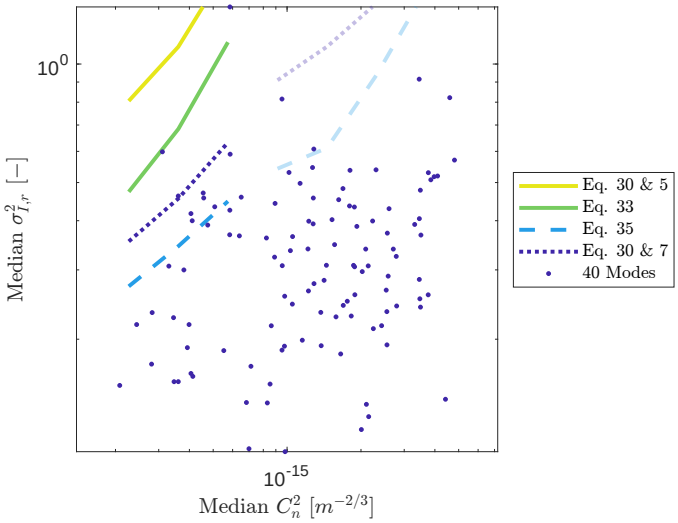

(a) Scatter plot.

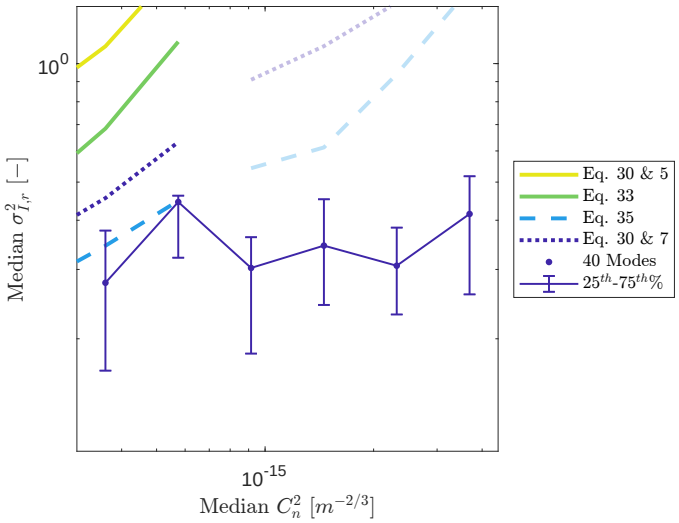

(b) Grouped plot.

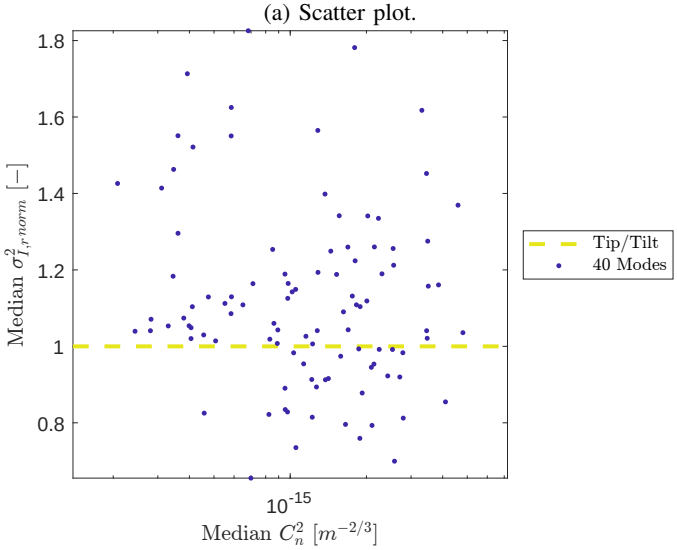

(c) Normalized scatter plot.

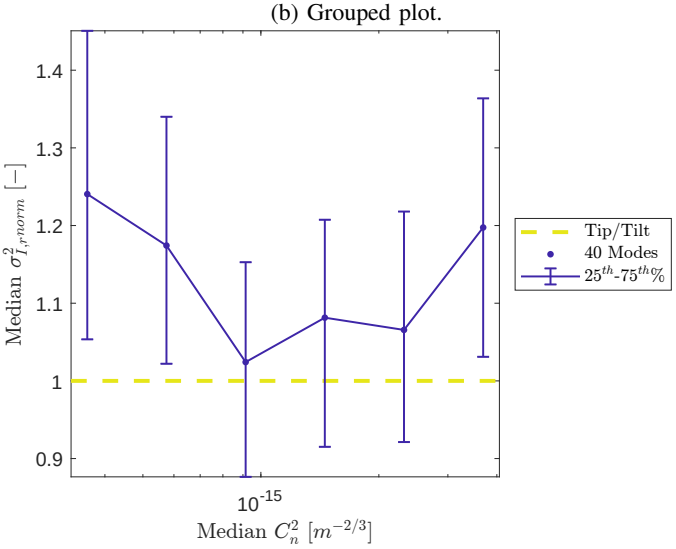

(d) Normalized grouped plot.

Fig. 80: Radial scintillation results for 40 AO modes.

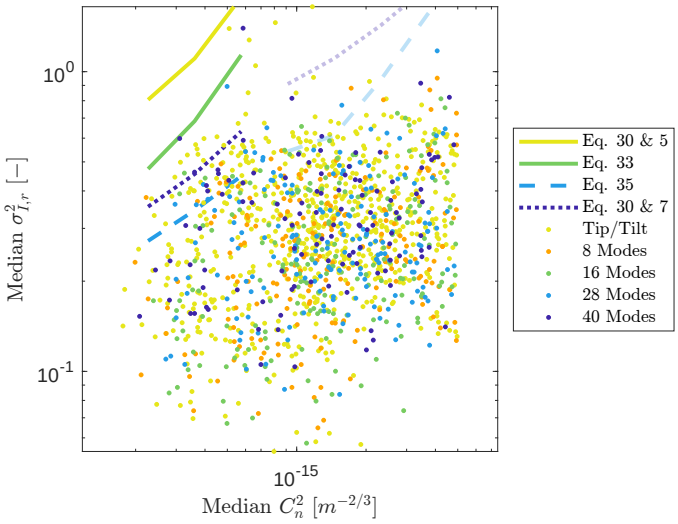

(a) Scatter plot.

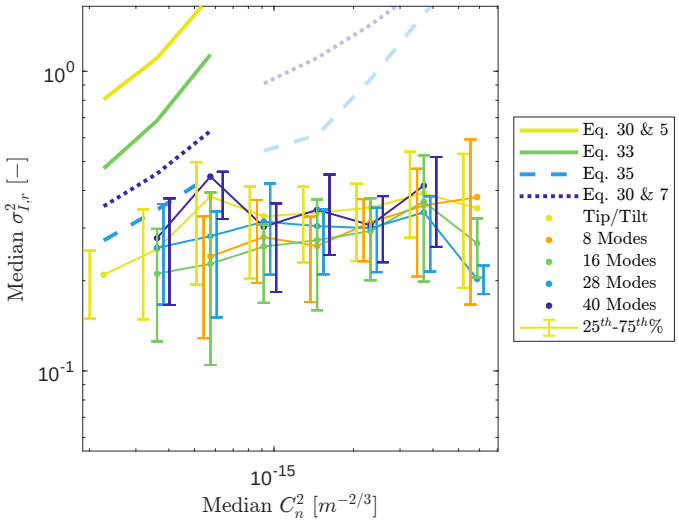

(b) Grouped plot.

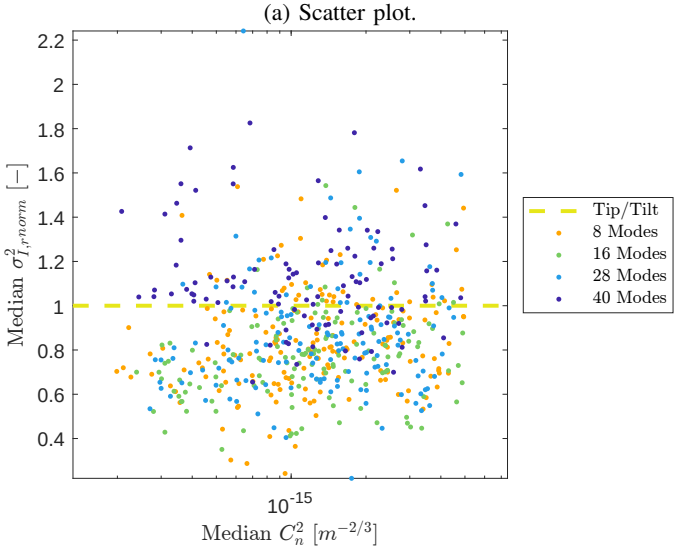

(c) Normalized scatter plot.

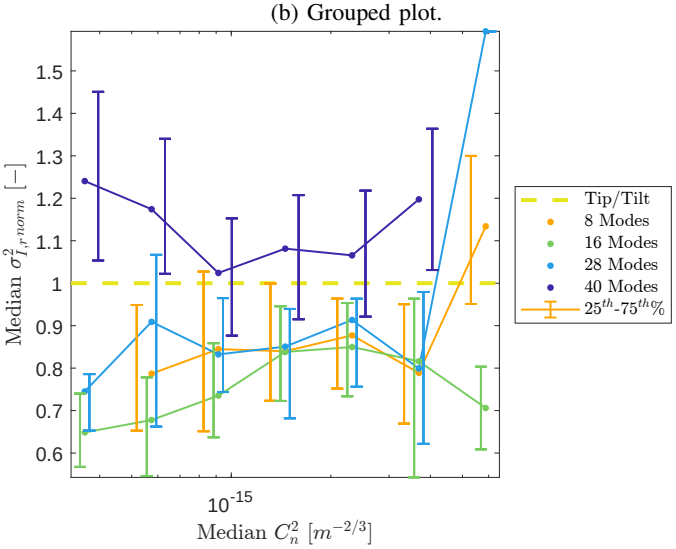

(d) Normalized grouped plot.

Fig. 81: Radial scintillation results for all AO modes.

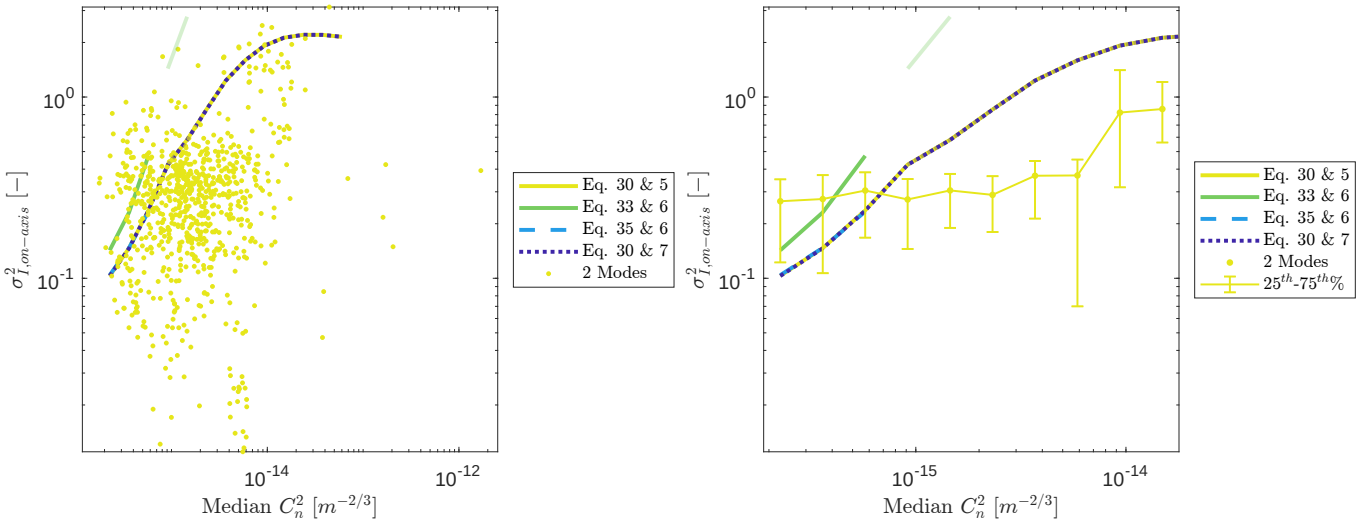

(a) Scatter plot.

(b) Grouped plot.

Fig. 82: On-axis scintillation results for tip/tilt pre-correction.

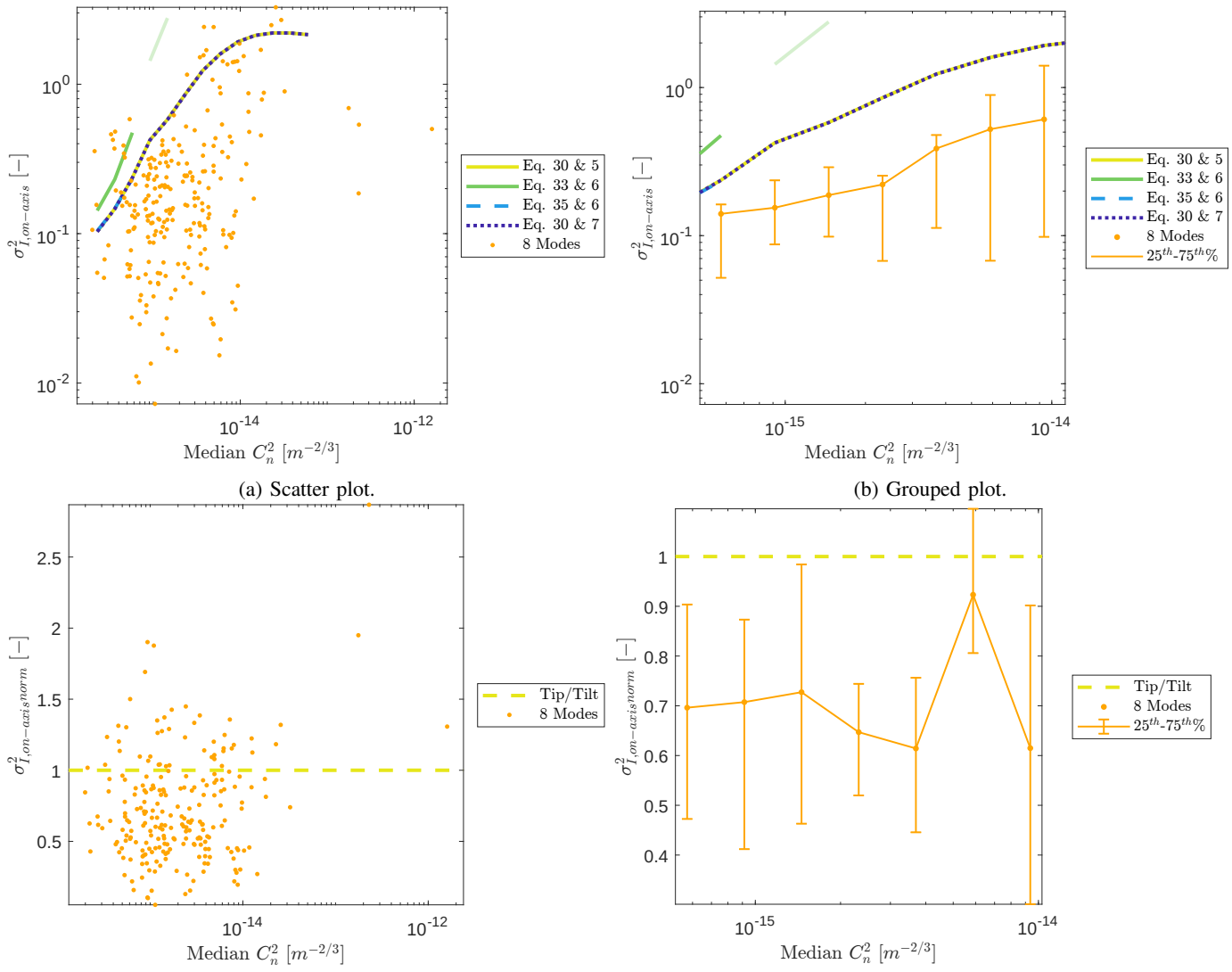

(a) Scatter plot.

(b) Grouped plot.

(c) Normalized scatter plot.

(d) Normalized grouped plot.

Fig. 83: On-axis scintillation results for 8 AO modes.

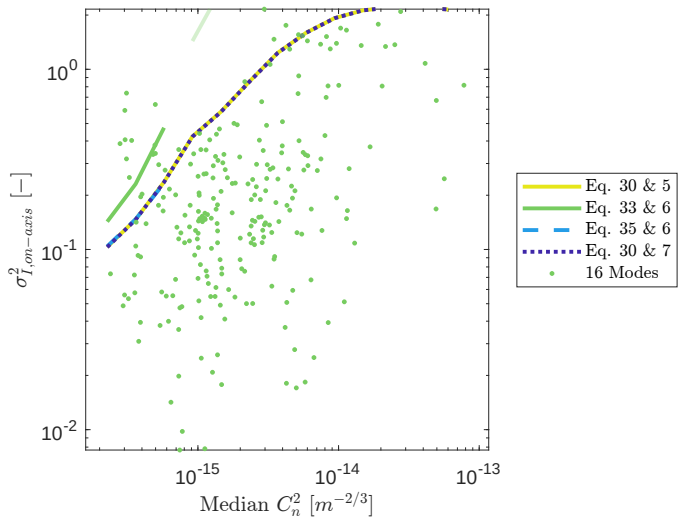

(a) Scatter plot.

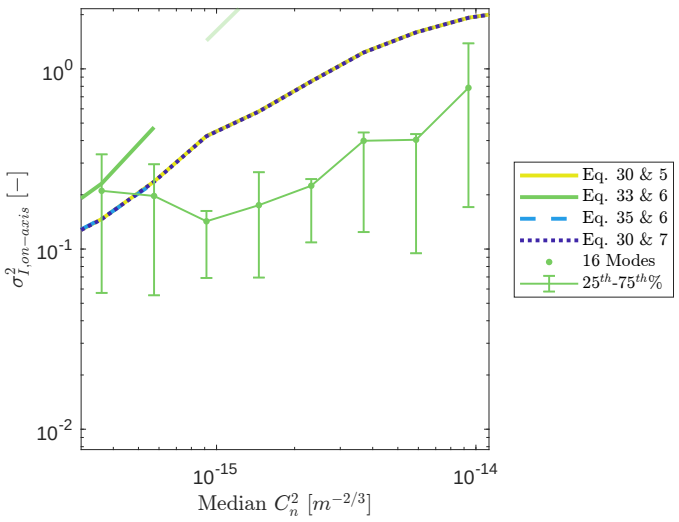

(b) Grouped plot.

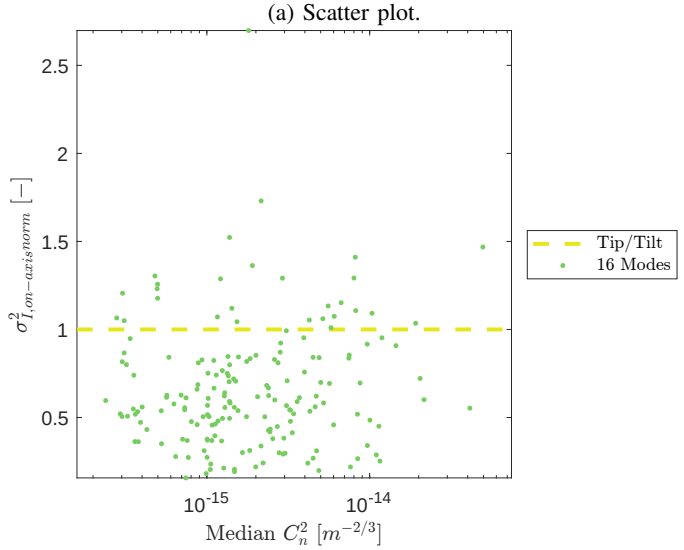

(c) Normalized scatter plot.

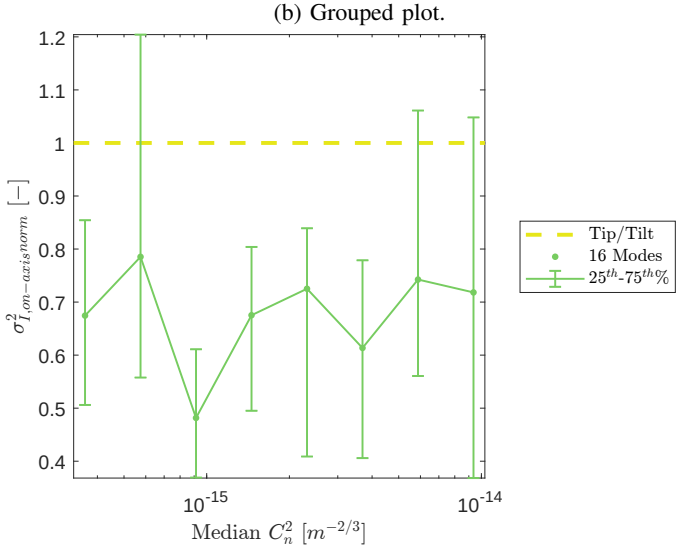

(d) Normalized grouped plot.

Fig. 84: On-axis scintillation results for 16 AO modes.

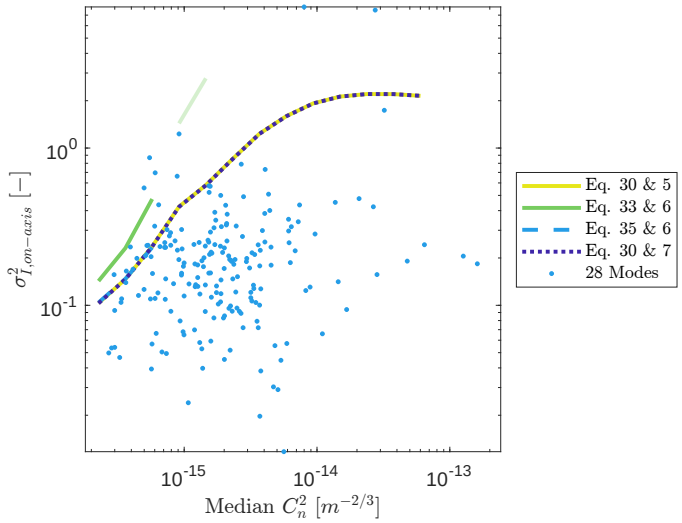

(a) Scatter plot.

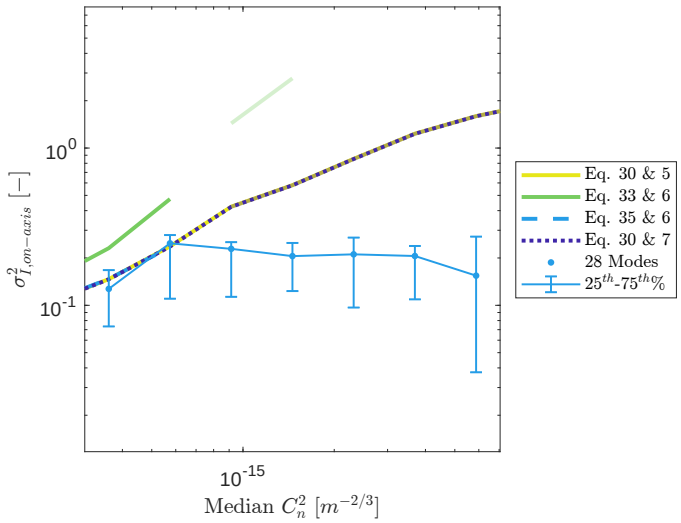

(b) Grouped plot.

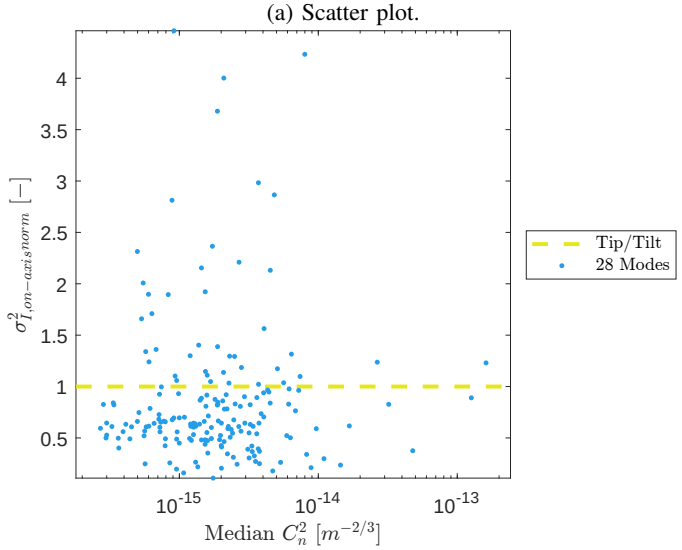

(c) Normalized scatter plot.

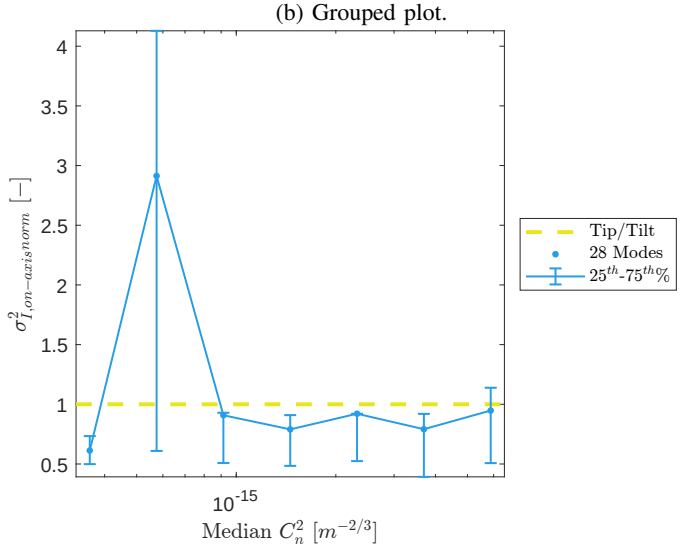

(d) Normalized grouped plot.

Fig. 85: On-axis scintillation results for 28 AO modes.

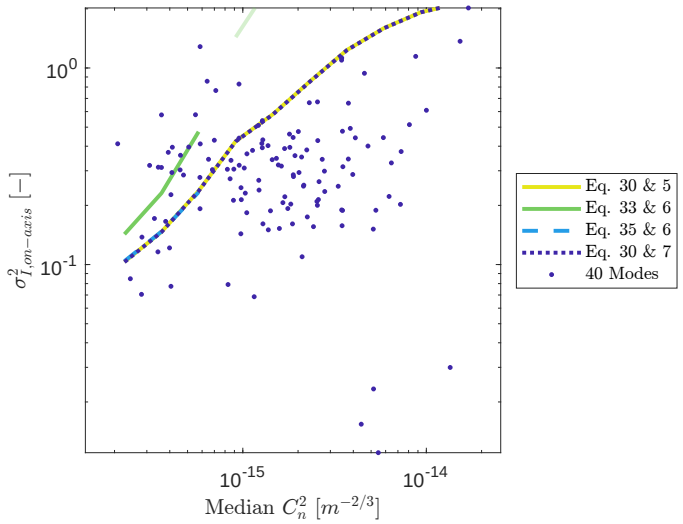

(a) Scatter plot.

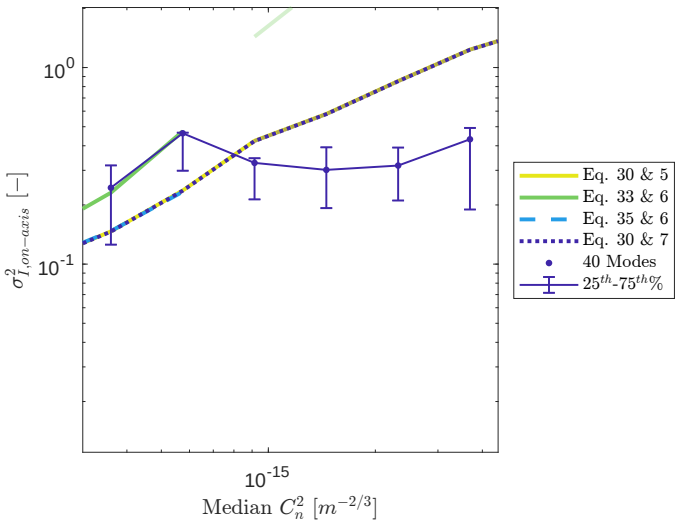

(b) Grouped plot.

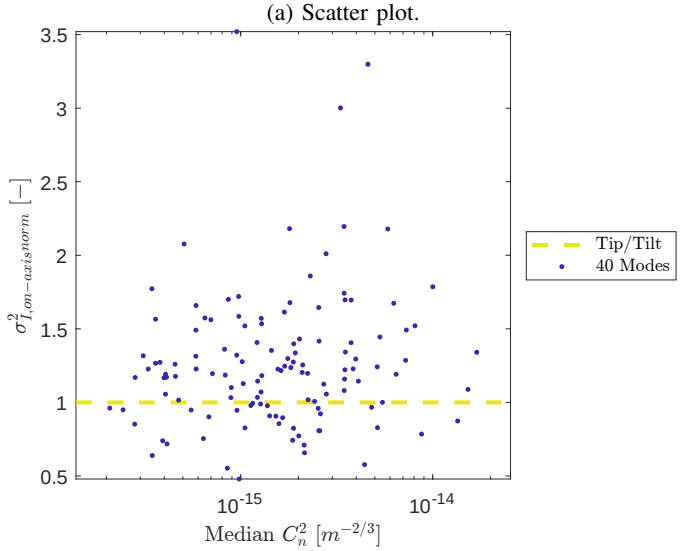

(c) Normalized scatter plot.

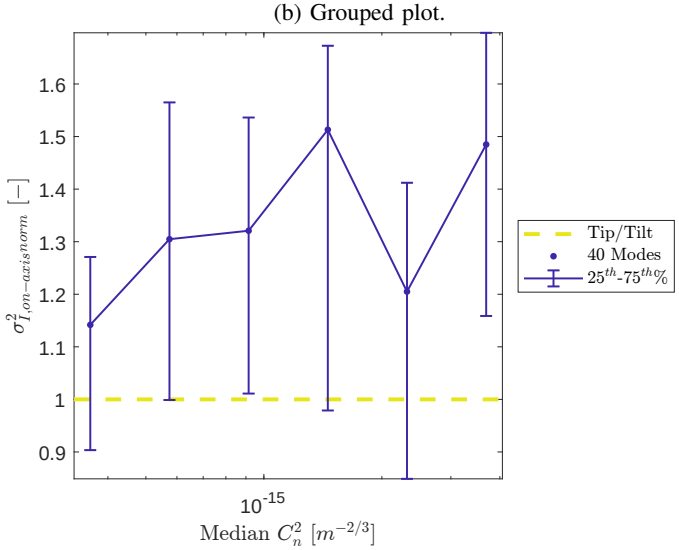

(d) Normalized grouped plot.

Fig. 86: On-axis scintillation results for 40 AO modes.

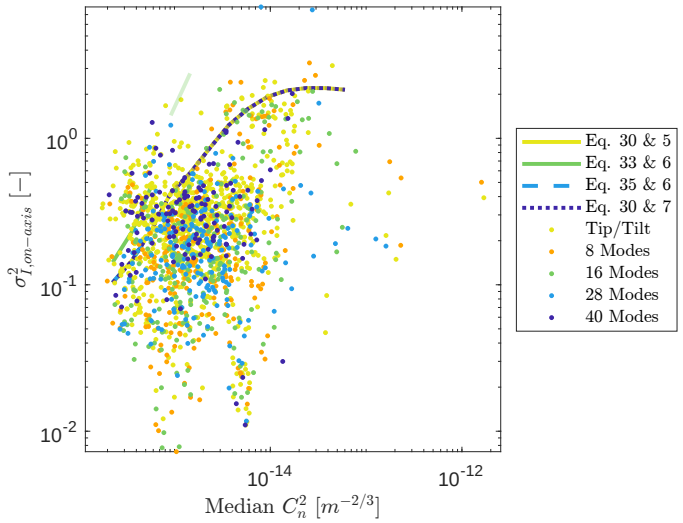

(a) Scatter plot.

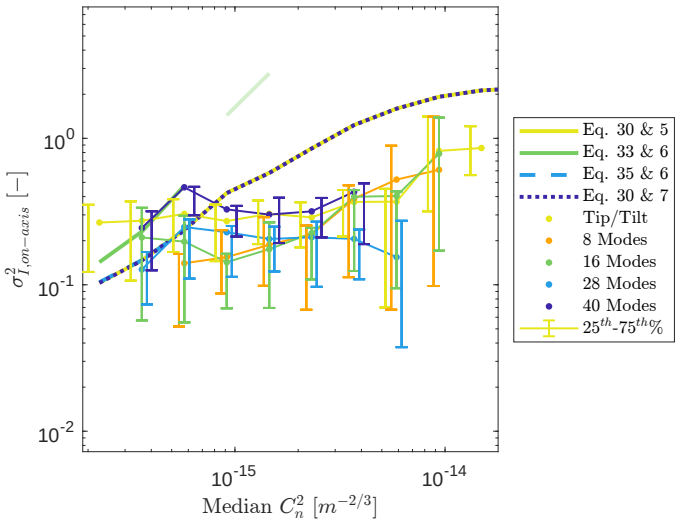

(b) Grouped plot.

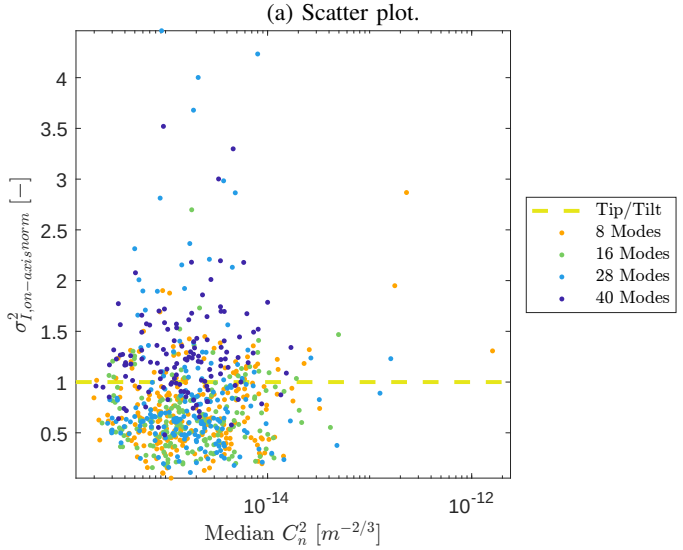

(c) Normalized scatter plot.

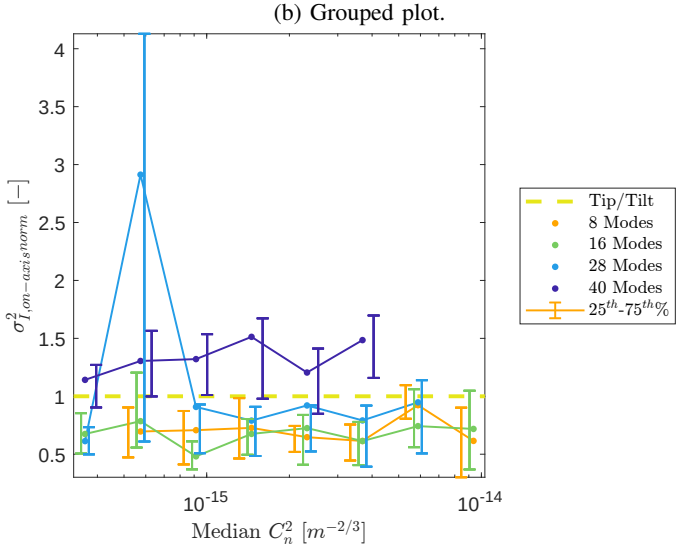

(d) Normalized grouped plot.

Fig. 87: On-axis scintillation results for all AO modes.

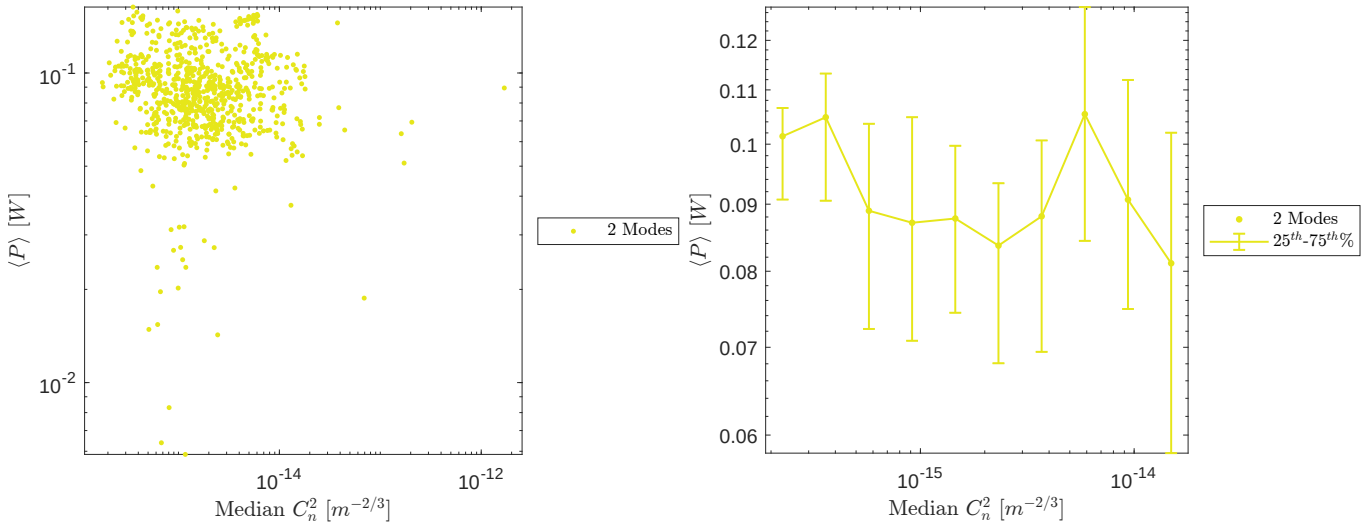

(a) Scatter plot.

(b) Grouped plot.

Fig. 88: Total received power results for tip/tilt pre-correction. Only results for $P_{Tx} = 0.200\ W$ are included.

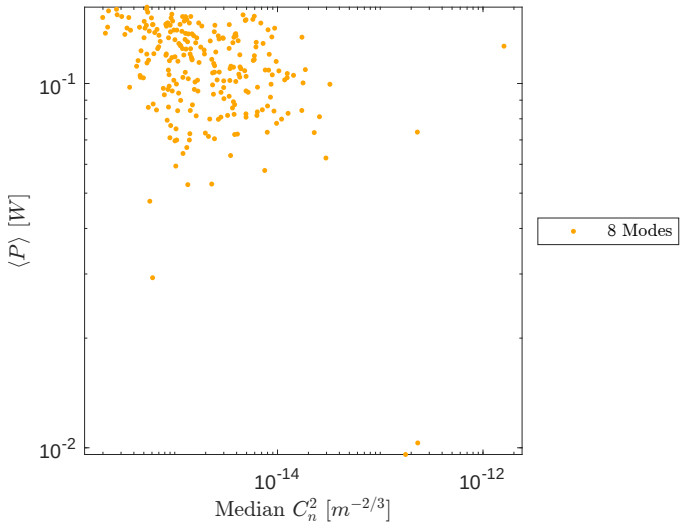

(a) Scatter plot.

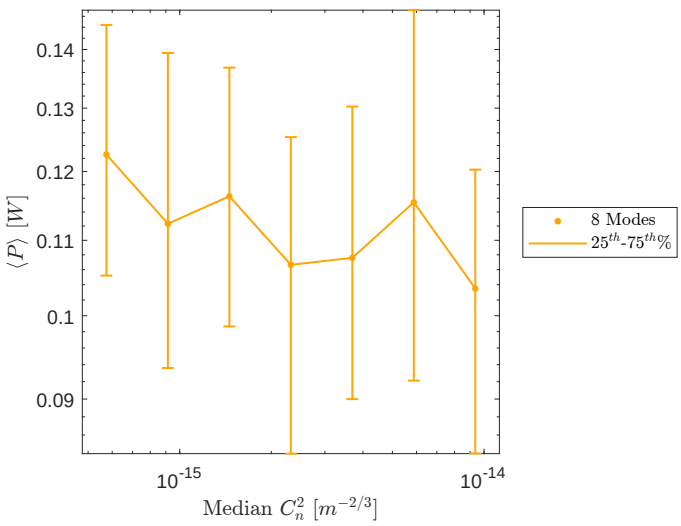

(b) Grouped plot.

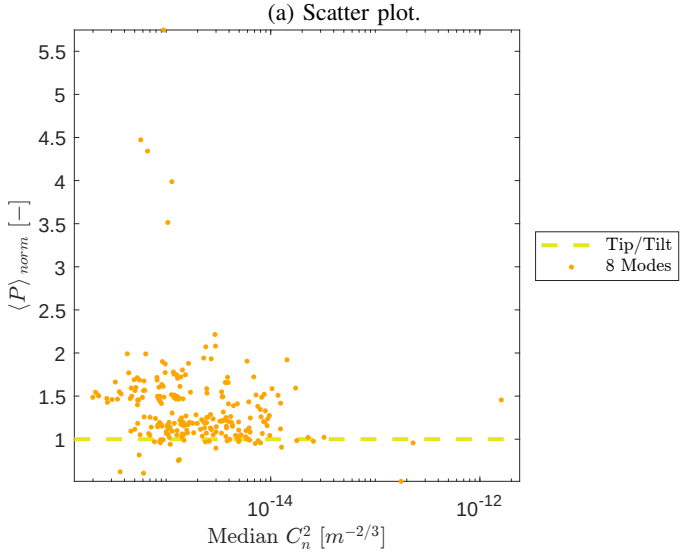

(c) Normalized scatter plot.

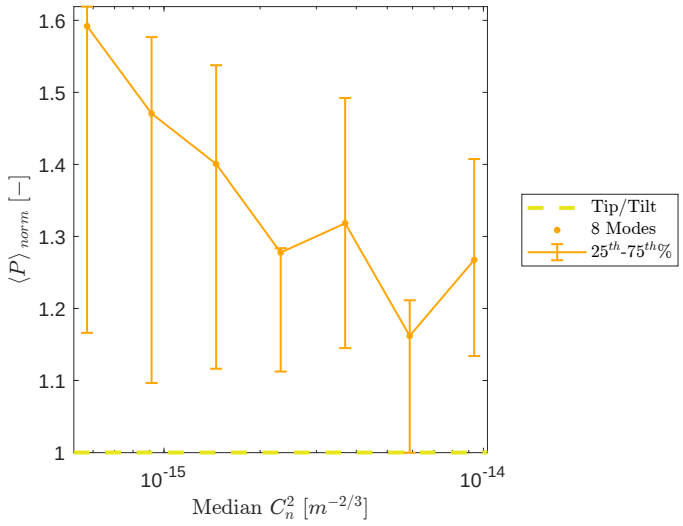

(d) Normalized grouped plot.

Fig. 89: Total received power results for 8 AO modes. Only results for $P_{Tx} = 0.200\ W$ are included.

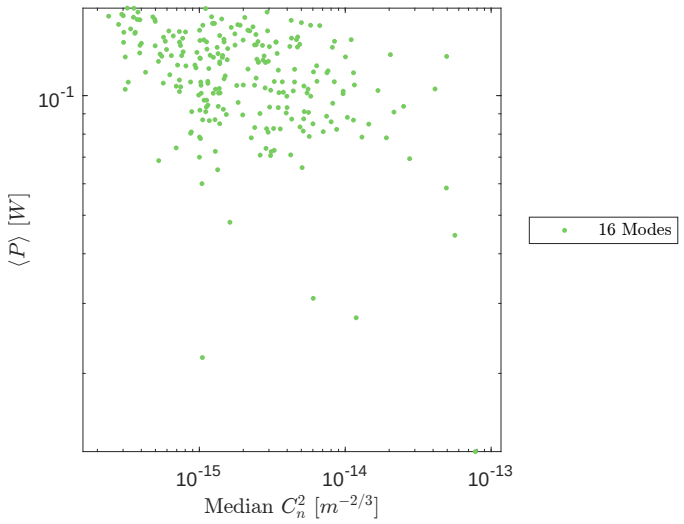

(a) Scatter plot.

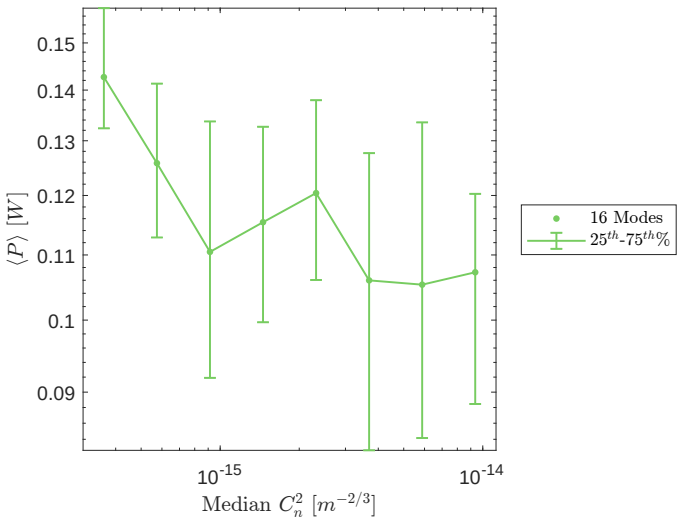

(b) Grouped plot.

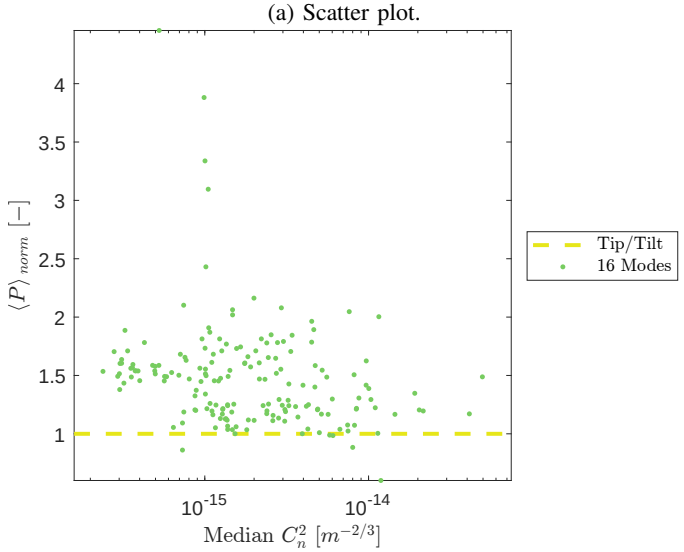

(c) Normalized scatter plot.

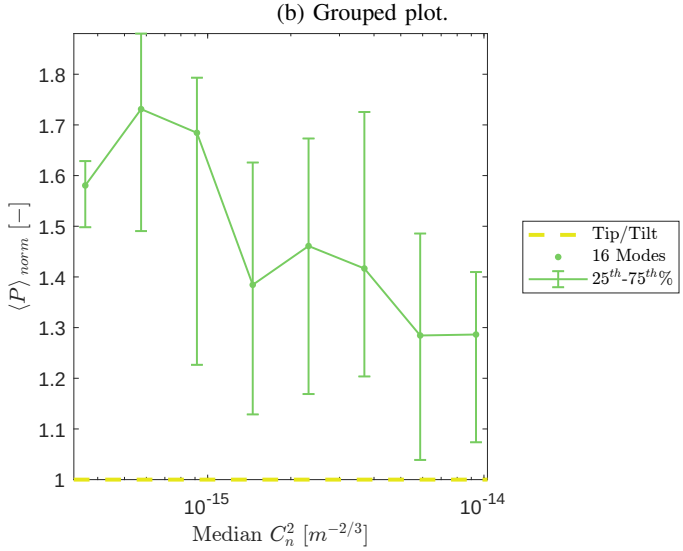

(d) Normalized grouped plot.

Fig. 90: Total received power results for 16 AO modes. Only results for $P_{Tx} = 0.200\ W$ are included.

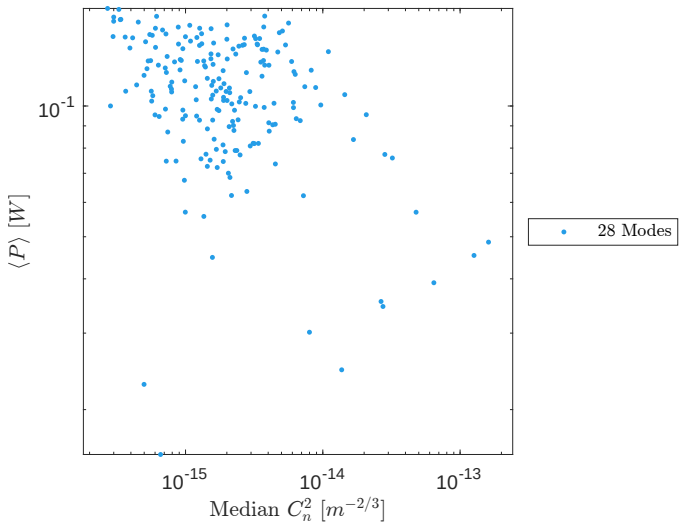

(a) Scatter plot.

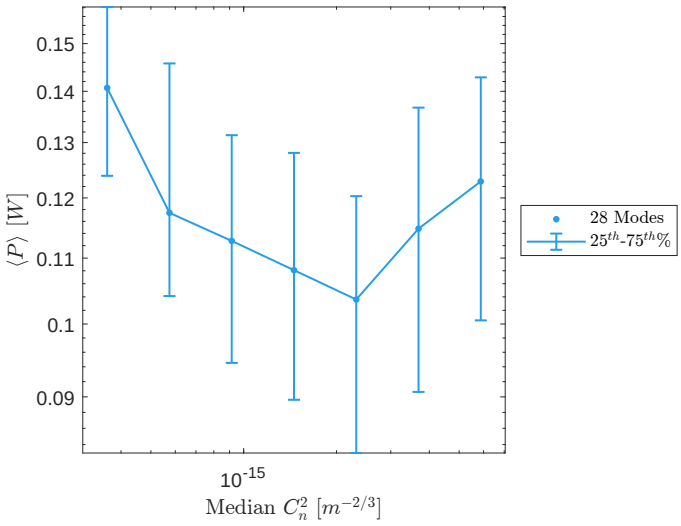

(b) Grouped plot.

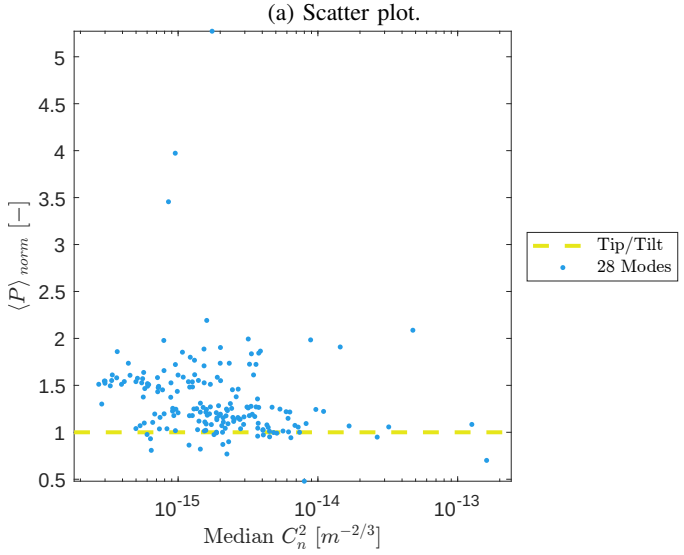

(c) Normalized scatter plot.

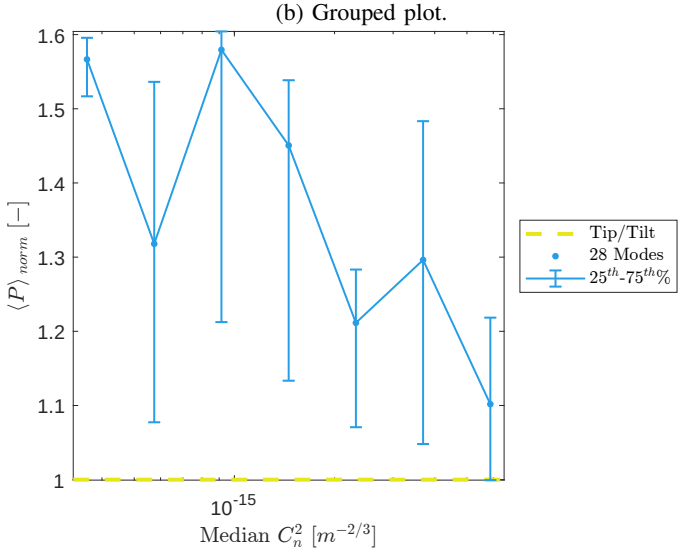

(d) Normalized grouped plot.

Fig. 91: Total received power results for 28 AO modes. Only results for $P_{Tx} = 0.200\ W$ are included.

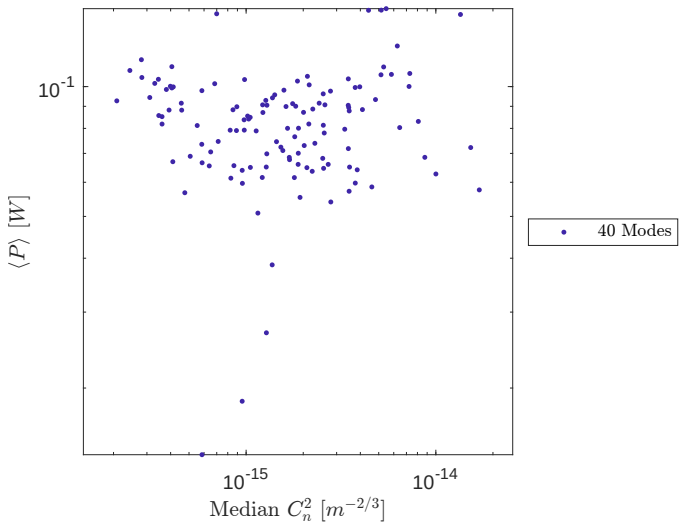

(a) Scatter plot.

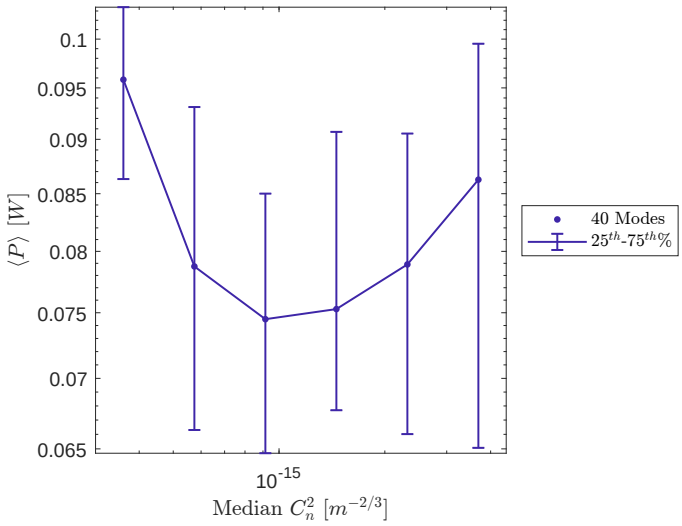

(b) Grouped plot.

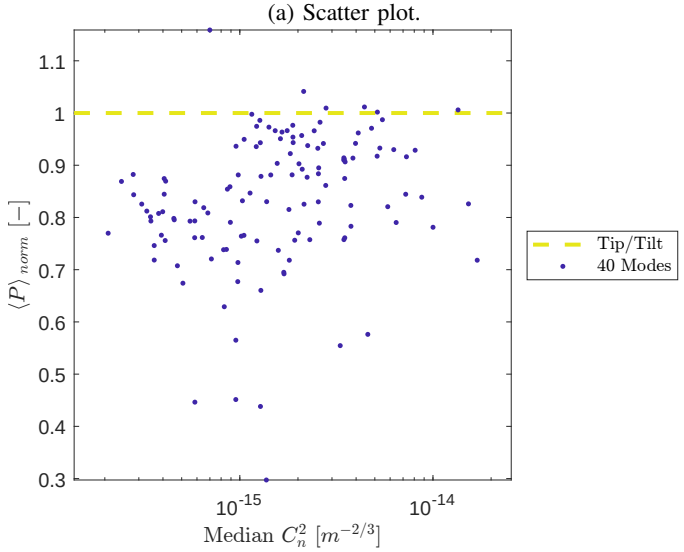

(c) Normalized scatter plot.

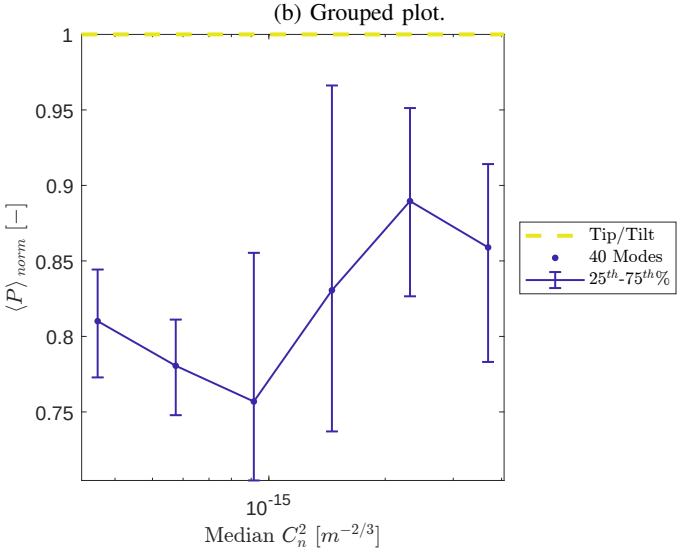

(d) Normalized grouped plot.

Fig. 92: Total received power results for 40 AO modes. Only results for $P_{Tx} = 0.200\ W$ are included.

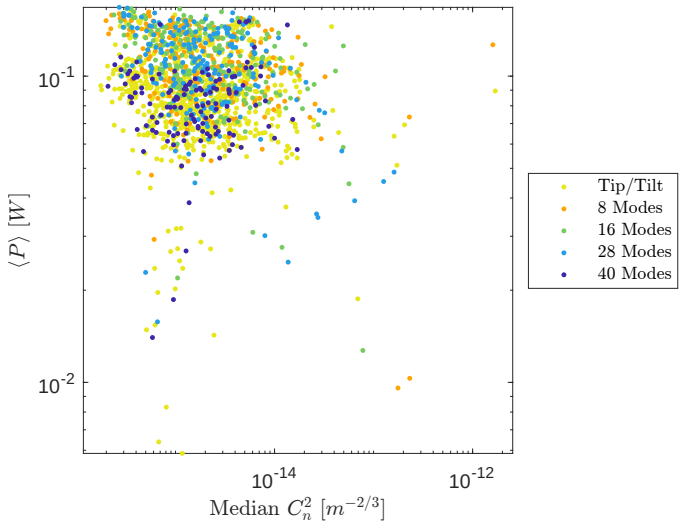

(a) Scatter plot.

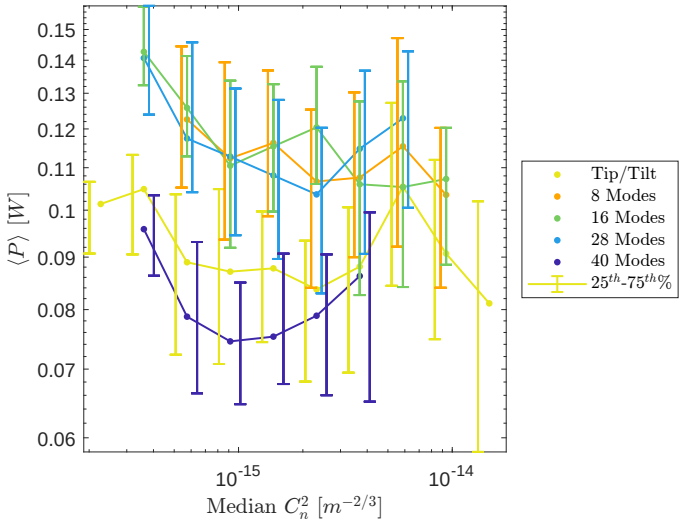

(b) Grouped plot.

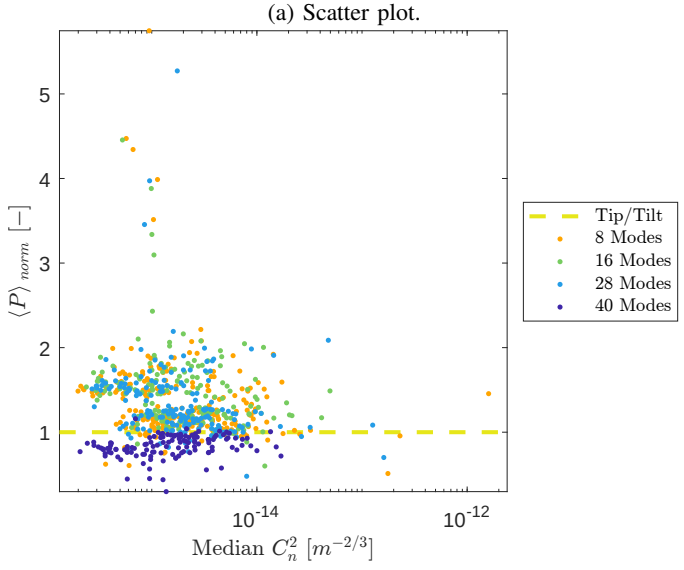

(c) Normalized scatter plot.

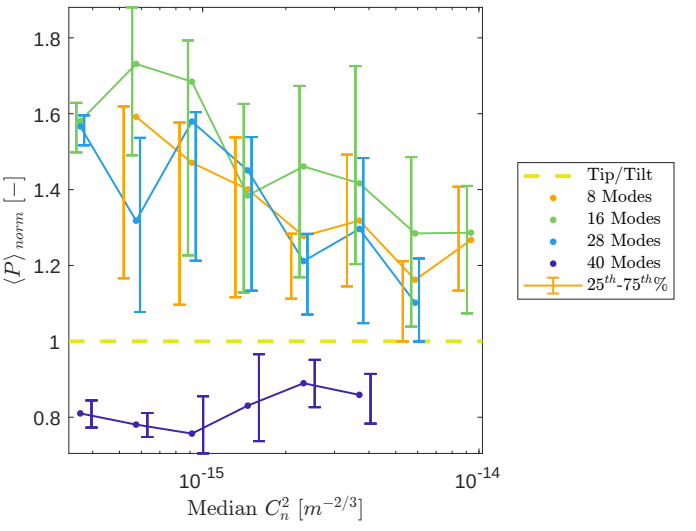

(d) Normalized grouped plot.

Fig. 93: Total received power results for all AO modes. Only results for $P_{Tx} = 0.200\ W$ are included.

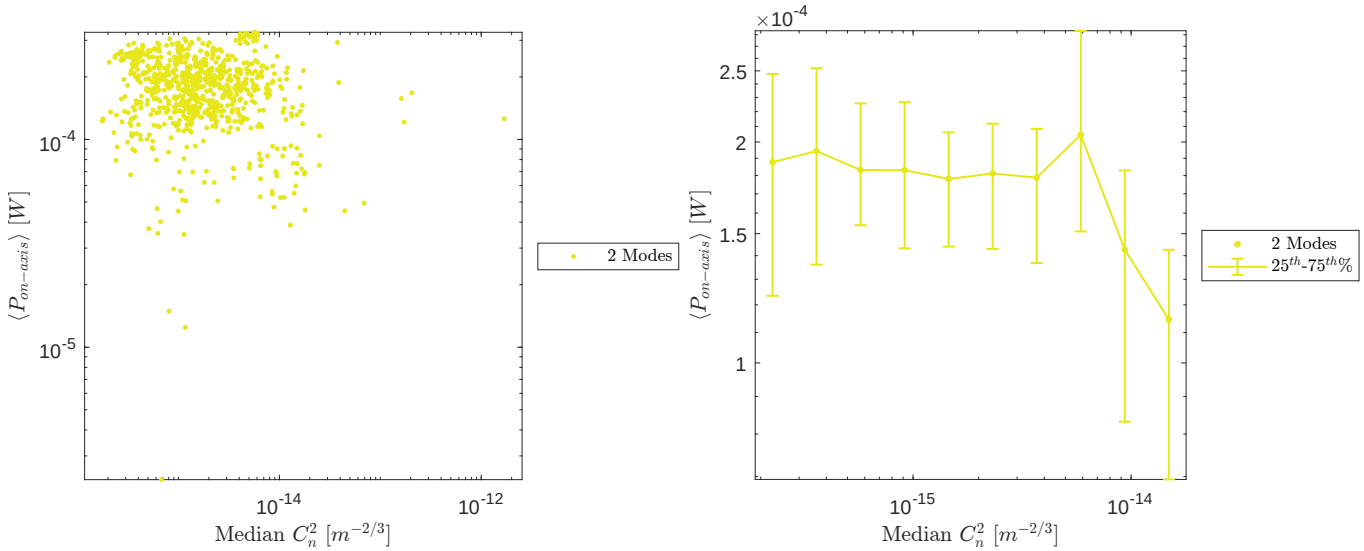

(a) Scatter plot.

(b) Grouped plot.

Fig. 94: Received on-axis power results for tip/tilt pre-correction. Only results for $P_{Tx} = 0.200\ W$ are included.

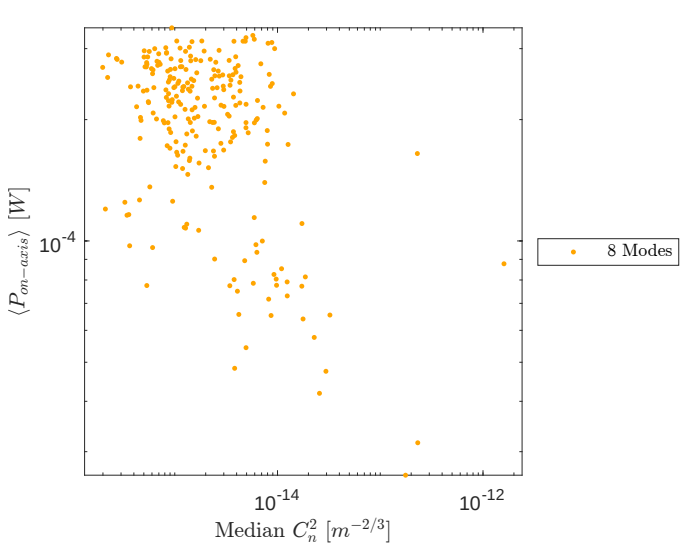

(a) Scatter plot.

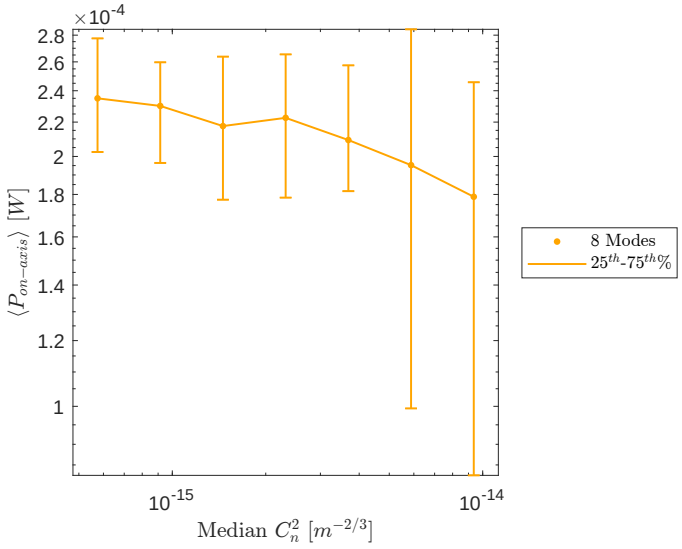

(b) Grouped plot.

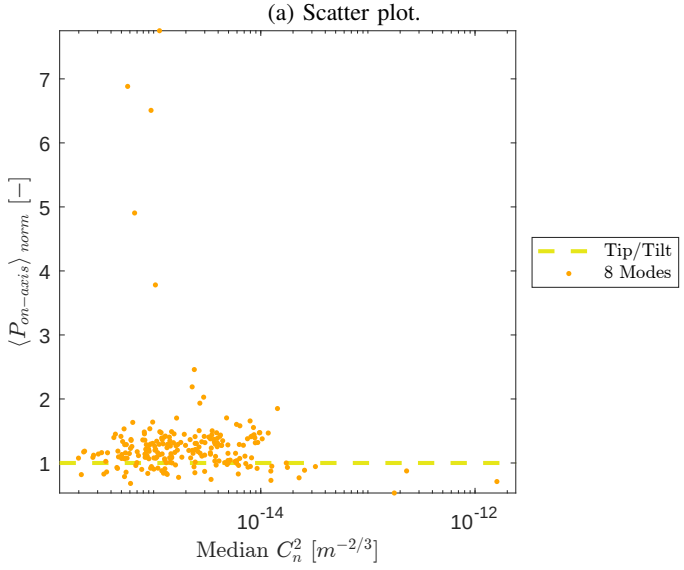

(c) Normalized scatter plot.

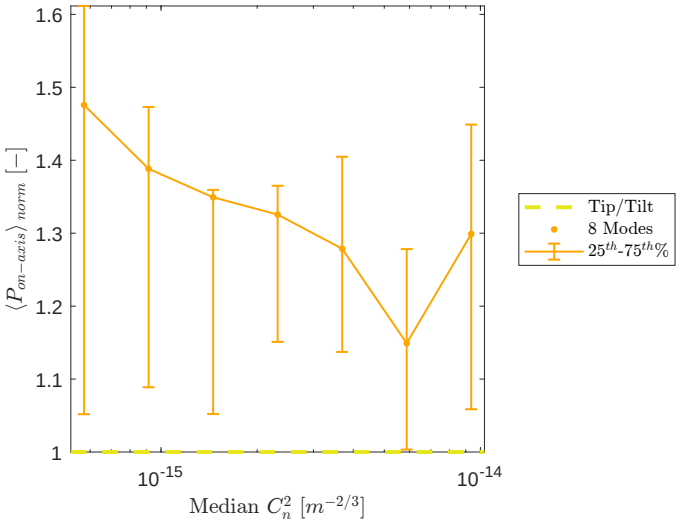

(d) Normalized grouped plot.

Fig. 95: Received on-axis power results for 8 AO modes. Only results for $P_{Tx} = 0.200\ W$ are included.

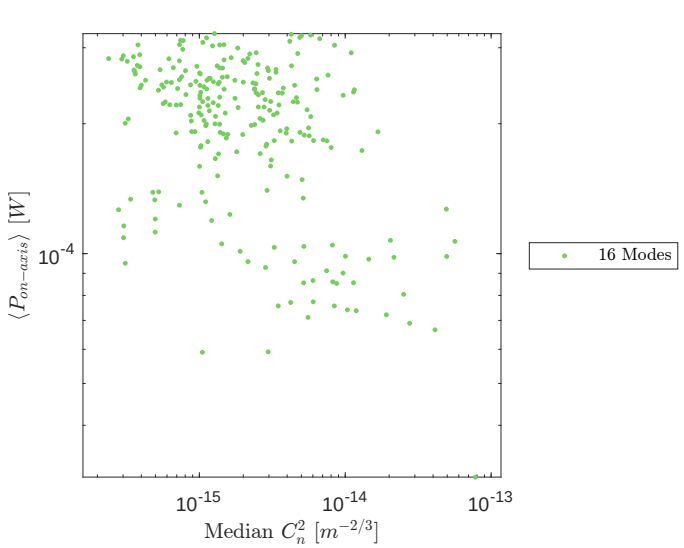

(a) Scatter plot.

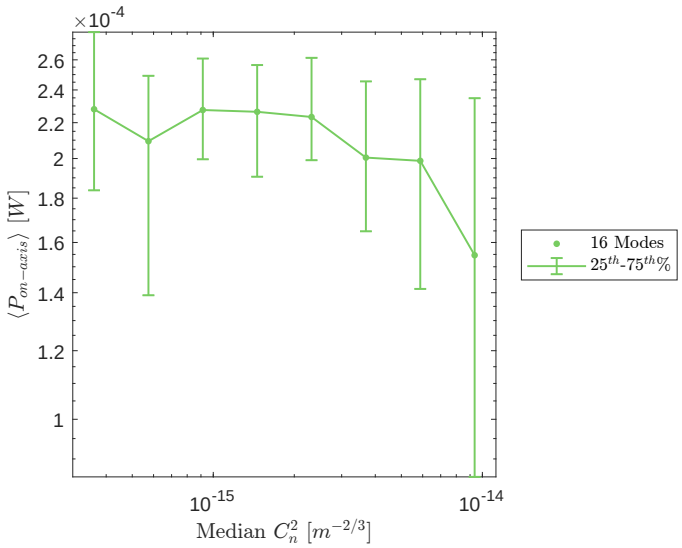

(b) Grouped plot.

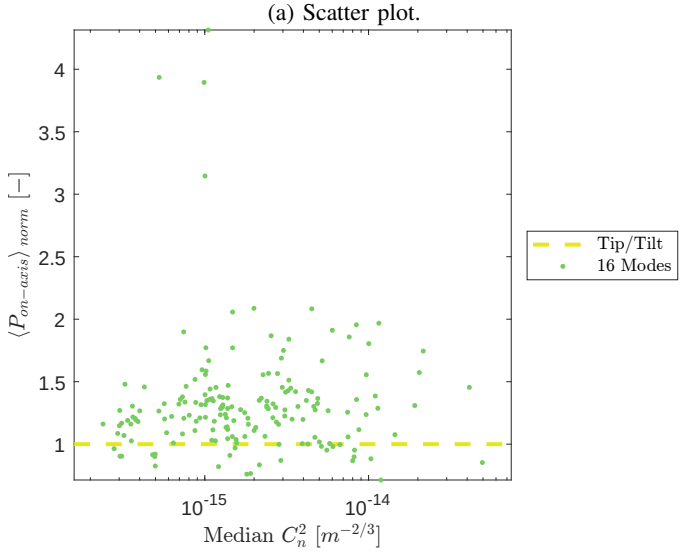

(c) Normalized scatter plot.

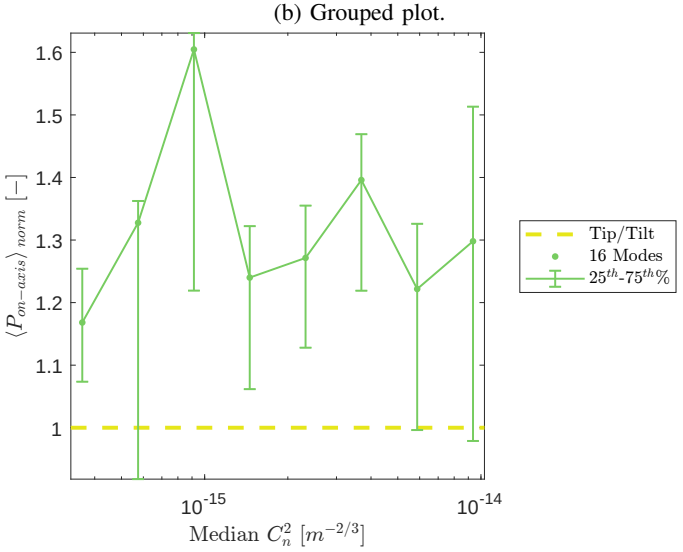

(d) Normalized grouped plot.

Fig. 96: Received on-axis power results for 16 AO modes. Only results for $P_{Tx} = 0.200\ W$ are included.

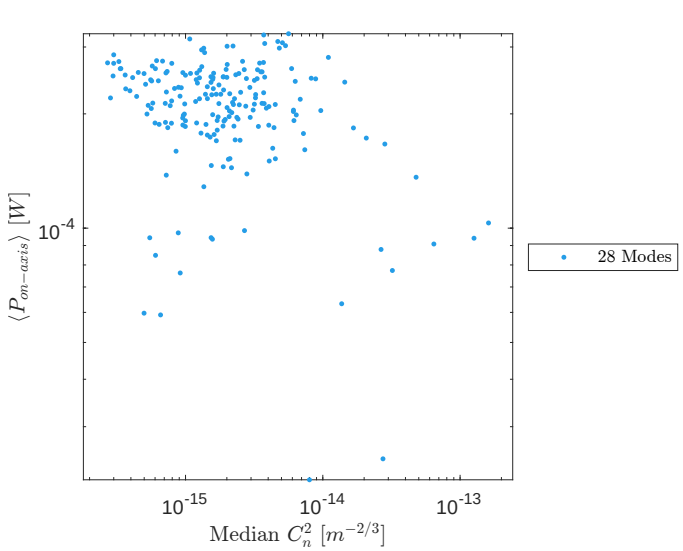

(a) Scatter plot.

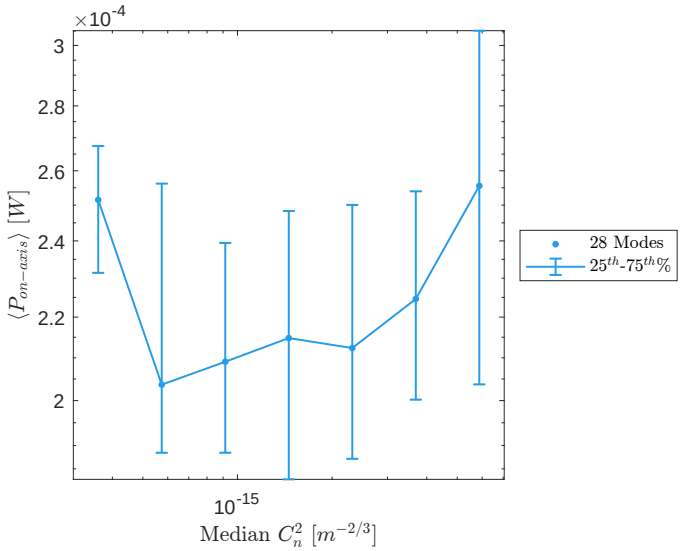

(b) Grouped plot.

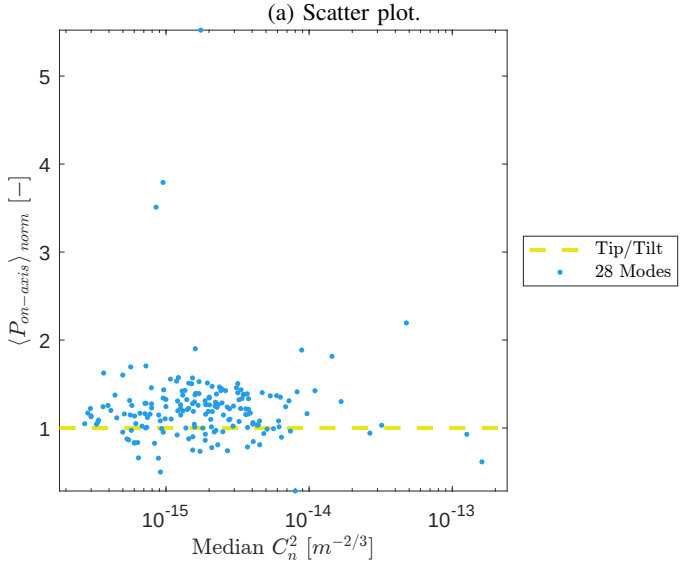

(c) Normalized scatter plot.

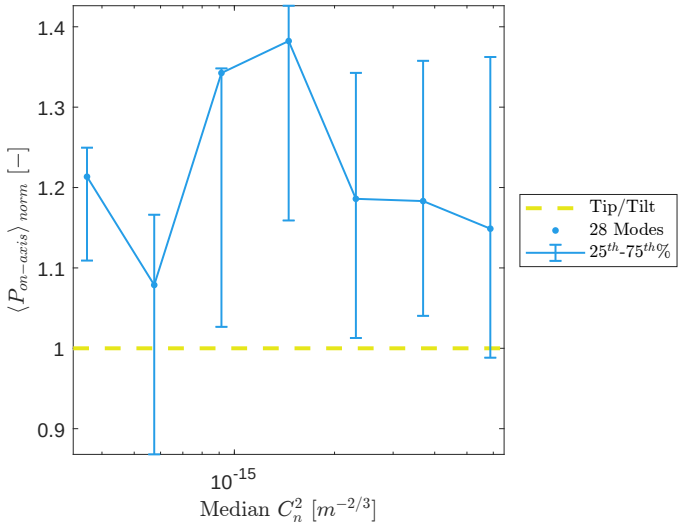

(d) Normalized grouped plot.

Fig. 97: Received on-axis power results for 28 AO modes. Only results for $P_{Tx} = 0.200\ W$ are included.

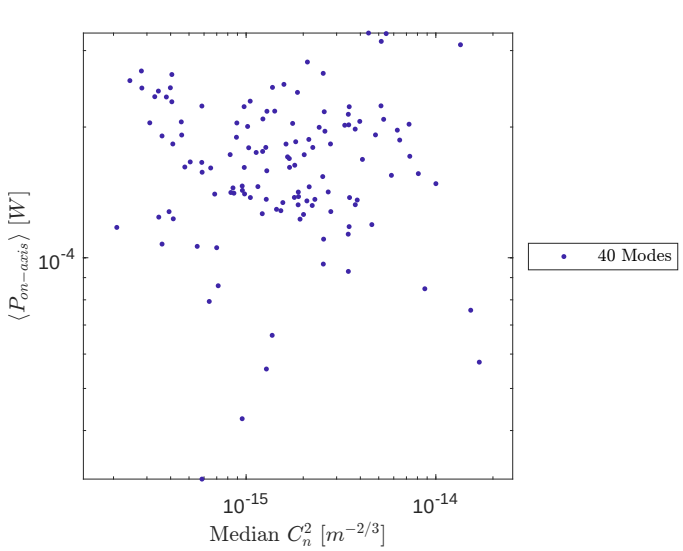

(a) Scatter plot.

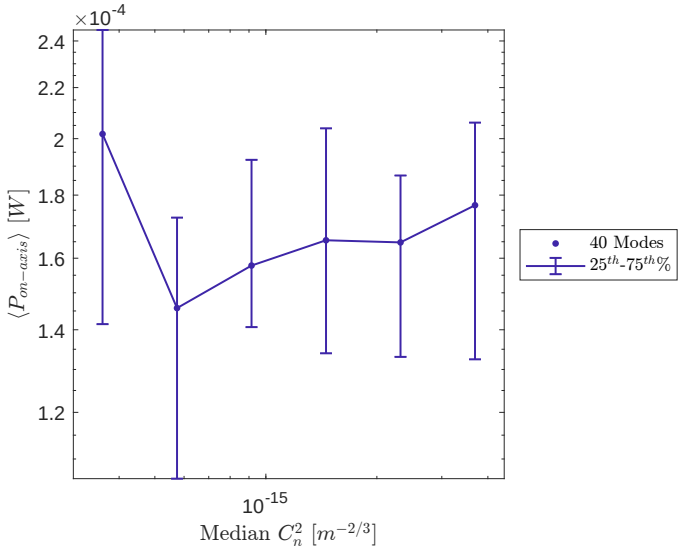

(b) Grouped plot.

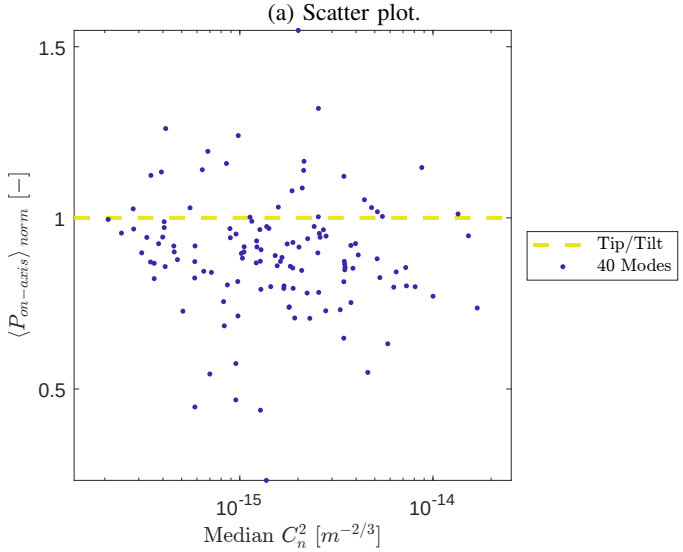

(c) Normalized scatter plot.

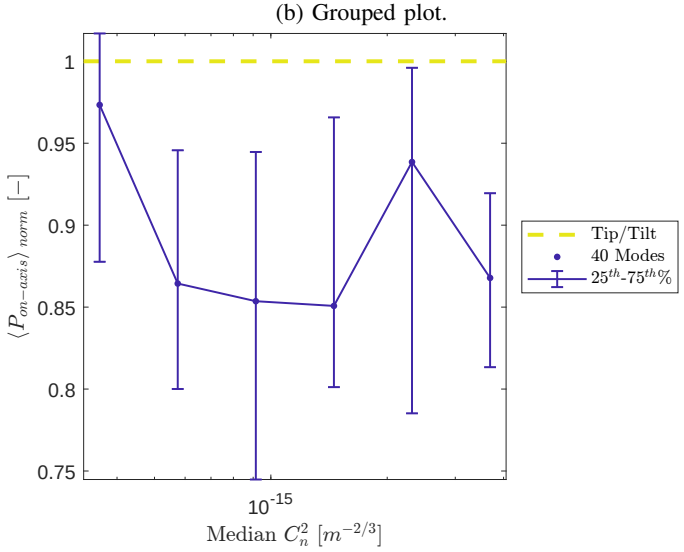

(d) Normalized grouped plot.

Fig. 98: Received on-axis power results for 40 AO modes. Only results for $P_{Tx} = 0.200\ W$ are included.

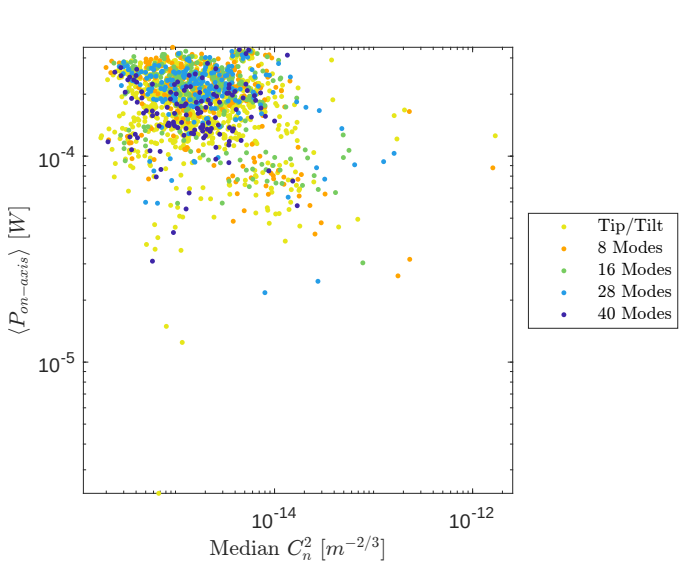

(a) Scatter plot.

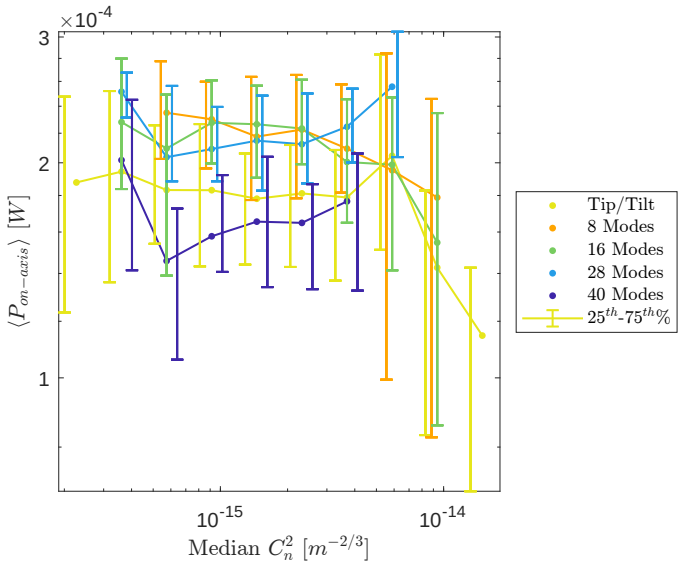

(b) Grouped plot.

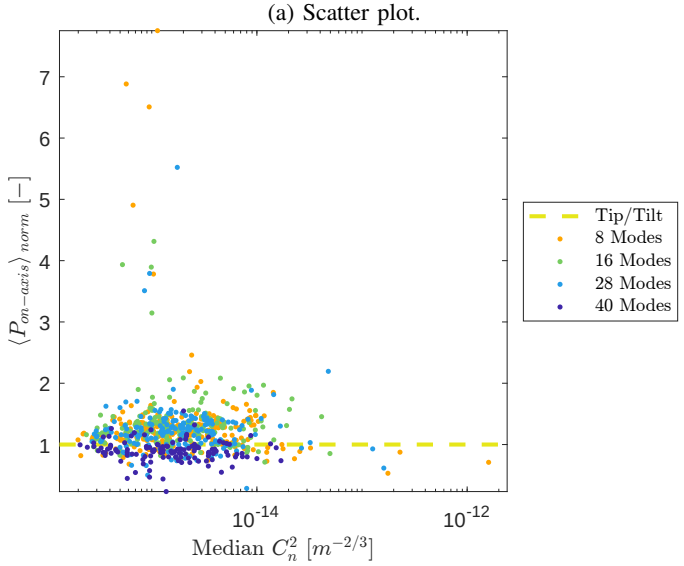

(c) Normalized scatter plot.

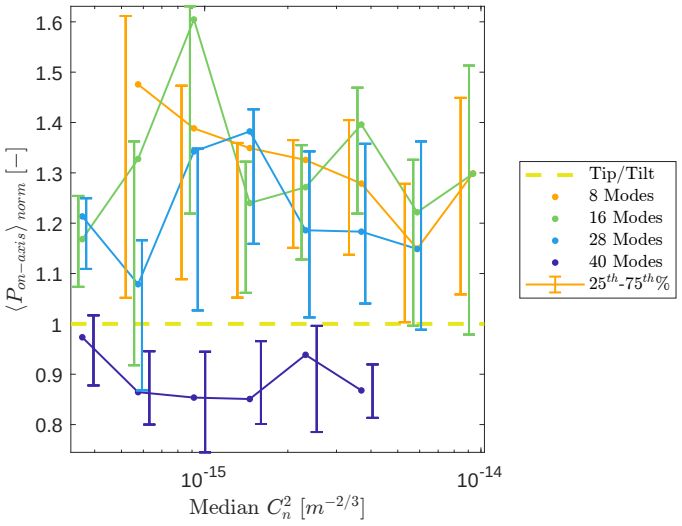

(d) Normalized grouped plot.

Fig. 99: Received on-axis power results for all AO modes. Only results for $P_{Tx} = 0.200\ W$ are included.